

**Production of micro and
nanoparticles of thermolabile
compounds using supercritical
assisted atomization**

Sara Liparoti

Omaggio a:
Riccardo Dalisi

“Nelle pieghe del tempo”



Unione Europea



*Ministero dell'Istruzione,
dell'Università e della Ricerca*



UNIVERSITÀ DEGLI
STUDI DI SALERNO

FONDO SOCIALE EUROPEO

Programma Operativo Nazionale 2007/2013

“Ricerca Scientifica, Sviluppo Tecnologico, Alta Formazione”

Regioni dell'Obiettivo 1 – Misura III.4

“Formazione superiore ed universitaria”

Department of Industrial Engineering

Ph.D. Course in:

Scienza e tecnologie per l'industria Chimica,

Farmaceutica ed Alimentare

(XI Cycle-New Series)

PRODUCTION OF MICRO AND NANOPARTICLES OF THERMOLABILE COMPOUNDS USING SUPERCRITICAL ASSISTED ATOMIZATION

Supervisor

Prof. Ernesto Reverchon

Dr. Ing. Giuseppe Caputo

Ph.D. student

Sara Liparoti

Scientific Referees

Dr. Ing Renata Adami

Dr. Ing. Andreas Braeuer

Ph.D. Course Coordinator

Prof. Paolo Ciambelli

I would like to thank here all the kind people around me who made this thesis possible with their help and support.

First of all, I am extremely grateful to my supervisor, Prof. Ernesto Reverchon, for giving me the opportunity to be part of his "Supercritical Fluid" team at the University of Salerno and for providing a stimulating and fun environment for me in which to learn and grow as a student and a researcher. His enthusiasm and passion for research, guidance and support, understanding and patience, added considerably to my experience.

My acknowledgements are also for Dr. Giuseppe Caputo for his valid suggestions.

I am grateful to Andreas Braeuer for his availability to take part in my scientific committee, for kindly giving me the opportunity to join his research group in Erlangen. His supervision with his expertise and valuable advices were precious for me. I want, also, to thank my mates in SAOT, especially Matthias „Bud Spencer" and Robert, who supported me during thesis drafting.

A special thank is for Renata Adami, who patiently introduced me in SAA process and in laser based technique. I appreciate her suggestions! She will be always „Mamma Chioccia" for me.

Thanks also to Supercritical Fluid group: Mariarosa, for her effective suggestions and her availability, Iolanda, Stefano, Giovanna, Marco, Andrea, Peppe, Lucia, Valentina, Francesco Cice, Massimiliano, Emilia, Titti and Paola. Moreover I want to mention my good Spanish friend Luis, who is known as Gigino. I always remember that I have "Vivere Piano...", even if it is very difficult for me! Thank you Islane, my miss-stress!.

Many thanks to my friend Francesco Glielmi. He kindly supported me during the University period. We have been the nice couple „Sandra e Raimondo"! I hope that our friendship will be forever.

I would like to thank the person who divided with me this „PhD adventure": Roberta Campardelli. We have shared everything, the desk, the computer and, sometimes the „brain". You are a good friend for me, a sort of „wife"!

Special thanks also to my friends outside the University: Davide, Nadia, Niky, Dino, Rosanna, Ilaria, Antonio and Pietro. I am very lucky to have these good friends.

How to forget my parents and my brother, with Lidia. My family is always my landmark!

Very special Thanks to my husband Francesco. He is very precious for me. He supported and endured me in these years. I don't know how he could do this! You are my best choose! Thank you so much!

Publication list

International journal

Renata Adami, Sara Liparoti, Ernesto Reverchon(2011). *A new supercritical assisted atomization configuration, for the micronization of thermolabile compounds*. **CHEMICAL ENGINEERING JOURNAL**. Vol. 173. Pag.55-61 ISSN:1385-8947.

Renata Adami, Sara Liparoti, Lorella Izzo, Daniela Pappalardo, Ernesto Reverchon (2012) “*PLA-PEG copolymers micronization by supercritical assisted atomization*” **THE JOURNAL OF SUPERCRITICAL FLUIDS**. Vol 72. Pag 15-21.

Sara Liparoti, Renata Adami, Ernesto Reverchon (2012) “*PEG micronization by supercritical assisted atomization, operated under reduced pressure*” **THE JOURNAL OF SUPERCRITICAL FLUIDS**. Vol 72. Pag. 46-51.

Giuseppe Caputo, Sara Liparoti, Renata Adami, and Ernesto Reverchon. (2012) “*Use of Supercritical CO₂ and N₂ as Dissolved Gases for the Atomization of Ethanol and Water*” **INDUSTRIAL & ENGINEERING CHEMISTRY RESEARCH**. Vol 51 Pag. 11803–11808.

Rita P. Aquino, Giulia Auriemma, Teresa Mencherini, Paola Russo, Amalia Porta, Renata Adami, Sara Liparoti, Giovanna Della Porta, Ernesto Reverchon, Pasquale Del Gaudio. (2012) “*Design and production of gentamicin/dextran microparticles by supercritical assisted atomisation for the treatment of wound bacterial infections*” **INTERNATIONAL JOURNAL OF PHARMACEUTICS**.
<http://dx.doi.org/10.1016/j.ijpharm.2012.07.074>

L.M. Navarro, S.Liparoti, J.L. Marqués, G. Della Porta, E. Reverchon, A.M. Mainar, J.S. Urieta, R. Adami. “*Rotenone Encapsulation in Biopolymers by Supercritical Assisted Atomization*”, **submitted to BIOTECHNOLOGY AND BIOENGINEERING**

Proceeding

Sara Liparoti, Renata Adami, Ernesto Reverchon (2011). Supercritical assisted atomization under reduced pressure: formation of PEG microspheres loaded with lipophilic vitamins. In: 13th European meeting on supercritical fluids The Hague 9th-13th October 2011 Maaik KROON, Cor PETERS,

Caroline van Os-ROVERS, Pleunie SMITS, Geert-Jan WITKAMP, Jaap van SPROSEN, Maaike van ROOSMALEN Pag.1-6 ISBN:9782905267771

Liparoti, S.; Adami, R.; Reverchon, E.(2010). Production of microspheres of Bovine Serum Albumin by supercritical assisted atomization at reduced pressure. In: 9th Confer. on Supercrit. Fluids an their Applic. Sorrento 5-8 Sept E. Reverchon Vol.1, Pag.223-228 ISBN:9788878970403

Adami, R; Liparoti, S.; Della Porta, G.; Del Gaudio, P.; Auriemma, G.; Prota, R.P.; Aquino, R.; Reverchon, E.(2010). Gentamicin loaded albumin/pectine microspheres for drug release obtained by SAA. Sorrento 5-8 Sept. E. Reverchon Vol.1, Pag.193-196 ISBN:9788878970403

Giuseppe Caputo, Sara Liparoti, Renata Adami, Libero Sesti Osséo(2011). Use of supercritical co2 as dissolved gas for the atomization of ethanol". In: 12th International Conference on MULTIPHASE FLOW IN INDUSTRIAL PLANTS ischia (NA) 21-23 settembre 2011 ANIMP Pag.1-8 ISBN:9788889677223

Sara Liparoti, Renata Adami, Ernesto Reverchon (2012) "Supercritical Assisted Atomization: effect of operative conditions on PVP particle size and morphology" 10th International Symposium on Supercritical Fluids-May 13-16- San Francisco

Contents

Chapter I.....	1
General statement on atomization.....	1
I.1. Drop and spray formation.....	1
I.2. Supercritical fluid based processes.....	4
I.3. CO ₂ -Assisted Nebulization with a Bubble Dryer (CAN-BD).....	4
I.4. Supercritical Assisted Atomization (SAA).....	5
Chapter II.....	9
Aim of the work.....	9
Chapter III.....	11
Analytical methods.....	11
III.1. Analysis on morphology.....	11
III.1.1. Scanning electron microscope field emission.....	11
III.1.2. Particle size analysis.....	11
III.2. Solid state analysis.....	12
III.2.1. X-Ray Diffractometry.....	12
III.2.2. Differential scanning calorimeter (DSC).....	12
III.3. Stability and denaturation analysis.....	12
III.3.1. Protein stability: FTIR.....	12
III.3.2. Dissolution rate test.....	12
III.3.3. Solvent residue analysis.....	13
III.4. Structural analysis.....	13
III.4.1. H and C NMR analysis.....	13
III.4.2. Gel Permeation Chromatography (GPC).....	13
III.4.3. High-performance liquid chromatography (HPLC).....	13
Chapter IV.....	15
Vapour liquid equilibria measurements.....	15
IV.1. Raman Scattering.....	16
IV.2. Description of Raman spectroscopy.....	18
IV.3. Concentration measurements.....	20
IV.4. Apparatus and methods.....	21
IV.4.1. Variable volume high pressure cell.....	22
IV.5. Results and discussion.....	23
IV.5.1 Calibration curve.....	23
IV.6. Equilibria CO ₂ -acetone.....	27
IV.7. Equilibria CO ₂ -acetone-water.....	28
IV.8. Conclusions.....	30
Chapter V.....	33
Experimental study on atomization mechanism.....	33
V.1 Supercritical dissolved gas atomization.....	34
V.1.1. Apparatus and methods.....	35

V.2. Results	37
V.2.1 Atomization of ethanol and water using CO ₂	39
V.3 Mechanism of atomization	44
V.4. Conclusions	47
Chapter VI.....	49
Effect of the solvent on particle size	49
VI.1 Material and methods.....	49
VI.2 Effect of solvents	50
Water	50
Mixture water-acetone.....	53
Ethanol	56
VI.3. Conclusions.....	61
Chapter VII.....	63
Choice of the operative conditions for the precipitation vessel.	63
VII.1 Drying mechanism.....	63
VII.1.1. Nitrogen flow rate in the precipitator	64
VII.2 Study of precipitation at low temperature.....	65
VII.2.1 Choice of the vacuum system	65
Chapter VIII	75
Validation of the SAA plant in the configuration operated at reduced pressure.....	75
VIII.1 Materials.....	75
VIII.1.1. Bovine serum albumin.....	75
VIII.1.2. Poly-L-Lactide Acid.....	76
VIII.1.3. Polyethylene glycol	77
VIII.1.4. Coprecipitates PLA-PEG	78
VIII.1.5. Coprecipitates: PEG α -tocopherol acetate.....	81
VIII.2. Results and discussion.....	82
VIII.2.1. BSA	82
Behavior of the system water-SC-CO ₂	82
Variation of the temperature in the precipitation vessel.....	83
Characterization of BSA microparticles.....	85
Discussion	86
VIII.2.2. PLLA	87
Behavior of the system chloroform-SC-CO ₂	87
Variation of temperature at different precipitation pressure	88
Solvent Residue.....	92
Solid state	92
Discussion	94
VIII.2.3. PEG	94
Behavior of the system acetone-SC-CO ₂	94
Variation of polymer concentration	97
Effect of PEG10000 concentration.....	100
Effect of precipitation temperature.....	104

Solid state.....	107
Discussion.....	109
VIII.2.4. Copolymers PLA-PEG.....	109
1:4 copolymer processing	111
1:8 copolymer processing	112
Characterization: composition	117
Discussion	120
VIII.2.5. Coprecipitates: PEG- α Tocopherol acetate	120
Discussion	125
VIII.2.6. Effect of polymer architecture and molecular weight	125
VIII.3. Conclusions	129
Chapter IX.....	131
Conclusions.....	131
References.....	133
List of symbols.....	143

FIGURE INDEX

Figure I.1 (a) Rayleigh breakup. Drop diameters larger than the jet diameter. Breakup occurs many nozzle diameters downstream of nozzle. (b) First wind-induced regime. Drops with diameters of the order of jet diameter. Breakup occurs many nozzle diameters downstream of nozzle. (c) Second wind-induced regime. Drop sizes smaller than the jet diameter. Breakup starts some distance downstream of nozzle. (d) Atomization regime. Drop sizes much smaller than the jet diameter. Breakup starts at nozzle exit. (Lin and Reitz, 1998).....	2
Figure I.2 Sketch of the functioning principle of CAN-BD (Sievers et al., 2001).	5
Figure I.3 Sketch of the pneumatic atomization and decompressive atomization.	6
Figure I.4 Sketch of the formation of particles from drops at low evaporation rate.	7
Figure I.5 Sketch of the formation of particles from drops at high evaporation rate.	7
Figure IV.1 Energy level of diatomic molecules (Schrader, 2008)	17
Figure IV.2 Raman transitional scheme (Dowy et al., 2009)	19
Figure IV.3 Raman optical setup (Lopez and Leipertz, 2010)	21
Figure IV.4 Variable volume high pressure cell (Varona et al., 2012). 23	
Figure IV.5 Raman spectra for acetone, water and CO ₂	24
Figure IV.6 Calibration curve for the system water-acetone.....	25
Figure IV.7 Calibration curve for the system CO ₂ -acetone at 60°C and 100 bar.	27
Figure IV.8 Ebuilibrium data for the system CO ₂ -acetone at 60°C. Comparison between data reported in literature (Sato et al., 2010, Han et al., 2005, Adrian and Maurer, 1997) and data detected by Raman scattering (our measurement).	28
Figure IV.9 Comparison between the equilibria data obtained by Raman based technique and data reported in literature (Wendland et al., 1994) at 60°C and 100 bar	29
Figure IV.10 Molar fraction detection by Raman scattering at 80°C and 90 bar, for the system CO ₂ -acetone-water.	30
Figure V.1 Sketch of laser diffraction	33
Figure V.2 Scheme of the system used to study the droplet size distribution. (C) CO ₂ tank; (P1) CO ₂ pump; (P2) liquid pump; (M) saturator; (L) liquid tank; (SL) laser source; (R) receiver.	35
Figure V.3 Vapour liquid equilibria for the system water-CO ₂ . (Bamberger et al., 2000) at 40°C (△), 60°C (□) and 80°C (○).....	37

Figure V.4 VLE data (■) and operating points (□) of the system ethanol-CO ₂ at 40°C and 80°C (Knez et al., 2008)	38
Figure V.5 Influence of GLR on the SMD of the droplets measured using different solvents. CO ₂ flow rate=13 gr/min; N ₂ flow rate=9 gr/min; Temperature=80°C; Pressure=70-90 bar; axial distance from the injector=135 mm; injector diameter=120 μm.	40
Figure V.6 Influence of GLR on the SMD of the droplets at different temperatures. CO ₂ flow rate=16 gr/min, injector diameter=120 μm, and axial distance=135 mm and 7 mm.	41
Figure V.7 Influence of GLR on the SMD of the droplets measured at different distances (h) from the injector. CO ₂ flow rate = 16 gr/min and injector diameter = 120 μm.	42
Figure V.8 Influence of GLR on the SMD of the droplets measured at different CO ₂ flow rate. Temperature=80°C; Pressure=70-90 bar; axial distance from the injector=7 mm; nozzle diameter=120 μm.	43
Figure V.9 Influence of GLR on the SMD of the droplets measured at different nozzle diameters. Temperature=80°C; Pressure=70-90 bar; axial distance from the injector=7 mm.	44
Figure V.10 Sketch of possible flow regimes in the discharge nozzle (Sovani et al., 2001).	46
Figure V.11 Changing in cone angle due to the increase of GLR. (T=40°C; p=70 bar; nozzle diameter 120 μm).....	47
Figure VI.1 PVP microparticles obtained by SAA using water as solvent at different concentration of solute. (a) 20 mg/mL; (b) 40 mg/mL; (c) 80mg/mL.....	52
Figure VI.2 Vapor liquid equilibria for the system water-CO ₂ -acetone at 90 bar and 80°C detected by Raman based technology (see chapter IV. The operative points are indicated with the ratio water/acetone used, the GLR is 1.8 and is referred to the ratio between CO ₂ and liquid (water + acetone) flow rate (w/w).....	53
Figure VI.3 PVP microparticles obtained by SAA using water-acetone as solvent (a) 1/1(v/v); (b) 1/2 (v/v). Solute concentration 40 mg/mL.	55
Figure VI.4 Vapor liquid equilibria for the system ethanol-CO ₂ at different temperatures (■=40°C; □=60°C; ◆=80°C), adapted from Knez et al (Knez et al., 2008)	56
Figure VI.5 Microparticles obtained by SAA using ethanol and a concentration of PVP of 20 mg/mL.	57
Figure VI.6 PVP microparticles obtained by SAA changing the saturator temperature. Ethanol was used as solvent and the concentration of solute was 20 mg/mL; GLR=1.8; p=70-93 bar (see Table VI.3).	58
Figure VI.7 PVP microparticles obtained by SAA using different nozzle diameters. Ethanol was used as solvent and the concentration of solute was 20 mg/mL.....	59

Figure VI.8 XRPD and DSC of PVP powder obtained by SAA compared with the untreated material.	60
Figure VII.1 Scroll pump	68
Figure VII.2 Membrane pump	68
Figure VII.3 Piston pump	69
Figure VII.4 Rotative pump.	69
Figure VII.5 DVP pump.....	71
Figure VII.6 Vacuum rate scheme of DVP ZA-100P pump	72
Figure VII.7 Scheme of the condenser.....	72
Figure VII.8 Configuration with vacuum system of SAA plant. GP: gas pump; H: heat exchanger; M: saturator; L: liquid feed; LP: liquid pump; P: precipitator; C:condenser; VP1 and VP2 vacuum pump.....	73
Figure VIII.1 Schematic representation of copolymeric architectures synthesized in this work (Izzo and Pappalardo, 2010).....	80
Figure VIII.2 SEM images showing the effect of precipitation temperature on the morphology of BSA microparticles. The operating conditions set in the precipitator were 80°C (a) and 60°C (b). See Table VIII.2	84
Figure VIII.3 PSD of BSA powders obtained by SAA operating at 0.8 bar and at different precipitation temperatures. The calculations were performed in terms of volumetric cumulative percentages.	85
Figure VIII.4 High pressure vapor liquid equilibria at 80 °C; experimental data adapted from Peters et al (Peters and Florusse, 1995), for the binary system CO ₂ -CHCl ₃	87
Figure VIII.5 SEM images showing the effect of the precipitation temperature on the morphology of PLLA microparticles obtained using SAA. Different temperatures were set in the precipitator: 30°C (a) and 40°C (b). See Table VIII.3	89
Figure VIII.6 Particle size distribution (PSD) of PLLA powders obtained by SAA operating at 0.65 bar and 30°C in the precipitation vessel. The calculations were performed in terms of volumetric cumulative percentages.	90
Figure VIII.7 SEM images showing the effect of precipitation temperature on the morphology of PLLA microparticles obtained using SAA. Saturator operated at 80°C, 100 bar; precipitator operated at 30°C (a) and 40°C (b), 0.5 bar. See Table VIII.3	91
Figure VIII.8 PSD of PLLA powders obtained by SAA operating at 0.5 bar and at different temperatures in the precipitation vessel. The calculations were performed in terms of volumetric cumulative percentages.	92

Figure VIII.9 XRPD of PLLA untreated (raw material) and PLLA microparticles produced by SAA process at different temperatures (30°C and 40°C) in the precipitation vessel.	93
Figure VIII.10 Thermograms of untreated raw material and SAA produced PLLA microparticles at different temperatures (30°C and 40°C) in the precipitation vessel.	93
Figure VIII.11 VLE of the system CO ₂ -acetone, at 40°C, adapted from Sato et al [77].	95
Figure VIII.12 SEM images showing the effect of high precipitation temperature on the morphology of PEG microparticles.	96
Figure VIII.13 SEM images showing the effect of low precipitation temperature on the morphology of PEG microparticles. The operating conditions set in the precipitator were 5°C and 0.6 bar.	96
Figure VIII.14 SEM images showing the effect of concentration on the morphology of PEG microparticles; 40 mg/mL (p03) and 60 mg/mL (p04).	98
Figure VIII.15 PSD of PEG 6000 powders obtained by SAA at different concentration of solute in the liquid feed. The calculations were performed in terms of volumetric cumulative percentages by DLS analysis.	99
Figure VIII.16 SEM images showing the microparticles obtained using PEG (M _w :10000). Set conditions 18°C and 0.8 bar in the precipitator and 40°C and 67 bar in the saturator.	100
Figure VIII.17 SEM images showing the effect of solute concentration on the morphology and diameter of PEG10000 microparticles obtained by SAA at 5°C and 0.8 bar, using (a) 20 mg/mL, (b) 30 mg/mL, (c) 40 mg/mL and (d) 60 mg/mL solute concentration. Histograms by count embedded.	102
Figure VIII.18 Volumetric cumulative PSDs, obtained DLS, of PEG10000 microparticles obtained by SAA at 5 °C and 0.8 bar, different concentrations.	103
Figure VIII.19 SEM images showing the effect of precipitation temperature on morphology and diameter of PEG10000 microparticles obtained by SAA at 0.8 bar, 20 mg/mL solute concentration and precipitation temperature: (a) 5°C, (b) 9°C and (c) 18°C. Histograms by count embedded.	105
Figure VIII.20 Volumetric cumulative PSDs, obtained by DLS, of PEG10000 powders obtained by SAA at 0.8 bar, 20 mg/mL solute concentration, operating at different precipitation temperatures.	106
Figure VIII.21 XRPD of PEG10000 untreated and microparticles produced by SAA at 5°C and 20 mg/mL concentration.	107
Figure VIII.22 DSC thermograms of PEG10000 untreated and PEG10000 microparticles produced by SAA at different solute concentration. Analyses performed with heating rate of 5°C/min.	108
Figure VIII.23 SEM photomicrographs of 1:4 (PEG:PLA) SAA precipitated microparticles. (a) l, (b) G1 branched copolymer (magnification 20Kx).	111

Figure VIII.24 SEM photomicrograph of 1:4 (PEG:PLA) microparticles of l copolymer (magnification 40Kx).	112
Figure VIII.25 SEM photomicrographs of 1:8 (PEG:PLA) microparticles. (a) l, (b) G1 and (c) G2 copolymer (magnification 20Kx).	113
Figure VIII.26 PSD of 1:8 PEG-PLA copolymer particles obtained by SAA. Calculations were performed in terms of volumetric cumulative percentages from SEM images.	115
Figure VIII.27 DSC analyses of PEG-PLA microparticles: l linear 1:4, l linear 1:8, G2 branched 1:4.	117
Figure VIII.28 Comparison between ¹ H NMR (CDCl ₃ , 5°C) spectra related to the copolymer as received and the processed polymer.	118
Figure VIII.29 PEG microparticles obtained by SAA, at 20°C and 0.8 bar in the precipitator; 40°C and 67 bar in the saturator.	121
Figure VIII.30 PEG loaded 5% (w/w) of α-TCP. Microparticles obtained by SAA at 20°C and 0.82 bar in the precipitator; 40°C and 67 bar in the saturator (see Table VIII.12).	121
Figure VIII.31 PEG loaded 10% (w) of α-TCP microparticles obtained by SAA at 23°C and 0.8 bar in the precipitator; 40°C and 68 bar in the saturator (see Table VIII.12).	122
Figure VIII.32 Cumulative volumetric particle size distribution of the particles produced using SAA. Comparison between the particles loaded with different percentage of α-TCP.	122
Figure VIII.33 XRPD of untreated raw material and SAA produced PEG-αTCP microparticles at different αTCP percentage in liquid feed. See Table 12	123
Figure VIII.34 Thermograms: comparison among the analysis performed on the powder produced by SAA and the raw materials, PEG and α-TCP untreated.	124
Figure VIII.35 PLLA 120000 Da and PLLA 28000 Da, microparticles obtained by SAA at 40°C in the precipitator. The concentration of the solution is 20 mg/mL.	126
Figure VIII.36 Volumetric cumulative particle size distribution of PLLA microparticles produced by SAA.	127
Figure VIII.37 PEG-PLA copolymer produced by SAA at 40°C and 0.65 bar in the precipitator; 80°C and 87 bar in the saturator. Ramified copolymer G2 (right); Linear copolymer (left).	128
Figure VIII.38 Volumetric particle size distribution of microparticles of copolymer PLA-PEG obtained by SAA.	129

TABLE INDEX

Table I.1 Comparison of state and transport properties of gases, liquids, and supercritical fluids.	4
Table IV.1 Parameter of selected methods	16
Table IV.2 Raman frequency shifts of the vibrational Q-branch of some molecules (Lopez and Leipertz, 2010)	20
Table IV.3 Molar fraction used for the calibration of water-acetone mixture.	25
Table IV.4 Molar fraction used for the calibration of CO ₂ -acetone mixture.....	26
Table VI.1 Selected SAA experiments on PVP microparticles production using water as solvent. The nitrogen flow rate is 1380 NL/hr. (c: solute concentration; Q _{CO₂} : CO ₂ flow rate; T _p : precipitation temperature; p _p : precipitation pressure; T _m : saturator temperature; p _m : saturator pressure)50	
Table VI.2 Selected SAA experiments on PVP microparticles production using water-acetone mixture as solvent. The nitrogen flow rate is 1380 NL/hr. (c: solute concentration; Q _{CO₂} : CO ₂ flow rate; T _p : precipitation temperature; p _p : precipitation pressure; T _m : saturator temperature; p _m : saturator pressure).....	54
Table VI.3 Selected SAA experiments on PVP microparticles production using ethanol as solvent. The nitrogen flow rate is 1380 NL/hr. (c: solute concentration; Q _{CO₂} : CO ₂ flow rate; T _p : precipitation temperature; p _p : precipitation pressure; T _m : saturator temperature; p _m : saturator pressure)57	
Table VI.4 Mean diameter of PVP microparticles produced by SAA process, using different kind of solvents.....	61
Table VII.1 Vacuum rate	67
Table VIII.1. Properties of copolymers PLA-PEG. Mw, weight average molecular weight; Mn, number average molecular weight evaluated from NMR analysis [64]; PI, polydispersity index; Tm, melting temperature; ΔH, enthalpy	80
Table VIII.2 Selected experiments performed using SAA equipped with the vacuum system. (T _p : precipitation temperature; p _p : precipitation pressure; T _m : saturator temperature; p _m : saturator pressure; c: solute concentration; GLR: gas to liquid ratio; Q _{CO₂} : CO ₂ flow rate; Q _{LIQ} : solvent flow rate; Q _{N₂} : N ₂ flow rate).	83
Table VIII.3 Selected experiments performed using SAA equipped with the vacuum system. (T _p : precipitation temperature; p _p : precipitation pressure; T _m : saturator temperature; p _m : saturator pressure; c: solute	

<i>concentration; GLR: gas to liquid ratio; Q_{CO_2}: CO_2 flow rate; Q_{LIQ}: solvent flow rate; Q_{N_2}: N_2 flow rate).</i>	89
Table VIII.4 <i>Selection of SAA tests performed on PEG6000 and PEG10000: SAA operating conditions, and particle size. Solvent: acetone; CO_2 flow rate 9 g/min; liquid flow rate 3 mL/min; $GLR = 3.5$; nitrogen flow rate 690 NL/h; saturator operating conditions 40 °C and 67 bar.</i>	101
Table VIII.5 <i>Composition, molecular weight and architecture of the copolymers used for SAA process.</i>	109
Table VIII.6 <i>Results of selected experiments performed using SAA.</i>	112
Table VIII.7 <i>PS and PSD of PEG–PLA copolymer particles obtained by SAA.</i>	114
Table VIII.8 <i>PSD of PEG–PLA copolymer particles obtained by SAA, suspended in water and measured by DLS.</i>	115
Table VIII.9 <i>Comparison between copolymers untreated (u) and after micronization (m): molecular mass, percentage in mole of lactide in the copolymer, polydispersity index, melting point and melting enthalpy. (T_f: melting temperature; ΔH_f: enthalpy of fusion)</i>	116
Table VIII.10 <i>1H NMR analysis of the molecular mass and lactide percentage of the linear copolymer as received and after SAA process.</i> ...	119
Table VIII.11 <i>Evaluation of polydispersity index obtained using GPC. Comparison between copolymer as received and processed copolymer.</i>	119
Table VIII.12 <i>Selected experiments performed using SAA equipped with the vacuum system. (T_p: precipitation temperature; p_p: precipitation pressure; T_m: saturator temperature; p_m: saturator pressure; c: solute concentration; GLR: gas to liquid ratio; Q_{CO_2}: CO_2 flow rate; Q_{LIQ}: solvent flow rate; Q_{N_2}: N_2 flow rate).</i>	120
Table VIII.13 <i>Stability to hydrolysis, in water medium, of the vitamin in SAA formulation. The percentage was related to the content of vitamin loaded in polymer matrix.</i>	125

Abstract

Supercritical Assisted Atomization (SAA) is a very efficient process to micronize several kind of compounds, such as catalysts, polymers and active principles, also for pharmaceutical applications.

The process is based on the solubilization of a controlled amount of CO₂ in the liquid mixture, containing the compound to micronize, to reduce the cohesive forces, related to viscosity and surface tension, in order to obtain smaller particles than those could be obtained by process such as spray drying. The solution, formed by the liquid feed and supercritical CO₂, is injected through a nozzle in a precipitation chamber where fast and complete evaporation of the solvent from the droplets takes place. The particles are collected on a porous filter located at the bottom of the precipitator.

The SAA process has many applications in the micronization field, for this reason it is important to have a better comprehension of the principal mechanisms involved in the atomization process, to have a better control on particle size and distribution. For this reason the first part of this thesis work has been devoted to the evaluation of vapor liquid equilibria, involved in the saturator, and the fluid-dynamic of the jet break up. To evaluate the composition of the vapor-liquid phases, in the equilibrium conditions, a new approach, based on Raman Scattering, has been used. This technique, compared with the traditional used in thermodynamical studies, has the advantage to avoid any disturbance during the measurements. The systems aceton-CO₂ and acetone-water-CO₂ have been studied and the obtained compositions have been compared with results reported in literatures. The obtained results revealed that the vapor liquid equilibria detected by Raman are comparable with those obtained by other techniques. This part of the work was made in collaboration with SAOT institute in Erlangen (Germany).

It is also important to understand the role of supercritical CO₂ in the atomization process, from fluid-dynamic point of view. For this reason Supercritical Dissolved Gas Atomization (SGDA) plant is used to analyze the spray by laser diffraction technique. The SGDA experiments were performed using two solvents: water and ethanol. Supercritical CO₂ shows different behaviours with these solvents, since it is not soluble in water but it has a good affinity with ethanol.

The laser diffraction analysis reveals that the droplet mean diameter strongly depends on gas to liquid ratio (GLR), since at low value of GLR (lower than 2) bigger droplets were obtained, whereas at GLR higher than 2, smaller droplets were obtained and no variation in droplet mean diameter was observed at higher value of GLR. Droplets obtained using ethanol are smaller than those obtained using water, this because the solubilization of supercritical CO₂ in ethanol allows the decrease of cohesive forces due to viscosity and surface tension. Finally, the analysis of spray by laser

diffraction lets to make hypothesis on the regime of atomization: this is bubbly for low value of $GLR < 1$ and become annular for higher GLR . This because the amount of gas not dissolved in the liquid becomes considerably high and induces the nucleation of bubbles in the inner zone of the injector. Moreover, when $GLR > 1.5$ the SMDs are considerably smaller than the diameter of the injector (2 order of magnitude), accordingly to the hypothesis of annular flow.

On basis of the results obtained by the experiments on SGDA, a model compound was chosen for SAA micronization experiments, to enforce the theory previous discussed. Polyvinylpyrrolidone (PVP), that is a polymer that shows high affinity to polar solvents, was chosen as model compound. The solvents used were water, in which CO_2 is not soluble, a water-acetone mixture, where acetone is a non-solvent for PVP and enhance the affinity of the liquid feed with supercritical CO_2 , and ethanol, that has a good affinity with CO_2 .

The bigger particles (mean diameter ranged between 1.20 and 1.86 μm) were obtained using water as solvent, whereas using ethanol it was possible to produce the smallest particles (mean diameter ranged between 0.4 and 1.36 μm).

Moreover, using ethanol as solvent, it was possible to change the operating conditions in the saturator in order to work in the one phase region of vapor liquid equilibria diagram. Keeping constant saturator temperature at 40°C, it was demonstrated that increasing saturator pressure (from 70 to 165 bar) smaller particles were obtained. When saturator pressure is higher than 100 bar, CO_2 gives no contribution to a pneumatic effect, since, it is completely dissolved in the liquid. This fact could contribute to the demonstration that the main factor that influences the mean dimensions of the micro particles produced by SAA could be the amount of dissolved CO_2 ; indeed, when SC- CO_2 is completely solubilized in the liquid feed, smaller particles can be obtained.

Furthermore, considering the main limit of SAA, that is related to temperature to be used to remove the solvent, a new plant configuration is proposed. In the new plant configuration, a vacuum system is added downstream the precipitator to allow the decrease of precipitation pressure and, as a consequence, of temperature that is necessary for the evaporation of the solvent from the droplets. Indeed, high temperatures might be prohibitive for proteins, that could denaturate, and for polymers with low glass transition temperature, that could soften on the filter, inducing the blockage of the filter and the increase of pressure up to the safety limits.

The project of the vacuum system faced several problems: 1) the process is continuous: a continuous flow of nitrogen is fed into the precipitator, and this flow has to be removed from the vacuum pump ;2) particulate could be present downstream the porous filter, these particles could decrease the efficiency of the vacuum pumps and could damage the mechanical

components of the pumps; 3) condensables are present due to the evaporation of the solvent, these fluids could condensate in the vacuum chamber of the pump, inducing, again, the decrease of pump efficiency. For these reasons, a condenser was projected, to separate condensables before they enter in the vacuum pump. Moreover, it was chosen a piston pump with diaphragm. The diaphragm allows to separate the mechanical parts of the pump from the particles that might be present; this kind of pump is oil free, to avoid the formation of emulsions with condensables.

To validate the plant in the new configuration, experiments on protein and polymers with low glass transition temperatures were performed. For example, the micronization of Bovine Serum Albumin was successfully performed, setting 60°C and 0.8 bar in the precipitator. FTIR analysis demonstrated that operating at this temperature the denaturation of the protein was avoided. Other experiments were performed on micronization of polymers. The polymers chosen for these experiments are poly-L-lactide acid (PLLA), poly ethylene glycol (PEG) and copolymers PEG-PLA.

Comparing the results of SAA experiments on these polymers were performed also using the traditional plant configuration and it is interesting to see how the soften of the polymeric particles took place, this phenomenon induces the formation of membrane like structure on the filter. Instead, using the configuration operating at sub-atmospheric pressure in the precipitator, very regular and no agglomerated particles were obtained. Figure 1 shows an example of microparticles of PEG that can be obtained using the vacuum system:

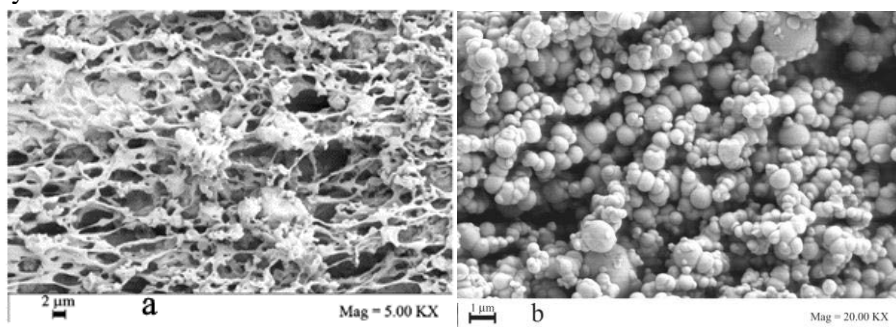


Figure 1 PEG microparticles obtained by SAA process using both plant configuration; (a) membrane like structure; (b) microparticles.

PEG has very low glass transition temperature (-20°C) and, as reported in literature, it is very difficult to obtain microparticles of this polymer. Using the new plant configuration, it was possible to decrease precipitation temperature down to 5°C, taking advantage of the Joule–Thomson effect, produced by the CO₂ expansion downstream the nozzle.

Generally, the mean dimension of the produced particles ranged between 0.2 and 3 μm. The diameter of the produced particles depends on operative

conditions used. For example, an increase of precipitation temperature induces the decrease of particle mean diameter; even the concentration of solute in the liquid feed has a no negligible effect on the particle size, since, at high concentration of solute bigger particles are produced.

In conclusion, in this PhD thesis, deeper understanding of the main mechanisms involved in the SAA process has been achieved. The Raman technique allows to evaluate the thermodynamic behavior of the system solvent-CO₂ that is generated in the saturator at the SAA operating conditions, that is of crucial importance in particle size control. The study of the atomization process, supported by SGDA experiments, gave an important comprehension of the role supercritical CO₂ in the spray formation. All these fundamental studies were also connected with particle formation, using SAA plant, giving a general interpretation of the main phenomena involved in micronization.

Furthermore, from the process point of view, a new layout for the SAA plant was proposed and validated. This new layout allows to operate under vacuum in the precipitator, in order to process, at low temperature, thermolabile compounds. Several compounds, for which the SAA micronization was unsuccessful, such as PLLA, copolymers PLA-PEG, PEG, were efficiently micronized, operating at low temperature, underlining the importance of this process improvement.

Chapter I

General statement on atomization

Supercritical assisted atomization (SAA) is a micronization process in which the supercritical fluid is used as an atomizing medium. The process is based on the solubilization of supercritical carbon dioxide (SC-CO₂) in the liquid solution composed by the solute, that must be micronized, and the solvent, that can be an organic solvent (ethanol, methanol, acetone) or water.

The process can be divided into three steps:

- Solubilization of SC-CO₂ in the solution (solvent and compound to be micronized);
- Injection of the expanded liquid;
- Drying of the droplets.

To understand the role of the supercritical fluid as atomization medium it is necessary to analyze the parameters that influence the atomization.

I.1. Drop and spray formation

Liquid jets are known to break up somewhere downstream the nozzle because of the interfacial forces between the jet and the surrounding air. When a liquid jet is discharged into air, disturbances on the jet surface will be increased because of the aerodynamic interactions between the jet and the surrounding ambient. The growth of these disturbances causes the liquid column to disintegrate into droplets soon after the discharge (Lefebvre, 1988). The most commonly accepted jet disintegration classification in the fluid mechanics literature dates back to the works of Ohnesorge (1936) (W, 1936) who combined the Reynolds (eq. 2) and Weber numbers and proposed a dimensionless group, Z (eq. 1), or the so-called Ohnesorge number shown as:

Chapter I

$$Z = \frac{\mu}{\sqrt{\rho\sigma D}} = \frac{\sqrt{We}}{Re} \quad (1)$$

where:

$$Re = \frac{\rho v D}{\mu} \quad (2)$$

v = jet velocity at injector exit;

ρ = density of the mixture formed by SC-CO₂ and the solution;

σ = surface tension solution/drying medium (nitrogen-N₂);

D = injector diameter ;

μ = viscosity of the mixture formed by SC-CO₂ and the solution.

Jet breakup phenomena have been divided into regimes that reflect differences in the appearance of jets as the operating conditions are changed. The regimes are due to the action of dominant forces on the jet, leading to its breakup, and it is important that these forces are identified in order to explain the breakup mechanism in each regime (Lin and Reitz, 1998). The case of a round liquid jet injected into a stagnant gas is shown in **Figure I.1**.

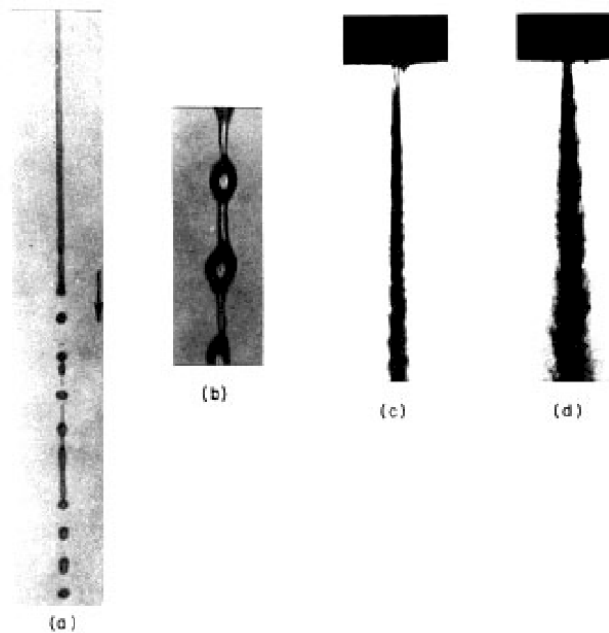


Figure I.1 (a) Rayleigh breakup. Drop diameters larger than the jet diameter. Breakup occurs many nozzle diameters downstream of nozzle. (b) First wind-induced regime. Drops with diameters of the order of jet

General statement on atomization

diameter. Breakup occurs many nozzle diameters downstream of nozzle. (c) Second wind-induced regime. Drop sizes smaller than the jet diameter. Breakup starts some distance downstream of nozzle. (d) Atomization regime. Drop sizes much smaller than the jet diameter. Breakup starts at nozzle exit. (Lin and Reitz, 1998)

Four main breakup regimes have been identified, that correspond to different combinations of liquid inertia, surface tension, and aerodynamic forces acting on the jet. These have been named the Rayleigh regime, the first wind-induced regime, the second wind-induced regime, and the atomization regime (Lin and Reitz, 1998). At low jet velocities, the growth of long-wavelength, small-amplitude disturbances on the liquid surface promoted by the interaction between the liquid and ambient gas is believed to initiate the liquid breakup process. The existence of these waves is clearly shown in **Figure I.1a** and b. For high-speed liquid jets, the breakup is thought to result from the unstable growth of shortwavelength waves (**Figure I.1c** and d).

The breakup drop sizes are on the order of the jet diameter in the Rayleigh and first wind-induced breakup regimes. The drop sizes are very much less than the jet diameter in the second wind-induced and atomization regimes. To categorize jet breakup regimes, it is necessary to consider the length of the coherent portion of the liquid jet or its unbroken length as a function of the jet exit velocity. Beyond the dripping flow regime, the breakup length at first increases linearly with increasing jet velocity, reaches a maximum, and then decreases.

The effect of the liquid viscosity (which appears in the Reynolds number, Re , and the Ohnesorge number, Z) is seen to reduce the wave growth rate and to increase the wave length significantly as the liquid viscosity increases. At low jet velocities (small Weber numbers) it is reasonable to assume that disruption of the jet occurs when the dominant wave amplitude is equal to the jet radius.

Beyond the first wind-induced breakup regime there is even more confusion about the breakup-length trends. Hiroyasu et al (1991) (Hiroyasu H, 1991) discovered discontinuous elongations and shortenings of the jet with changes in the jet velocity. These apparent anomalies are associated with changes in the nozzle internal flow patterns caused by separation and cavitation phenomena, which also exhibited hysteresis effects. Jets from cavitating nozzles were found to have very short breakup lengths.

Lin and Reitz (1998) (Lin and Reitz, 1998) have proposed the following expressions for different breakup regimes.

1. The Rayleigh breakup region:
 $We_L > 8$ and $We_g < 0.4$ or $1.2 + 3.41 Z^{0.9}$
2. The first wind-induced region:
 $1.2 + 3.41 Z^{0.9} < We_g < 13$
3. The second wind-induced region:

Chapter I

$$13 < We_g < 40.3$$

4. Atomization region

$$We_g > 40.3$$

We_g is the Weber number referred to the atomizing gas.

No account is made of nozzle internal flow effects in the above correlations.

I.2. Supercritical fluid based processes

A supercritical fluid is any substance at a temperature and pressure above its critical point. In these conditions the properties of the fluid significantly change, indeed it can effuse through solids like a gas, and dissolve materials like a liquid. In addition, close to the critical point, small changes in pressure or temperature result in large changes in density, allowing many properties of a supercritical fluid to be "fine-tuned". Table I.1 gives a comparison between density and viscosity of supercritical fluids and gas and liquid.

Table I.1 Comparison of state and transport properties of gases, liquids, and supercritical fluids¹.

	Density [kg/m^3]	Viscosity [$\mu Pa*s$]
<i>Gases</i>	1	10
<i>Supercritical Fluids</i>	100-1000	50-100
<i>Liquids</i>	1000	500-1000

When the atomizing medium is a supercritical fluid we can speak about supercritical fluid based micronization process. In these processes SC-CO₂ acts as co-solute. The main role of SC-CO₂ is to reduce surface tension and the viscosity to allow working in the atomization regime.

I.3. CO₂-Assisted Nebulization with a Bubble Dryer (CAN-BD)

Sievers et al. (Sievers et al., 2001) proposed a process in which the supercritical fluid and the liquid solution are fed in two separated lines and are mixed in a T-connection (**Figure I.2**) forming an emulsion. The emulsion is expanded in a nozzle downstream the T. The aerosol plume is dried as it mixes with nitrogen or air in the drying chamber where the formed particles are collected.

¹ <http://sfe.vemt.bme.hu/angol/supercritical.html>

General statement on atomization

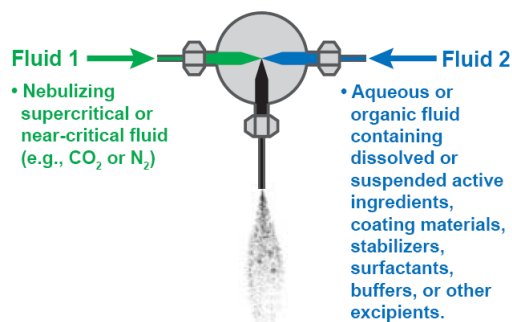


Figure I.2 Sketch of the functioning principle of CAN-BD (Sievers *et al.*, 2001).

Using this process it is possible to micronize some compounds:

- Active molecules: budesonide, naproxen, anphotericin B (Sievers *et al.*, 2003), ciprofloxacin HCl, moxifloxacin HCl, rifampicin, capreomycin, amikacin (Manion *et al.*, 2012);
- Proteins and enzymes: lysozyme, lactate dehydrogenase (Sievers *et al.*, 2001).

I.4. Supercritical Assisted Atomization (SAA)

In this process (Reverchon, 2002b) SC-CO₂ solubilizes in the liquid solution in a saturator, a high-pressure vessel loaded with stainless steel perforated saddles, characterized by a high surface, favouring the contact between CO₂ and the liquid solution, to promote the dissolution of the gaseous stream in the liquid. The operating conditions are selected considering the binary VLE diagram solvent-CO₂. The molar fraction of CO₂, the temperature and the pressure selected at the saturator ensure large CO₂ solubility in the liquid. However the presence of the solute could modify VLEs, as a consequence the solute could precipitate in the saturator because of the antisolvent effect. The antisolvent effect takes place because the operative condition are upon the mixture critical point, of the mixture CO₂-solvent, where the solvent, in which the compound to be micronized is solubilized, has high solubility in SC-CO₂ and the compound precipitates in the saturator. This condition must be avoided in order to have the success in SAA process.

The injection of the mixture through a nozzle allows the formation of the droplets, that are dried in the precipitation vessel by the inert gas flow (N₂).

The particles are collected at the bottom of the precipitation vessel on a porous filter (pores with a diameter less than 0.1 μm) while the condensable gases are separated from the inert gas by a separator vessel located downstream the precipitator.

SAA process has been used to micronize several compounds:

Chapter I

- Precursors of catalysts and salts: Yttrium Acetate, sodium chloride, aluminum sulfate, zirconyl nitrate hydrate (Reverchon et al., 2008b)
- Active molecules: carbamazepine, ampicillin trihydrate, triclazadol, dexamethasone (Reverchon et al., 2008b), Rifampicin (Reverchon and Antonacci, 2006a);
- Enzymes: Lysozyme (Adami et al., 2009);
- Polymers: Chitosan, HPMC (Reverchon et al., 2008b);
- Coprecipitates: Ampicillin-Chitosan and Ampicillina-HPMC (Reverchon et al., 2008b), BSA-Gentamycin Sulfate (Della Porta et al., 2010).

The produced particles have a regular morphology and generally a mean diameter between 0.5 and 5 μm . The PS (particle size) and the PSD (particle size distribution) can be controlled modifying the process parameters.

Cai et al (Cai et al., 2008) propose a process very close to SAA called SAA-HCM where a cavitation mixer is located upstream the saturator.

Some compounds have been micronized using SAA-HCM:

- levofloxacin-HCl (Cai et al., 2008)
- sodium cellulose sulfate (Wang et al., 2010)

The mean diameter of the produced particles is between 0.5 and 5 μm ; the morphology is regular.

On the bases of the experiments performed using SAA process, a first hypothesis on atomization mechanism was proposed. This hypothesis expects that the atomization takes place following two mechanisms: the first step is the production of primary droplets at the exit of the nozzle by pneumatic atomization. The second step is due to the fast release of CO_2 , from the inner of the droplets during decompression: a secondary atomization occurs, that produces smaller secondary droplets (Adami et al., 2009), as schematically reported in **Figure I.3**.

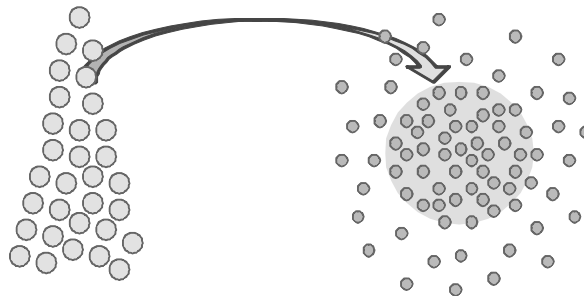


Figure I.3 Sketch of the pneumatic atomization and decompressive atomization.

However this hypothesis has not been verified. For this reason some experiments will be performed in this thesis work, to study spray formation at the exit of the injector.

General statement on atomization

After the formation of the droplets the drying of the solvent takes place; the drying is driven by the continuous flow of a warm inert gas (N_2). The solvent is continuously removed by the inert gas (N_2) flow. It is possible to apply the theory proposed by Vehring on the drying process that takes place during spray drying process (Vehring et al., 2007). When the solvent is dried, the solute reaches the saturation, forms a solid matrix through which the solvent diffuses before leaving the droplet. If the diffusion of the solvent through the solid matrix is not fast and the solute to micronize has a large solubility, precipitation takes place later than the evaporation process, and the solute precipitates homogeneously inside the drop. The resulting dry particles are expected to have little or no void space and a density close to the density of the dried bulk material (**Figure I.4**).

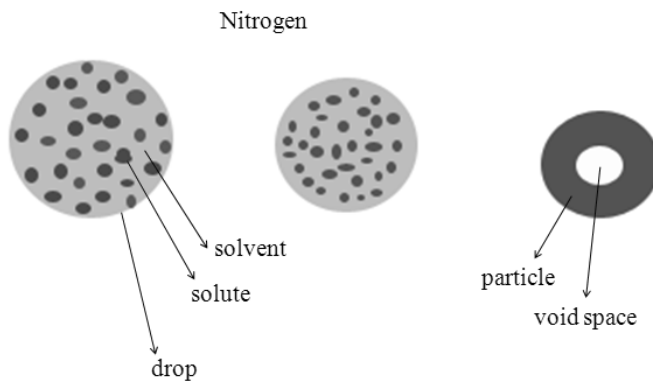


Figure I.4 Sketch of the formation of particles from drops at low evaporation rate.

If the diffusion of the solvent is fast and the solute solubility is small, the resulting particles will have a considerable void space (**Figure I.5**). These phenomena are influenced by the precipitation temperature and pressure (Vehring et al., 2007).

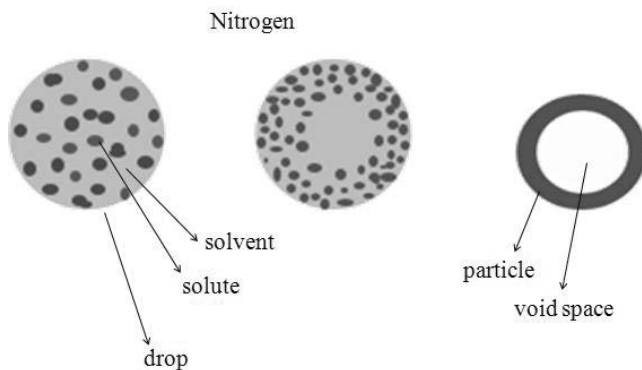


Figure I.5 Sketch of the formation of particles from drops at high evaporation rate.

Chapter I

SAA technique is more efficient than the traditional similar micronization techniques, that do not use supercritical fluid as atomized medium, because it is possible to obtain smaller particles (Reverchon, 2002b); particle size distribution can be changed according to the used operative parameters. Moreover it is possible to use several kinds of solvents; if water is used, the process can be clearly considered environmental friendly and it is possible to micronize a significant variety of pharmaceutical compounds that are water soluble. SAA process allows to obtain microspheres formed by a carrier, like polymers or proteins, and an active principle, that can be efficiently used in the controlled release (Reverchon et al., 2008b, Della Porta et al., 2010).

Chapter II

Aim of the work

SAA has many application, since it can be used to micronize many compounds of chemical and pharmaceutical interest. Moreover, it is possible to control particle size and crystalline degree, choosing appropriate operative conditions.

However, up to now, the mechanisms involved in SAA process are not well understood. Particularly, it could be interesting to understand how supercritical CO₂ acts as atomizing medium.

The aim of this work can be divided in three steps, as following indicated:

- study of vapor liquid equilibria in the saturator;
- characterization of the spray at the exit of the nozzle, downstream the saturator;
- improvement of precipitator performance decreasing the precipitation temperature

The evaluation of vapor liquid equilibrium is fundamental to choose the operating conditions in the saturator, where CO₂ is mixed with the liquid feed. Generally speaking, literature is poor of vapor liquid equilibrium data for the system CO₂-solvent at high pressure, especially when mixture of solvents are used. To overcome this limitation, an innovative technique is proposed to evaluate the concentration of the compounds in the two phase region of vapor liquid equilibria diagram. This technique allows to obtain concentration without disturbing the equilibria between the phases.

Up to now, it is believed that the atomization involves two mechanisms: the pneumatic atomization and the decompressive atomization, as indicated in the previous chapter. However no experiments were performed to verify this atomization mechanism. In this work supercritical dissolved gas atomization apparatus is proposed to analyze the spray at the exit of the injector, using laser diffraction technique.

The last goal of this work will be to enlarge the application field of SAA process to the micronization of thermosensitive compounds. For this purpose, it is necessary to project and implement a vacuum system that

Chapter II

operates downstream the precipitator, in order to reduce the precipitation pressure and to perform the drying of the drops at lower temperatures.

Chapter III

Analytical methods

III.1. Analysis on morphology

III.1.1. Scanning electron microscope field emission

A field-emission scanning electron microscope (FE-SEM model LEO 1525; Carl Zeiss SMT AG, Oberkochen, Germany) was used to study the morphology of the produced particles. Samples were fixed over an adhesive carbon tab, previously stuck to an aluminium stub and covered with gold (layer thickness 250 Å) using a sputter coater (model 108 A; Agar Scientific, Stansted, UK).

III.1.2. Particle size analysis

Particle size (PS) and particle size distribution (PSD) were measured from FE-SEM photomicrographs using the Sigma Scan Pro Software (release 5.0, Aspire Software International Ashburn, VA). Approximately 1000 particles were measured for each particle size distribution calculation. Histograms representing the particle size distribution were fitted using Microcal Origin Software (release 8.0, Microcal Software, Inc., Northampton, MA). Moreover, the produced microparticles were characterized by the dynamic laser scattering (DLS) method using a Nanosizer (NanoZS Malvern Instrument, UK) equipped with a He-Ne laser operating at 4.0 mW and 633 nm, for measuring the hydrodynamic diameter of the particles. PLLA and PLA-PEG microparticles were dispersed in a water solution containing 0.1 wt% of a stabilizing agent, sodium dodecyl sulphate (SDS); BSA microparticles were dispersed in chloroform; PEG and PEG- α Tocopherol microparticles were dispersed in cold acetone and the analysis was performed at 10°C; PVP was dispersed in ethyl acetate.

III.2. Solid state analysis

III.2.1. X-Ray Diffractometry

Solid state analysis of the samples was performed using an X-ray powder diffractometer (model D8 Advance; Bruker AXS, Madison, WI) with a Cu sealed tube source. Samples were placed in the holder and flattened with a glass slide to ensure a good surface texture. The measuring conditions were: Ni-filtered Cu K α radiation, λ 1.54 Å, 2θ angle ranging from 5 to 60 with a scan rate of 3 s/step and a step size of 0.028.

III.2.2. Differential scanning calorimeter (DSC)

Thermograms of the samples were obtained using a differential scanning calorimeter (DSC, model TC11, Mettler Toledo, Inc., Columbus, OH). Fusion temperature and enthalpy were calibrated with an indium standard (melting point, 156.6°C). 10 mg of the sample was accurately weighed, crimped in an aluminum pan, and heated from 25 to 195°C under a nitrogen purge at 10°C/min.

III.3. Stability and denaturation analysis

III.3.1. Protein stability: FTIR

Fourier transform infrared (FT-IR) spectra were obtained via M2000 FTIR (MIDAC Co, Costa Mesa, CA), at a resolution of 0.5 cm⁻¹. The scan wavenumber range was 4,000–400 cm⁻¹, and 16 scan signals were averaged to reduce the noise. The powder samples were ground and mixed thoroughly with potassium bromide (KBr) as infrared transparent matrix. KBr discs were prepared by compressing the powders in an hydraulic press. All spectra were smoothed using a 13-point Savitzky–Golay smoothing function to remove white noise.

III.3.2. Dissolution rate test

Dissolution tests was performed on BSA microparticles. 10 mg of material were dissolved in distilled water (100 mL) at 25°C under stirring (300 rpm). The dissolution time were investigated measuring the increase of concentration of BSA in the solution mentioned above. This concentration was determined by an UV–Vis spectrophotometer (mod. Cary 50, Varian, Palo Alto, CA) measuring BSA absorbance (280 nm).

III.3.3. Solvent residue analysis

Chloroform residue in PLLA microparticles, produced by SAA, was measured by a headspace sampler (mod. 7694E, Hewlett Packard, USA) coupled to a gas chromatograph (GC) interfaced with a flame ionization detector (GC-FID, model 6890 GC-SYSTEM, Hewlett Packard, USA). Chloroform was separated using two fused-silica capillary columns connected in series by press-fit: the first column (model Carbowax EASYSEP, Stepbios, Italy) connected to the detector, 30 m length, 0.53 mm i.d., 1 μ m film thickness and the second (model Cp Sil 5CB CHROMPACK, Stepbios, Italy) connected to the injector; 25 m length, 0.53 mm i.d., 5 μ m film thickness. GC conditions were the one described in the USP 467 Pharmacopoeia with some minor modifications: oven temperature from 45 to 210 °C for 15 min. The injector was maintained at 135°C (split mode, ratio 4:1), and helium was used as the carrier gas (5 ml/min). Head space conditions were: equilibration time, 30 min at 95°C; pressurization time, 0.15 min; loop fill time, 0.15 min. Head space samples were prepared in 20 ml vials filled with internal standard DMI (3 ml) and 500 mg of NaCl and water (0.75 ml) in which PLLA particles were suspended.

III.4. Structural analysis

III.4.1. H and C NMR analysis

Spectra were recorded on a Bruker Advance 400MHz spectrometer at 298 K. The samples were prepared by introducing 20 mg of copolymer in 0.5mL of CDCl₃ into a NMR tube (0.5mm outer diameter). Tetramethylsilane (TMS) was used as internal reference.

III.4.2. Gel Permeation Chromatography (GPC)

GPC chromatograms were recorded on the system equipped with a Waters 1525 binary pump, a Waters 2414 RI detector and four Styragel columns (range 10³–10⁶ Å). The measurements were carried out at 25°C, using THF as eluent (1.0 mL/min) and polystyrene standards as references.

III.4.3. High-performance liquid chromatography (HPLC)

Vitamin loading was investigated by dissolving 5 mg of powder in 2.5 mL (5% α -TCP) and 5 mL (10% α -TCP) of methanol, and vitamin concentration were monitored at 292 nm in a HPLC system, using methanol/acetonitrile (25/75 v/v) as eluent in a Spherisorb ODS-2 column at a flow rate of 1.5 ml/min.

Chapter III

The stability to hydrolysis of the vitamin in water medium was investigated dissolving the powder produced by SAA in water. 1 mL of the resulted solution was eluted in ethanol (50/50 v/v) and the concentration of the vitamin was measured using HPLC analysis as previously discussed.

Chapter IV

Vapour liquid equilibria measurements

The knowledge of equilibrium states of binary or multicomponent mixtures is of high interest in chemical engineering, to know the composition of the mixture that is formed in the saturator of the SAA plant.

In SAA processing, the choice of the proper conditions in the saturator is fundamental to produce microparticles. Indeed, the jet-breakup in form of atomization process depends on the quantity of CO₂ solubilized in the liquid solution contained in the saturator. Assuming that the solute has not a relevant influence on the vapor liquid equilibria (VLEs), the formation of an homogeneous mixture is assured if the SAA operative point is located in the liquid region of the VLE diagram for the binary system solvent-CO₂ (Reverchon, 2002b, Wang et al., 2010). However, literature is poor of data which respect to vapor liquid equilibria at high pressure. This is due to the difficulties to measure the composition of two phase mixture, at high pressure, without interfering the system.

Different methods can be used to evaluate the equilibrium data. For example, bubble-point pressures could be determined from the relationship between the pressure and the inner volume of the cell used to mix the compounds (Sato et al., 2010, Campos et al., 2009). Another possibility is to measure the concentration in the phases by gas chromatographic analysis. The main limitations of these classical techniques are: possible disturbance of the equilibrium by the extraction of the probe, changes of the probe state between probe extraction and probe analysis, and the time delay between probe extraction and analysis (Stratmann and Schweiger, 2002). Noninvasive spectroscopic methods, such as Raman (Kiefer, 2010) or NIR spectroscopy (Stratmann and Schweiger, 2002), do not have this kind of drawback. In this chapter the evaluation of the composition of system CO₂-solvents by Raman spectroscopy is proposed.

IV.1. Raman Scattering

Laser optical measurement techniques are very useful for the determination of properties, such as composition of a mixture, because they do not affect the medium and have a short measuring time.

Furthermore, due to the particular type of interaction between laser photons and involved molecules, the Raman scattered light is specific to each molecule. Therefore it is possible to use this technique to detect simultaneously all components of a gas with only one laser source.

However, when light interacts with a material several physical processes take place. They are characterized from different frequencies and cross section, as reported in **Table IV.1**.

Table IV.1 Parameter of selected methods

<i>Method</i>	<i>Scattering centre</i>	<i>Frequency</i>	<i>Scattering cross section</i>
			$\frac{d\sigma}{d\Omega}$ in $\left[\frac{cm^2}{sr} \right]$
Mie	\varnothing 10 μ m particle	ν_0	10^{-7}
Mie	\varnothing 0,1 μ m particle	ν_0	10^{-13}
Fluorescence	molecule	$\nu_F < \nu_0$	$10^{-19} - 10^{-24}$
Rayleigh	molecule	ν_0	10^{-27}
Raman	molecule	$\nu_0 \pm \Delta\nu_R$	$10^{-30} - 10^{-31}$
CARS	molecule	$\nu_0 + \Delta\nu_R$	$10^{-21} - 10^{-25}$

The linear Raman scattering is the weakest scattering process of all processes listed (see **Table IV.1**).

Every motion of a molecule can be regarded as a combination of translational, vibrational and rotational motions. The translational motion is not relevant in molecular spectroscopy, therefore, it will be neglected.

In many cases, the total energy of a molecule can be defined in a good approximation as the sum of electronic, vibrational and rotational energies. Electronic states are characterized with the main quantum number (n). Rotational and vibrational energy levels are indicated with the rotational quantum number (J) and the vibrational quantum number (v), respectively.

Figure IV.1 shows schematically the potential curves of the electronic ground state and the first two excited electronic states for a diatomic molecule. Considering molecules not having extended conjugated electronic system, electronic excitations normally cannot occur if light in the visible wavelength range is used because its energy is not high enough to excite this kind of transitions.

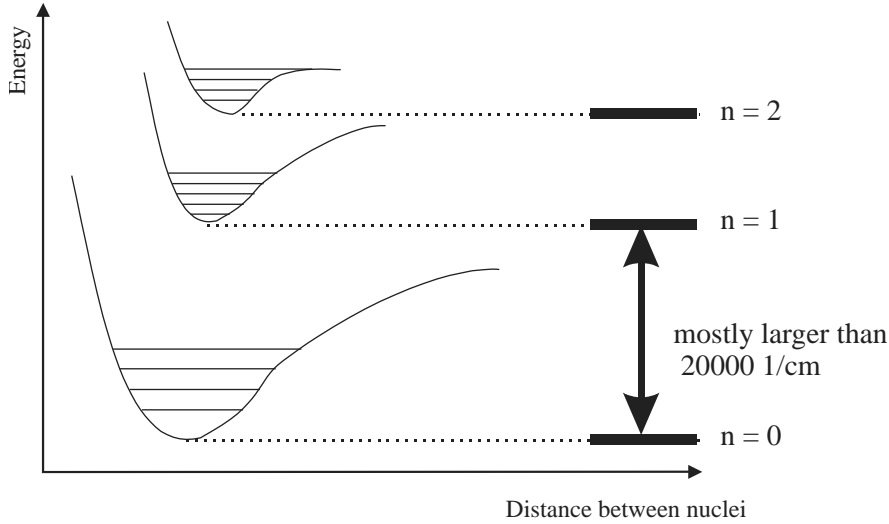


Figure IV.1 Energy level of diatomic molecules (Schrader, 2008)

Normal vibration is defined as a vibration, at which all mass points of the system vibrate with the same frequency and a given phase relation. A normal vibration can be excited without exciting another normal vibration.

The vibrational energies are normally determined via quantum mechanical calculations. However, the vibrations of a simple linear diatomic molecule can be explained in a first approximation as those of a harmonic oscillator.

The vibrations of the harmonic oscillator are not damped. Only certain states of vibration are possible.

This description leads to a quantization of the vibrational states (term values) $G(v)$. For the harmonic oscillator the vibrational energy is dependent on the vibrational quantum number v :

$$\frac{G(v)}{h \cdot c} = G(v) \propto \left(v + \frac{1}{2} \right) \quad (3)$$

Where h is the Planck's constant and c is the speed of light. The energy levels of the harmonic oscillator are equidistant. Reality is much better described by the inharmonic potential. Especially for large deviations from the equilibrium state, the distances between energy levels decrease with increasing vibrational quantum number v .

$$\frac{G(v)}{h \cdot c} = G(v) \propto (-1)^{n+1} \left(v + \frac{1}{2} \right)^n \quad (4)$$

Chapter IV

Similarly to the harmonic oscillator one uses as a first approximation for the calculation of the rotational levels a descriptive and easy calculable object: the rigid rotator, which is characterized by a fixed distance of its mass points.

As quantum mechanics is normally used for the calculation of the energy levels, one gets a quantization of the rotational states $F(J)$. The correlation between the rotational term value F and the rotational quantum number J is given by:

$$\frac{U_{rot}(J)}{h \cdot c} = F(J) = \frac{h}{8\pi^2 c I_e} J(J+1) = B_e \cdot J \cdot (J+1) \quad (5)$$

U_{rot} is the internal rotational energy.

The value B_e is known as the rotational constant and it is indirect proportional to the moment of inertia I_e of the considered molecule.

(Hint:
$$I_e = \mu R^2 = \frac{m_1 m_2}{m_1 + m_2} R^2 \quad (6)$$

m is the mass and μ is the reduced mass.

From the equation of moment of inertia results a high rotational energy for light molecules and a small rotational energy for heavy ones.

The fact that the distances of specific rotational levels for different vibrational states are not equal (i.e. $F(v, J) \neq F(v', J)$) means that the coupling of vibration and rotation cannot be neglected. The interaction of the nucleus motions has to be taken into account with the definition of mixed, terms v and J containing. The vibration of molecules is much faster than the rotation.

IV.2. Description of Raman spectroscopy

A photon of a laser ($h\nu_0$), which has not enough energy to be absorbed by the molecule, can be scattered elastically, which means that after the scattering process the molecule is back in its initial energy level (*Rayleigh scattering*). In this case, the scattered photon has the same energy as the exciting photon ($h\nu_0$). Less probably, the photonmolecule does not return to the initial state but change its vibrational or rotational energy. This process is named *Raman scattering*, and the scattering is inelastically. In this case, the molecule occupies a higher energy level after the scattering process than before (see **Figure IV.2**).

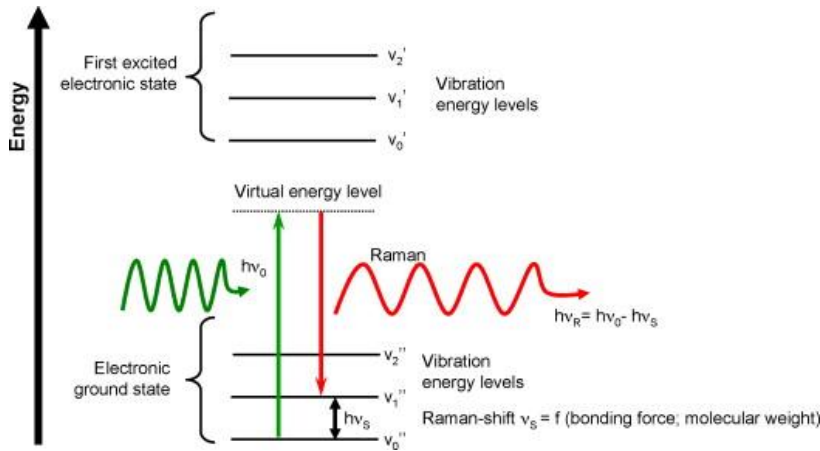


Figure IV.2 Raman transitional scheme (Dowy et al., 2009)

Due to energy conservation, the energy of the scattered photon ($h\nu_R$) is lower than that of the exciting photon ($h\nu_0$), and the energy difference of the two photons is equal to the energy difference of involved energy levels of the scattering molecule. This energy difference is also called Raman shift, is specific for different molecules, and is given in the energy unit of wavenumbers [cm^{-1}].

The Raman frequency shift gives also the difference between the internal energy U of the scattering molecule (in wave numbers [cm^{-1}]) before and after the scattering process:

$$\Delta\tilde{\nu}_R = \frac{U_2 - U_1}{hc} = T_2(\nu_2, J_2) - T_1(\nu_1, J_1) \quad (7)$$

whereby T_1 and T_2 are the so called term values in wave numbers of the states (1) and (2).

If excitation is made with a laser, the energy of the exciting photons is well known. By detecting the energy of the scattered photons, the Raman shift can be calculated and is specific for each molecule. Therefore, Raman spectroscopy is species sensitive. Furthermore, the number of the inelastically scattered photons of a certain Raman shift is proportional to the number of molecules of this species present in the measurement volume, which enables quantitative composition measurements in mixtures of molecules which have different Raman shifts.

The rotational-vibrational transitions of different species appear mostly clearly separated in the Raman spectra. This makes possible a simultaneous multi-species detection with a simultaneous identification of the Raman lines by means of their characteristic Raman shifts. **Table IV.2** gives an overview of the Raman frequency shifts of the vibrational Q-branch of some important molecules for the flow and combustion diagnostics.

Table IV.2 Raman frequency shifts of the vibrational Q-branch of some molecules (Lopez and Leipertz, 2010)

molecule	transition	$ \Delta\tilde{\nu} _R$ [cm ⁻¹]	molecule	transition	$ \Delta\tilde{\nu} _R$ [cm ⁻¹]
SO ₂	ν_1	519	N ₂	$\nu = 0 \rightarrow \nu = 1$	2331
Cl ₂	$\nu = 0 \rightarrow \nu = 1$	557	H ₂ S	ν_1	2611
C ₆ H ₆	ν_2	992	C ₁₂ H ₂₆	C-H (max.)	2842
C ₂ H ₆	ν_3	993	C ₁₆ H ₃₄	C-H (max.)	2851
SO ₂	ν_2	1151	C ₇ H ₁₆	C-H (max.)	2875
N ₂ O	ν_1	1285	HCl	$\nu = 0 \rightarrow \nu = 1$	2886
CO ₂	$2\nu_2$	1286	C ₈ H ₁₈	C-H (max.)	2910
C ₂ H ₄	ν_3	1342	CH ₄	ν_1	2914
CO ₂	ν_1	1388	C ₂ H ₄	ν_3	3019
O ₂	$\nu = 0 \rightarrow \nu = 1$	1556	CH ₄	ν_3	3020
C ₂ H ₄	ν_2	1623	C ₆ H ₆	ν_1	3070
NO	$\nu = 0 \rightarrow \nu = 1$	1876	NH ₃	ν_1	3334
C ₂ H ₂	ν_2	1974	C ₂ H ₂	ν_1	3374
CO	$\nu = 0 \rightarrow \nu = 1$	2143	H ₂ O	ν_1	3652
N ₂ O	ν_3	2224	H ₂	$\nu = 0 \rightarrow \nu = 1$	4156

For spontaneous or linear Raman scattering there is a linear correlation between the polarization P and the exciting electric field E. The parameter α is the polarizability tensor.

$$P = \epsilon_0 \alpha E \quad (8)$$

IV.3. Concentration measurements

One of the outstanding properties of the linear Raman scattering is that nearly all molecules have Raman active transitions and are, therefore, measurable. Exceptions are merely the noble gases because they are monoatomic molecules and cannot perform molecule vibrations or rotations.

The direct proportional correlation between the Raman signal intensity and the concentration of the available material in the measurement volume can be extracted directly from the working equation.

The determination of the concentration can be made in absolute and relative way. \dot{U}

If all setup and molecule specific parameters are combined in the working equation to one constant C_i , the following equation results:

$$I_i = C_i I_0 n_i \quad (9)$$

If the laser power does not change, this can also be included in the constant C_i . The determination of this proportionality constant is made by a calibration of the setup with given temperature and concentrations.

A more complex method is the generation of a calibration curve in the expected concentration region.

IV.4. Apparatus and methods

The main components of the experimental setup are: the continuously working laser system; optical components (mirrors, lenses, optical fiber), which are built in a compact-unit-cage; a spectrometer, which is equipped with a grating and a CCD-chip; as well as an optically accessible measuring cell, in which two liquids are mixed.

The laser to be used is a diode-pumped, frequency-doubled CW-laser (continuous-wave laser) emitting light at a wavelength of 532 nm. The emitted laser radiation is polarized ($> 100:1$ perpendicular) and the laser beam is 2 mm in diameter. The maximum laser output power is 250 mW.

A sketch of the optical setup to be used in this practical course is shown in **Figure IV.3**. By means of several mirrors and lenses, the laser beam is conducted to the point of measurement. Through a combination of a plano-concave lens and a plano-convex lens, the laser outlet (initial) diameter is expanded by 16.67 times. Further, the expanded beam is reflected on a dichroic (mirror) beam splitter at 45° angle of incidence. This beam splitter is highly reflective for laser light at 532 nm and highly transmissive for longer wavelengths. Using a spherical lens with a focal length of 100 mm, the laser beam is focused into the measurement volume.

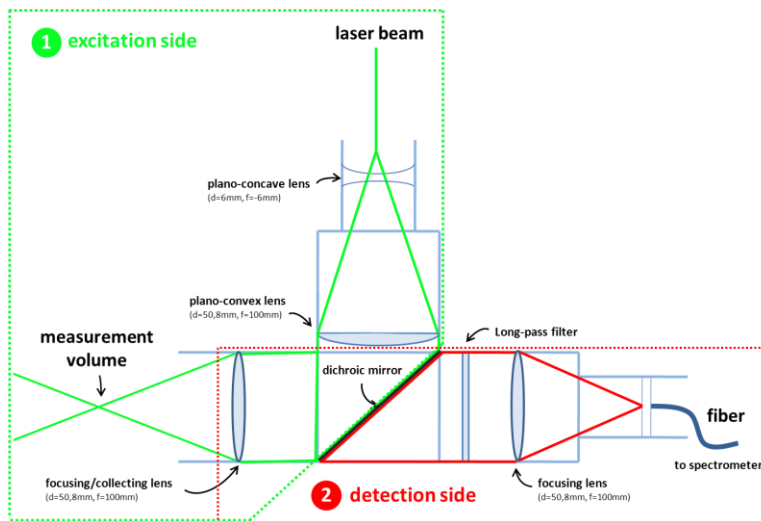


Figure IV.3 Raman optical setup (Lopez and Leipertz, 2010)

Chapter IV

By using this setup, the scattering signals are collected in backscattering direction, i.e. 180° to the direction of propagation of the laser beam. It means that the lens used to focus the laser beam into the measurement volume is also used to collect the signals. Then, the elastically scattered light ($\lambda = 532\text{nm}$) is reflected on the dichroic beam splitter and the inelastically scattered light ($\lambda > 532\text{nm}$), transmitted. In order to filter the elastically scattered light, which may not be suppressed by the dichroic beam splitter completely, a long-pass filter (RazorEdge filter) is additionally mounted in the detection cage in order to avoid any damage of the CCD-chip. Through a further lens ($f = 100\text{ mm}$), the signals are focused exactly in the core of the optical fiber, which transmits the signals to the spectrometer. The optical fiber has a round-to-linear configuration, i.e. 7 single fibers with a core diameter of $100\text{ }\mu\text{m}$ each are bundled together, such that the fiber has a round configuration at one end (for signal collection) and a linear configuration at the other (to spectrometer).

A spectrometer is used to record the spectrally resolved signals. It has no entrance slit, so the linear side of the fiber bundle works as a slit and determines the spectral resolution (slit width = $100\text{ }\mu\text{m}$). The CCD-chip of the spectrometer is a Hamamatsu back-thinned detector with a 2-D arrangement of pixels (1044 horizontal x 64 vertical) that is responsive from 200-1100 nm. The detector's columns are binned, or summed, inside the detector prior to the readout process, thereby minimizing readout noise. The pixel size is $24.6\text{ }\mu\text{m}$ square. The time-dependent resolution is given by the exposure time of the detection system.

IV.4.1. Variable volume high pressure cell.

Solubility measurements were performed in a variable volume high pressure equilibrium cell (EC 700, Separex). This cell is equipped with a stirrer which allows an optimal mixing of the phases, four sapphire windows and heating jacket which allows operating at constant temperature. The cell has an internal volume which can vary between 25-50 mL and can withstand pressures of up to 70 MPa and temperatures up to 423 K. The main components of this configuration are two syringe ISCO pumps (model 260D from Teledyne, Lincoln, NE) to introduce CO_2 and the solvent inside the cell. A schematic diagram of the equipment is presented in **Figure IV.4**.

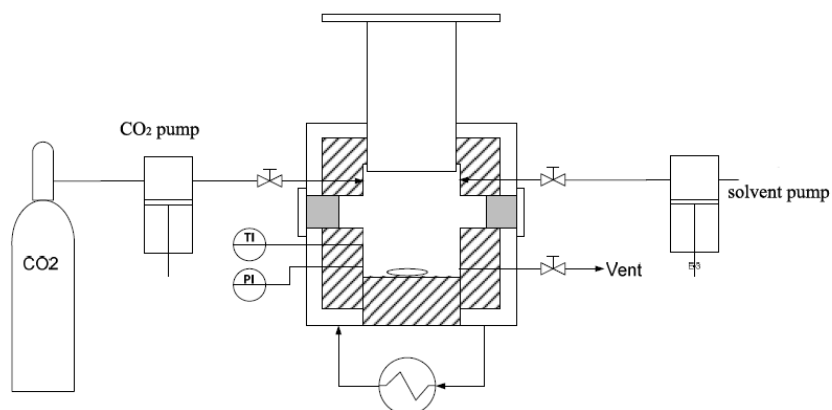


Figure IV.4 Variable volume high pressure cell (*Varona et al., 2012*)

IV.5. Results and discussion

The equilibria for systems acetone-CO₂ and acetone-water-CO₂ were studied. The Raman detection for binary system were used to validate the technique. Moreover, new equilibria data were obtained, on the ternary system, for which poor data exist in literature.

IV.5.1 Calibration curve

The Raman shift is characteristic for each bond, as mentioned above. **Figure IV.5** shows the Raman shift for acetone, water and CO₂.

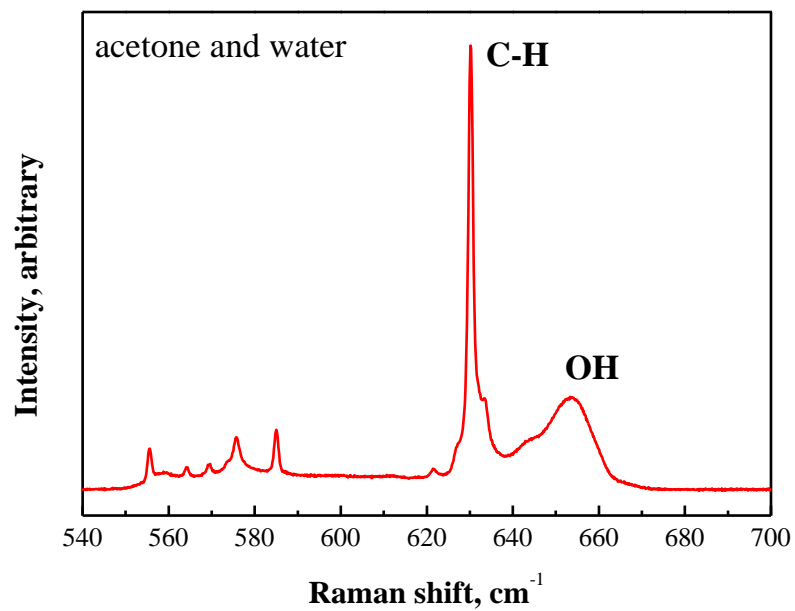
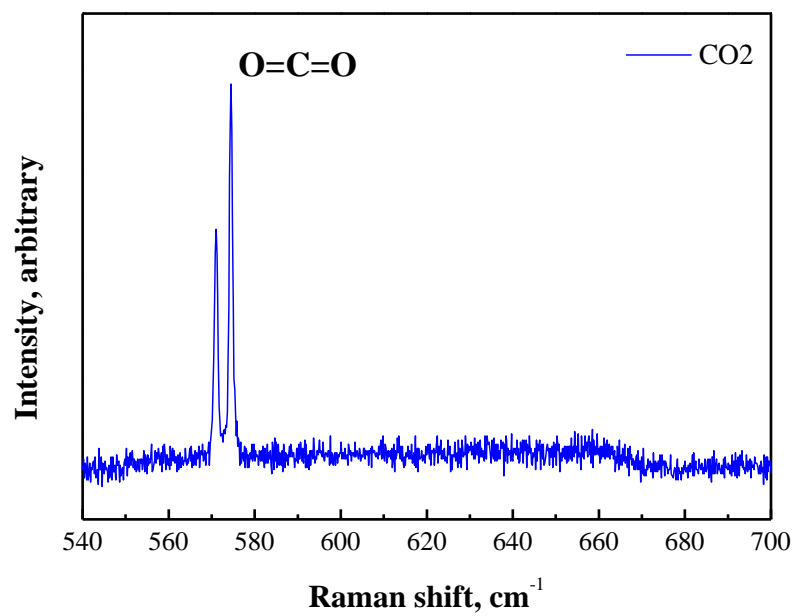


Figure IV.5 Raman spectra for acetone, water and CO₂.

Vapour liquid equilibria measurements

To evaluate the relation between the intensity of Raman shift and the composition of the system a calibration was necessary. Two calibration curves were calculated: the first was related to the system CO₂-acetone and the second to the system water-acetone. The data used to calibrate were obtained when the systems were in homogeneous phases.

Variable volume high pressure cell was filled with a mixture of water and acetone, for which the composition was well known. The Raman scattering was applied to different mixtures, containing the following molar fraction (see **Table IV.3**) of each component.

Table IV.3 Molar fraction used for the calibration of water-acetone mixture.

	Acetone	Water
	0.25	0.75
Molar fraction	0.40	0.60
	0.50	0.50
	0.70	0.30

Each composition was correlated with Raman shift intensity and the calibration curve, evaluated at 60°C and 70 bar is reported **Figure IV.6**:

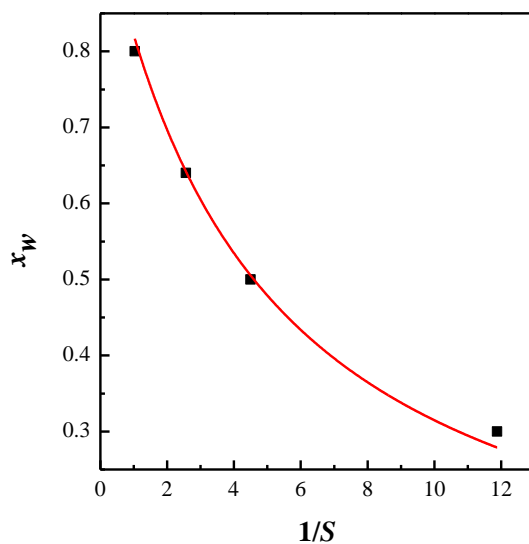


Figure IV.6 Calibration curve for the system water-acetone.

The following equation was applied to fit experimental data:

Chapter IV

$$x_W = \frac{1}{1 + k_W \frac{1}{S_W}} \quad (10)$$

x_W molar fraction of water

k_W evaluated constant for the mixture water-acetone

S_W intensity of water

The calibration was made also for the system CO₂-acetone. **Table IV.4** reports molar fractions used to calibrate.

Table IV.4 Molar fraction used for the calibration of CO₂-acetone mixture.

	Acetone	CO ₂
	0.25	0.75
<i>Molar fraction</i>	0.40	0.60
	0.50	0.50
	0.75	0.25

Different calibration curves were evaluated since close to the mixture critical point a small difference in pressure may induce a non negligible change in intensity. **Figure IV.7** shows the calibration curve for the mixture CO₂-acetone at 60°C and 100 bar, but the calibration was also evaluated at 80°C and 90 bar, that are the operative conditions used for SAA experiments.

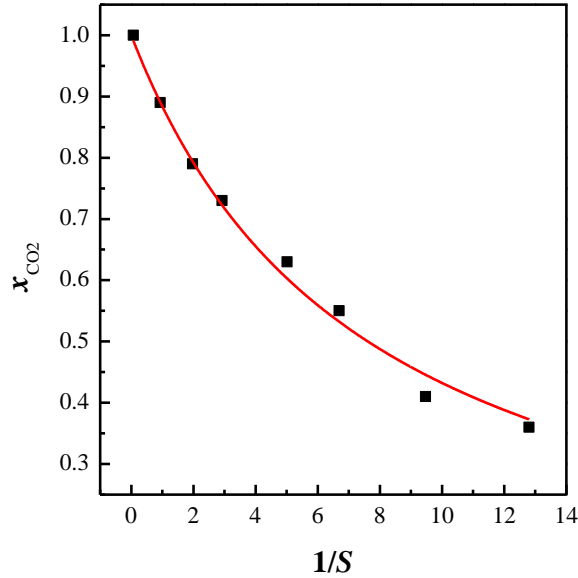


Figure IV.7 Calibration curve for the system CO₂-acetone at 60°C and 100 bar.

The following equation was applied to fit experimental data:

$$x_{CO_2} = \frac{1}{1 + k_{CO_2} \frac{1}{S_{CO_2}}} \quad (11)$$

x_{CO_2} molar fraction of CO₂

k_{CO_2} evaluated constant for the mixture CO₂-acetone

S_{CO_2} intensity of water

IV.6. Equilibria CO₂-acetone.

To validate the non invasive technique, based on Raman scattering, for the detection of the compositions in different phases, the equilibria for the system CO₂-acetone at 60°C was taken into account, since many literature data exist and it was possible to make a comparison. **Figure IV.8** shows a comparison between data reported in literature (Sato et al., 2010, Han et al., 2005, Adrian and Maurer, 1997) and data detected by Raman scattering based technique:

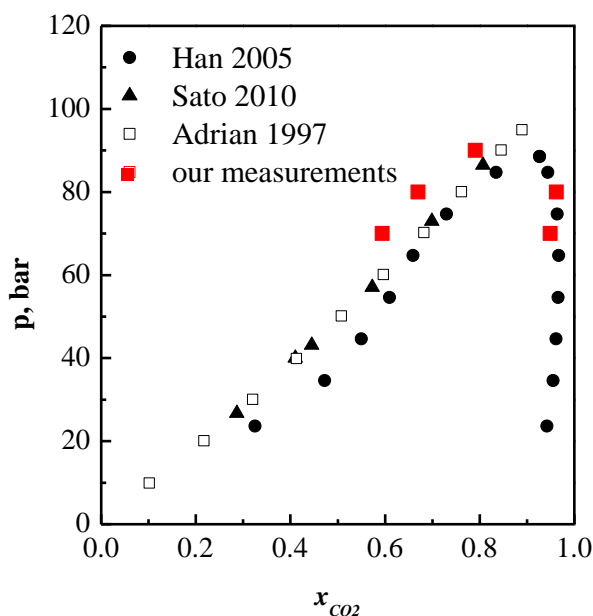


Figure IV.8 Ebuliubrium data for the system CO_2 -acetone at $60^\circ C$. Comparison between data reported in literature (Sato *et al.*, 2010, Han *et al.*, 2005, Adrian and Maurer, 1997) and data detected by Raman scattering (our measurement).

Data obtained by Raman scattering based technique are very similar to those reported in literature. The small differences are probably due to the standard deviation related to the different techniques used for the detection.

IV.7. Equilibria CO_2 -acetone-water.

It is very difficult to detect the composition at equilibria for ternary systems without perturbation of the equilibria. Raman scattering based technique allows to detect the composition of the three compounds in the phases in the same time.

To detect the equilibria for the system CO_2 -acetone-water it was necessary to relate the two calibration curves reported above.

Figure IV.9 shows the validation experiments for the system CO_2 -acetone-water at $60^\circ C$ and 100 bar, also in this case the data obtained by Raman scattering were compared with those reported in literature (Wendland *et al.*, 1994).

Vapour liquid equilibria measurements

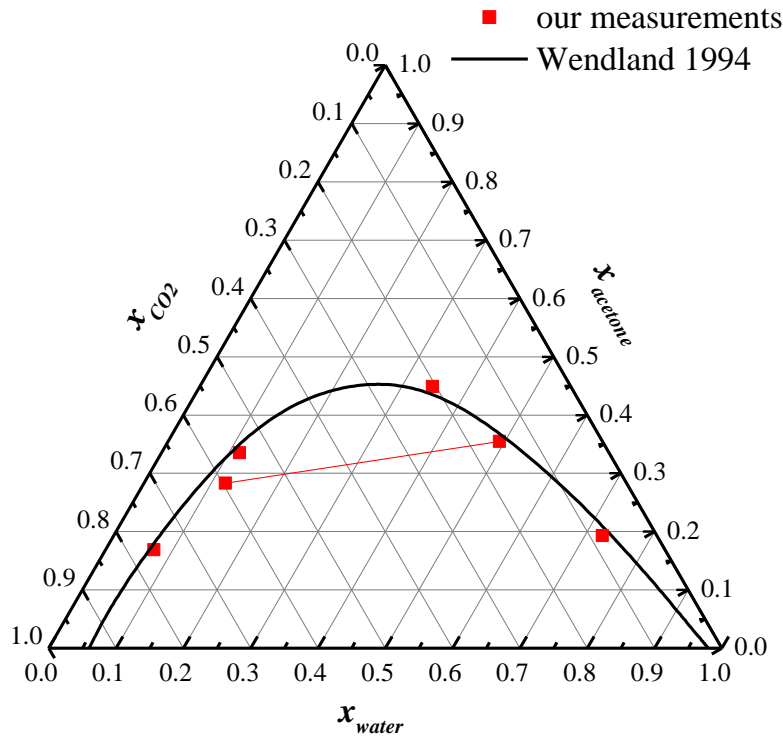


Figure IV.9 Comparison between the equilibria data obtained by Raman based technique and data reported in literature (Wendland et al., 1994) at 60°C and 100 bar

The data detected by Raman scattering are very similar to those reported in literature, therefore, it was demonstrated that Raman scattering is an efficient technique for equilibrium molar fraction detection.

On the basis of the validation experiments Raman scattering detection was also applied to the equilibria at 80°C and 90 bar for the system CO₂-acetone-water (see **Figure IV.10**). In this case no data related to these conditions are presented in literature, but the investigated conditions are the same used for SAA experiment on Polyvinylpirrolidone.

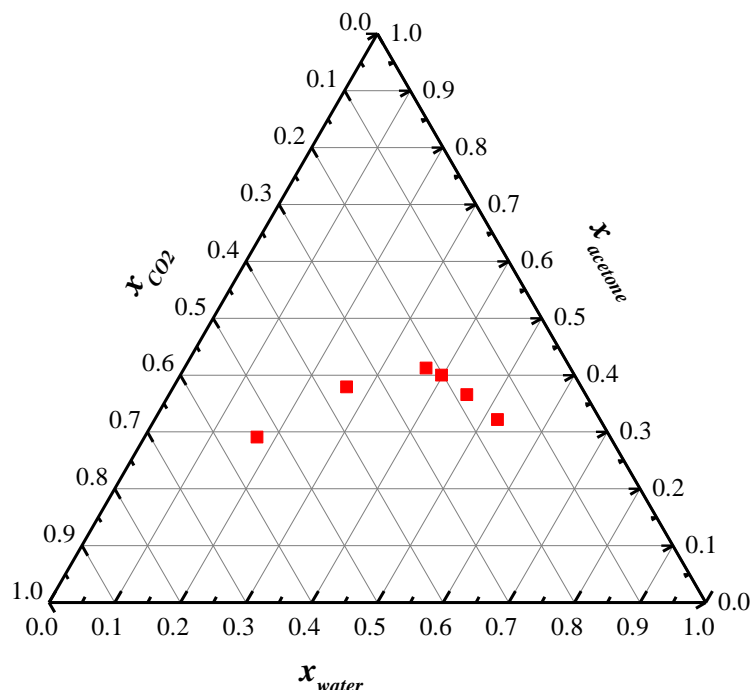


Figure IV.10 Molar fraction detection by Raman scattering at 80°C and 90 bar, for the system CO₂-acetone-water.

The two phase region obtained at 80°C and 90 bar is narrower than those obtained at 60°C and 100 bar. Generally speaking the two phase region becomes narrow when temperature increases, as observed by Wendland and coworkers that studied the same system from 40°C to 60°C (Wendland et al., 1994).

IV.8. Conclusions

Raman scattering based technique is an efficient method to detect the compositions at equilibrium, since it has not any influence on the behavior of the system at equilibrium.

The noninvasive method was validated for binary and ternary systems, obtaining very similar results compared with data reported in literature.

The application of Raman can be extended to the evaluation of molar composition at equilibrium for the system acetone-water-CO₂ at 80°C and 90 bar and, as expected, the two phase region became narrower than those obtained at lower temperature.

Vapour liquid equilibria measurements

The technique can be used for VLE measurements of several mixtures in which high pressure CO₂ is involved

Chapter IV

Chapter V

Experimental study on atomization mechanism

The particle size distribution in SAA process is strongly affected by the droplet size distribution at the exit from the injector. Many research works focused on the study of the effect of operative conditions of spray based processes, such as the amount of gas, pressure, temperature and the kind of nozzle, on droplet size distribution using laser diffraction technique (Mugele and Evans, 1951, Sovani et al., 2005, Dumouchel et al., 2009, Caputo et al., 2010, Li et al., 2011, Caputo et al., 2012, Gülder, 1990).

Laser diffraction (LD) technique is an optical diagnostic method used to measure drop (in case of emulsions) and particle diameter distribution, it can be used also to measure the drop size distribution of liquid sprays.

LD technique allows to measure particle size distributions using the angular variation in intensity of light scattered as a laser beam passes through a dispersed particulate sample. Large particles scatter light at small angles relative to the laser beam and small particles scatter light at large angles, as illustrated in **Figure V.1**.

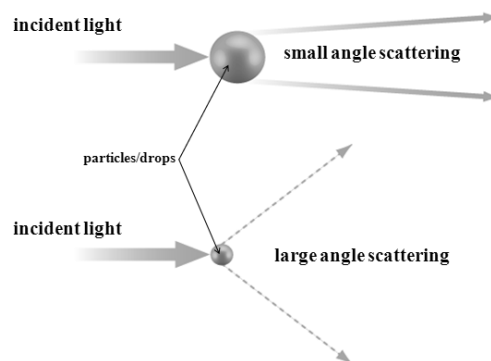


Figure V.1 Sketch of laser diffraction

Chapter V

The angular scattering intensity data is, then, analyzed to calculate the size of the particles responsible for creating the scattering pattern, using the Mie theory of light scattering². The particle size is reported as a volume equivalent sphere diameter.

Mie theory requires knowledge of the optical properties (refractive index and imaginary component). Usually the optical properties of the dispersant are relatively easy to find from published data, and many modern instruments have in-built databases that include common fluids. If the optical properties are not known, the user can either measure them or estimate them using an iterative approach based upon the goodness of fit between the modelled data and the actual data collected for the sample.

A simplified approach is to use the Fraunhofer approximation³, which does not require knowledge of the optical properties of the sample. This can provide accurate results for large particles. However it should be

used with caution whenever working with samples which might have particles below 50 μm or where the particles are relatively transparent.

V.1 Supercritical dissolved gas atomization

In order to have a better knowledge of the mechanisms involved in the formation of drops and particles one part of SAA process has been investigated: the mixing of the solution and SC-CO₂ in the saturator, and the subsequent jet break up. This part of the process has been defined supercritical dissolved gas atomization (SDGA). The system used is schematize in **Figure V.2**.

2

http://www.malvern.com/processeng/systems/laser_diffraction/technology/technology.htm

3

http://www.malvern.com/labeng/technology/laser_diffraction/mie_theory_fraunhofer.htm

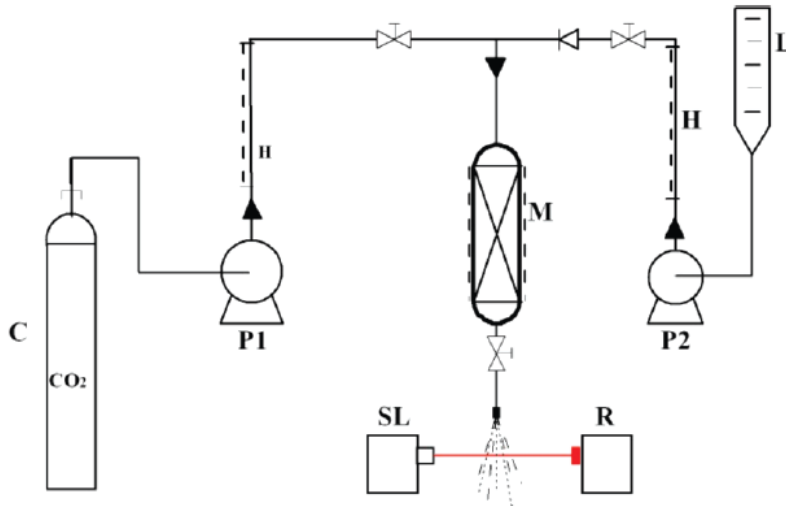


Figure V.2 Scheme of the system used to study the droplet size distribution. (C) CO₂ tank; (P1) CO₂ pump; (P2) liquid pump; (M) saturator; (L) liquid tank; (SL) laser source; (R) receiver.

In SDGA the CO₂ is dissolved in the liquid feed in a saturator, a packed vessel that assures a high liquid-gas contact surface, thus the solution is injected through the nozzle located at the bottom of the packed vessel. This configuration is close to the saturator used for supercritical assisted atomization, indeed the fluids have the same residence time of SAA process. The main difference concerns the surrounding in which the spray is released. Indeed, in SAA plant the spray is formed in a precipitator where it is possible to feed an inert gas and to adjust the temperature to enhance the evaporation of the solvent from the droplet. In SDGA the spray is not confined, therefore the coalescence of the droplet could take place. For this reason the measurement of the droplet size distribution have been performed at distance lower than 150 mm from the injector and a liquid droplet collector is located downstream the laser line. The effects of the gas-to-liquid mass ratio (mass of CO₂/mass of solvent; GLR) using two solvents, water and ethanol, nozzle diameter, and atomization temperature on the droplet mean size and size distribution have been studied.

V.1.1. Apparatus and methods

The SDGA apparatus is illustrated in **Figure V.2**. It mainly consists of two feed lines used to deliver the atomizing gas and the liquid to a mixing vessel. Atomizing gas stored in a vessel (C) is preheated in a water bath and delivered to the mixer (M) by a volumetric pump (P1). The liquid is

delivered to the mixer by a membrane pump (P2) from a 500 mL graduated cylinder (L). The two streams are fed to the mixer through a three-way connection. The mixer is a high-pressure vessel with an internal volume of 0.15 dm³ heated by thin band heaters and is packed with stainless steel perforated saddles with a high specific surface area. It provides a large contacting surface and an adequate residence time (3–5 min depending on the flow rates) for the mixing of the liquid and gas. Therefore, an efficient continuous solubilization of the gas in the liquid solution is ensured. As a result, the gas dissolves in the liquid and tends to form a fluid phase near the saturation limits at the chosen operating conditions of temperature and pressure. The pressure in the saturator is measured by a pressure gauge mounted on the top of the saturator. The mixture of solvent and CO₂ at the exit of the saturator is sprayed into the atmosphere using a single plain orifice. Two nozzles have been used: with a diameter of 120 μm and 80 μm with length to diameter (*l/D*) ratio of 6.67 and 8 respectively. The orifice dimensions were selected to obtain pressure above the critical pressure of CO₂ (7.38 MPa) at the given flow rates of gas inside the saturator.

The characteristics of the spray were investigated using the laser diffraction technique. A Mastersizer S (Malvern Instruments, Malvern, U.K.) particle size analyzer equipped with a 300 mm focal length lens was used to measure the spray droplet size distribution, this provides a lower droplet size boundary of about 0.5 μm. The technique is based on measurement of the scattered light intensity caused by the drops as they pass through the analyzer sampling area, using a series of semicircular photodiodes housed in the detector unit. The effect of the presence of the CO₂ on the refractive index of the gas phase was not considered because refractive index of surrounding ambient and CO₂ are considered the same. The instrument-reported obscuration was used to indicate the presence of multiple scattering due to dense spray. Instrument software compensates for multiple scattering and it works satisfactorily up to 95% obscuration. Droplet size measurements were carried out at distances of 5 and 135 mm downstream of the nozzle exit, with the laser beam passing through the centerline of the spray. The recirculation of droplets was kept to a minimum by absorbing the spray on an adsorbent material located about 40 cm downstream of the nozzle exit. Each experiment consisted of a set of five consecutive analyses, each composed of 10000 data points acquired by the analyzer. In the atomization literature, the Sauter Mean Diameter (SMD) is frequently used to represent the mean droplet diameter of a spray because it expresses the fineness of a spray in terms of the surface area produced by it. The SMD is defined as the volume-to-surface mean diameter.

The plain-orifice atomizer produces a coherent jet of liquid when pure liquid is injected. With the addition of SC-CO₂ or N₂, the jet disintegrates into a fine spray in which it is not possible to visually observe any phase separation between gas and liquid.

V.2. Results

All the experiments were performed at steady-state conditions with the injector spraying into the atmosphere. Steady-state conditions were determined when flow rates, pressure, and temperature, inside M, reached constant values. The spray characteristics reported here include the mean droplet size (SMD) and the droplet size distribution curves. Their variations with GLR, temperature, and injector downstream distance were studied. Experimental observations are presented as a function of GLR; indeed literature on effervescent atomization (Sovani et al., 2001) reports that this is the main parameter that affects the mean dimension of drops, therefore the same method was applied for SDGA experiments, since it usually operates in the two phase region of VLE.

Knowledge of the phase equilibrium is fundamental to understand the phenomena in the saturator because it provides information on the maximum quantity of gas that can be dissolved in the liquid. The composition of the liquid and gas phases can be determined from thermodynamic phase diagrams representing, as a pressure-mole fraction ($p-x$), the miscibility curve of the binary system gas solvent. **Figure V.3** and **Figure V.4** show vapour liquid equilibria (VLEs) for the systems CO₂-water and CO₂-ethanol (Bamberger et al., 2000).

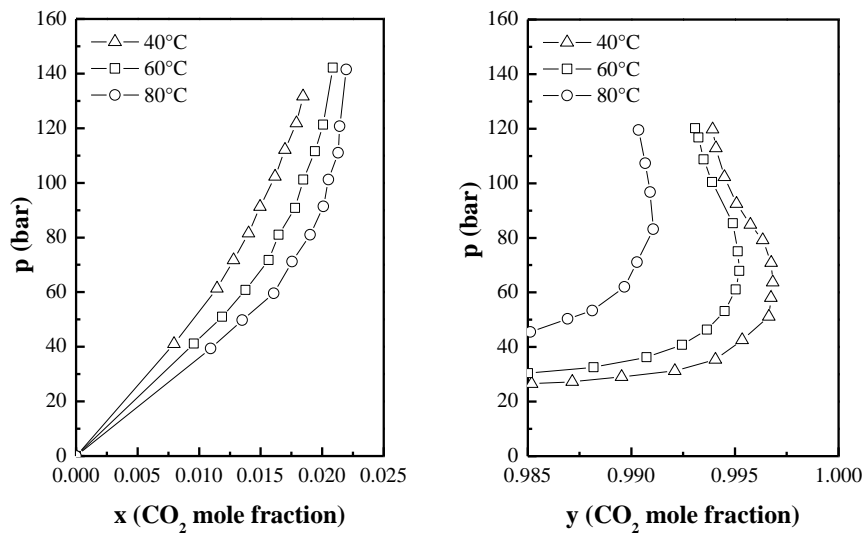


Figure V.3 Vapour liquid equilibria for the system water-CO₂. (Bamberger et al., 2000) at 40°C (Δ), 60°C (\square) and 80°C (\circ)

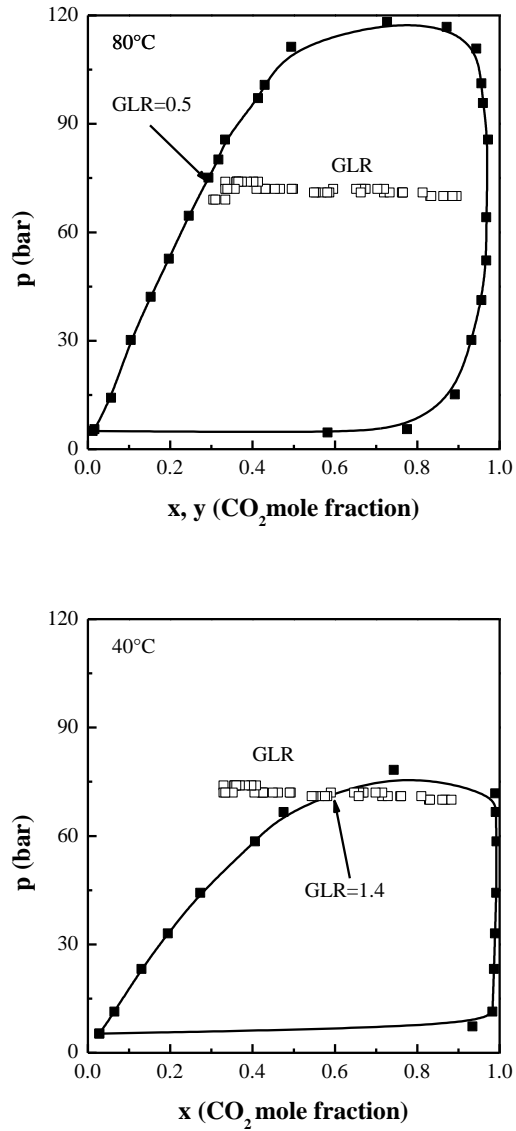


Figure V.4 VLE data (■) and operating points (□) of the system ethanol–CO₂ at 40°C and 80°C (Knez et al., 2008)

An operating point is characterized by the mole fraction of the mixture inside the saturator and the saturator pressure. Mole fraction (x_{CO_2}) and GLR are directly correlated by the relationship in Equation 12

$$x_{CO_2} = \frac{GLR(MW_{solvent} / MW_{CO_2})}{GLR(MW_{solvent} / MW_{CO_2}) + 1} \quad (13)$$

MW : molecular weight

Figure V.3 shows that the amount of CO₂ that solubilizes in water is very low, therefore it is not possible to operate in the one-phase region. Whereas CO₂ shows a good solubility in ethanol, therefore, using this solvent it is possible to operate in the one-phase region in the saturator. In the hypothesis that equilibrium conditions hold in the saturator, the system changes from one-phase to two-phase flow as GLR increases. At 40°C and 70 bar, the operative point moves from the one phase region to the two phase region when $x = 0.57$ (crossover); this molar fraction corresponds to $GLR = 1.14$; at 80°C, the crossover occurs at about $x = 0.3$ and $GLR = 0.5$. With the aid of these diagrams, we can study the effect of the phase transition on the droplet size, and moreover, we can study the role played by the dissolved gas on the atomization.

V.2.1 Atomization of ethanol and water using CO₂

Generally, the results show that SMD is a nonlinear function of GLR: drop size decreases rapidly as GLR is increased to around 2–3; then, it decreases at a lower rate, increasing in GLR.

The operative conditions used for the experiments are:

- 120 μm injector diameter;
- 13 gr/min CO₂ flow rate;
- 80°C;
- 70-90 bar;
- 135 mm axial distance from the injector

Pressure and temperature are the same used for SAA experiments using water as solvent (Della Porta et al., 2010). The results are summarizing in **Figure V.5**

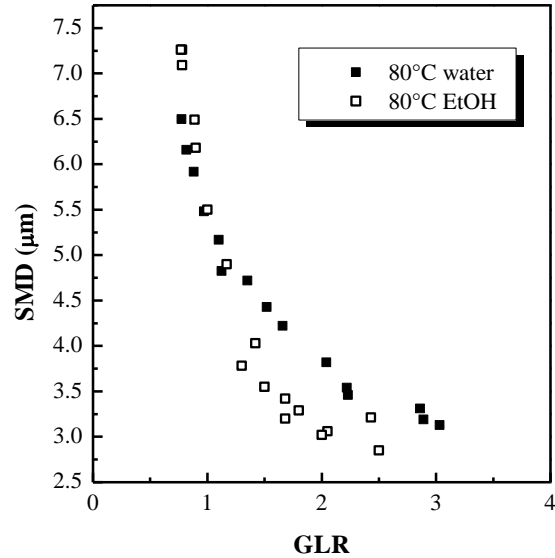


Figure V.5 Influence of GLR on the SMD of the droplets measured using different solvents. CO_2 flow rate=13 gr/min; N_2 flow rate=9 gr/min; Temperature=80°C; Pressure=70-90 bar; axial distance from the injector=135 mm; injector diameter=120 μm .

When the GLR is lower than 1.3, no relevant differences are noticed in the droplet size distribution, whereas, at higher value of GLR, the droplets obtained using ethanol as solvent have lower SMD than the droplets obtained using water as solvent. We could hypothesize that at lower value of GLR the phenomenon controlling the atomization process concerns the energy carried by the atomizing gas. This energy, accordingly with the hypothesis of Sovani et al. (Sovani et al., 2005), is larger than the one required for atomization, thus the gas energy is sufficient to obtain fine atomization also with a liquid of higher viscosity and surface tension.

Figure V.6 shows the behavior of the system CO_2 -ethanol at different temperatures of the saturator. The drop size distribution was measured at 135 mm and 7 mm from the injector.

Experimental study on atomization mechanism

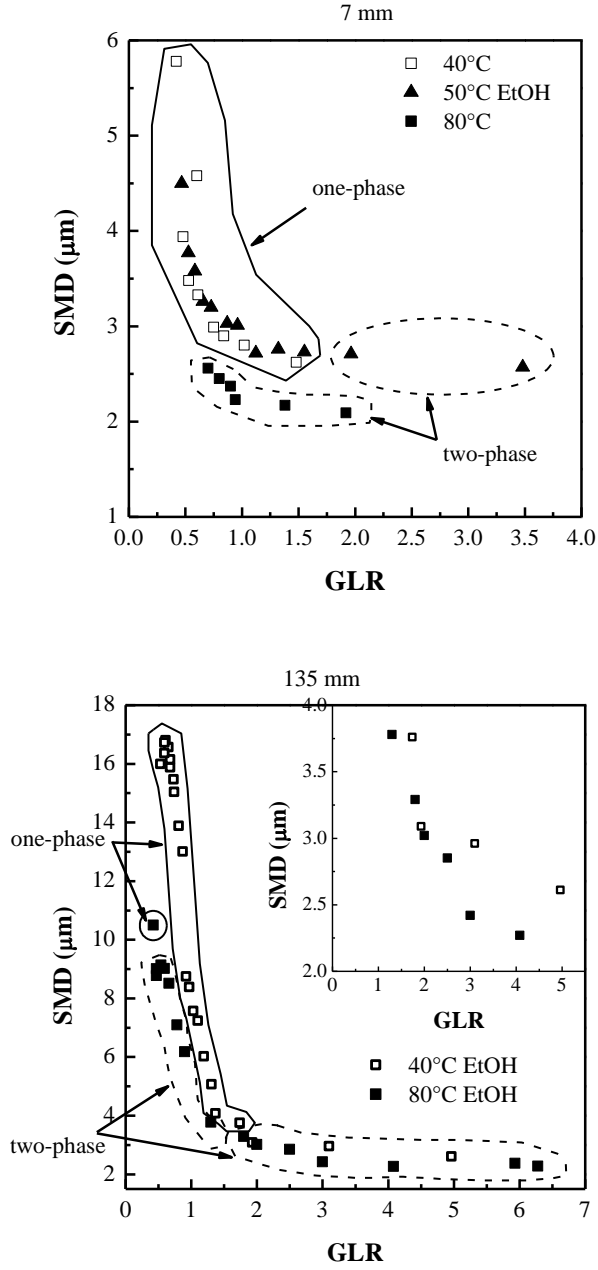


Figure V.6 Influence of GLR on the SMD of the droplets at different temperatures. CO_2 flow rate=16 gr/min, injector diameter=120 μm, and axial distance=135 mm and 7 mm.

Chapter V

At a distance of 7 mm from the nozzle, smaller drops can be obtained operating at higher temperatures (80°C) independently from the phases formed in the saturator. At 135 mm from the nozzle bigger drops were obtained at lower temperatures (40°C) operating in the one phase region, whereas only a small difference in drop diameter could be detected when the system is in the two phase region. Generally speaking, the increase of temperature induces a decrease of solution viscosity and surface tension (Sovani et al., 2001), therefore, at higher temperatures smaller drops can be obtained. However, at higher axial distances from the nozzle, evaporation of smaller drops could take place, and the difference in drop diameter is visible only for low values of GLR, that correspond to a low value of gas flow rate and to a less efficient jet break-up. **Figure V.7** confirms this statement.

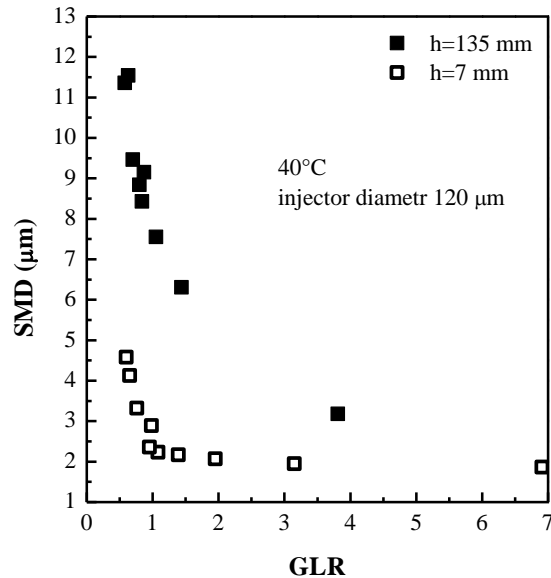


Figure V.7 Influence of GLR on the SMD of the droplets measured at different distances (h) from the injector. CO_2 flow rate = 16 gr/min and injector diameter = 120 μ m.

The SMDs registered at 135 mm from the injector are considerably bigger than those registered at 7 mm.

The behavior of the system CO_2 -ethanol at different CO_2 flow rate was also taken into account. The results are summarized in **Figure V.8**.

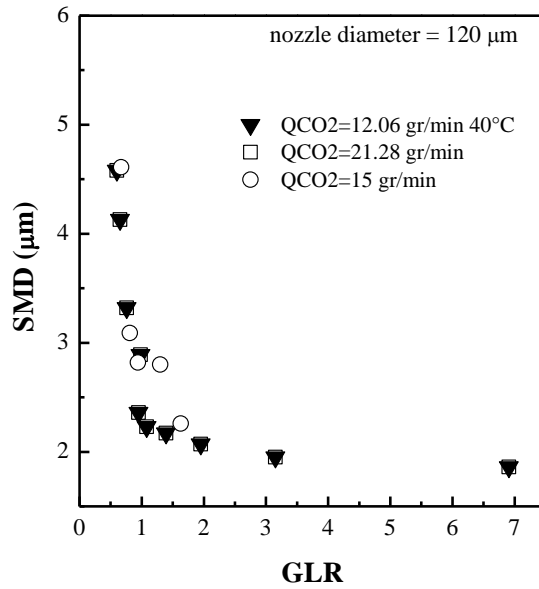


Figure V.8 Influence of GLR on the SMD of the droplets measured at different CO₂ flow rate. Temperature=80°C; Pressure=70-90 bar; axial distance from the injector=7 mm; nozzle diameter=120 μm .

The flow rate of CO₂ has not an remarkable influence on droplet size distribution. This behavior was registered also for the system CO₂-water (Caputo et al., 2010).

The last investigated parameter was the influence of the nozzle diameter; two injector diameter were used, 80 and 120 μm . The effect of the injector diameter is reported in **Figure V.9**.

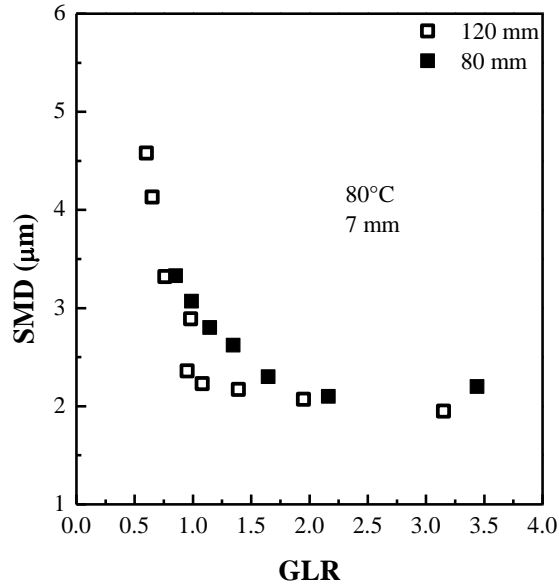


Figure V.9 Influence of GLR on the SMD of the droplets measured at different nozzle diameters. Temperature=80°C; Pressure=70-90 bar; axial distance from the injector=7 mm.

The SMD slightly decreases with an increase in nozzle diameter from 80 to 120 μm . However, the effect of the orifice diameter on the SMD is limited to some extent by the fact that the injection pressure slightly decreased when the orifice diameter was increased, because the experiments were performed at constant flow rates. This phenomenon was observed also in the case of effervescent atomization: Wade et al. (Wade et al., 1999) measured the droplet sizes produced by an effervescent atomizer at a very high injection pressure (33 MPa) for relatively small orifice diameters (180-340 μm) and noted that the mean droplet size decreased slightly as the diameter of the discharge orifice was increased. In this case when the injector diameter is reduced from 120 to 80 μm the length/diameter ratio (l/D) increases from 6.67 to 8, and smaller droplets were obtained.

V.3 Mechanism of atomization

The phenomenon that occurs in the SAA saturator, when two phases are formed, can be compared with flash atomization (Caputo et al., 2012, Park and Lee, 1994). In this conditions, it can be hypothesized that gas supersaturation takes place and segregation of gas induces bubbles

formation. When a pressurized liquid is driven out through an orifice, the pressure of the saturator abruptly decreases and the bubbles undergo a rapid expansion process, which results in a rapid disintegration of the liquid bulk into small droplets. Flash atomization can also be achieved by dissolving a flashing liquid (or liquid propellant) in the liquid to be atomized.

Essentially, flash atomization is initiated by in situ bubble nucleation followed by bubble growth that drives the atomization process. Basically, two flashing modes have been reported on the basis of the spray configuration outside the nozzle; they are the complete flashing mode (also called external flashing mode) and the two-phase effluent flashing mode (also called internal flashing mode) (Xiao et al., 2009). In the external flashing mode, the phase change with bubble formation occurs outside the nozzle, and it is characteristic of a short-hole nozzle (low l/D). In the internal flashing mode, the two-phase flow is already formed inside the nozzle, and it occurs mostly with a long-hole nozzle and particularly when $l/D > 7.15$. Indeed, more active bubble formation occurs with a longer nozzle due to a larger number of wall nucleation sites.

In our case l/D is 6.7 when the nozzle diameter is 120 μm and 8 when the nozzle diameter is 80 μm . Moreover, we operate at high value of GLR ($\text{GLR} < \text{GLR}_{\text{saturation}}$), higher than 2, and two phases are present in the nozzle, this allow the internal flashing mode. In this condition Sovani et al. (Sovani et al., 2001) summarized the studies on 3 possible different mechanisms of atomization:

- Bubbly flow,
- Slug flow
- Annular flow

as schematically reported in **Figure V.10**:

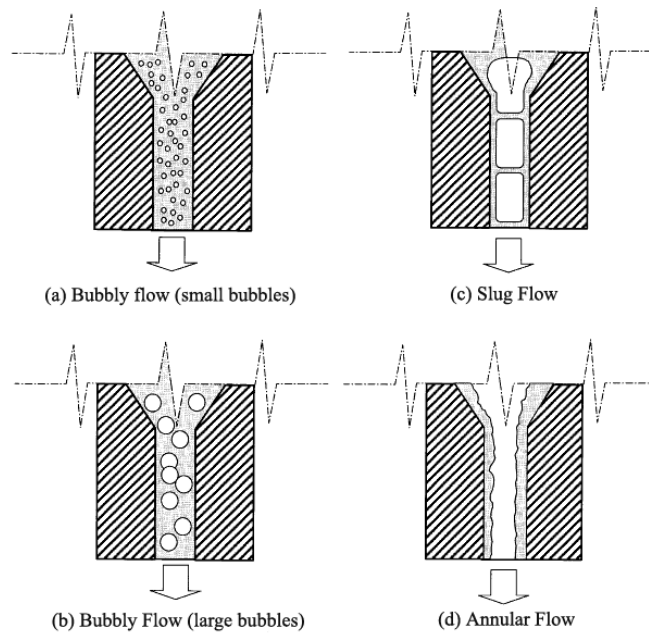


Figure V.10 Sketch of possible flow regimes in the discharge nozzle (Sovani *et al.*, 2001).

With bubbly flow, the bubbles discharged from the nozzle are dispersed in the liquid jet. On leaving the nozzle the bubbles experience a sudden pressure relaxation and rapidly expand, thereby shattering the liquid into drops. When the atomizer is operating in the slug flow regime, the rapidly expanding gas slugs similarly break up the liquid. In the annular flow the liquid forms an annular sheath within the ligaments due to the rapidly expanding gas core; the ligaments break up forming fragments that stabilize into drops. Since the liquid occupies only a small portion of the injector cross-section, the diameter of each ligament, and hence the size of drops formed, is considerably smaller than the diameter of the nozzle.

To understand the possible atomization regime of SDGA it is important to note how the cone angle change according to the increase of GLR, as shown in **Figure V.11**:

Experimental study on atomization mechanism

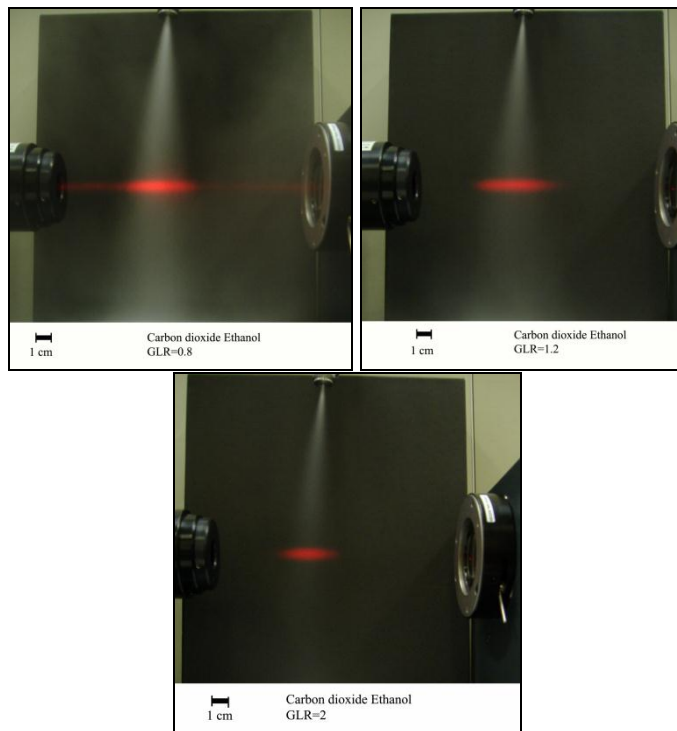


Figure V.11 Changing in cone angle due to the increase of GLR. ($T=40^{\circ}\text{C}$; $p=70$ bar; nozzle diameter $120\ \mu\text{m}$)

The spray cone angle decreases at higher value of GLR. According to Chen and Lefebvre (Chen and Lefebvre, 1994), this reduction in cone angle is due to the reduction in impact of bubbles on jet break-up which occurs when continuous increase in GLR causes the internal flow structure to change gradually from the bubbly to the annular flow regime. Therefore, it can be hypothesized that the regime of atomization is bubbly for low value of $\text{GLR}<1$ and becomes annular for higher GLR. This is because also the amount of dissolved gas induces the nucleation of bubbles in the inner zone of the injector. Moreover, when $\text{GLR}>1.5$ the SMDs are considerably smaller (see **Figure V.6**) than the diameter of the nozzle (2 order of magnitude), accordingly to the hypothesis of annular flow (Sovani et al., 2001)

V.4. Conclusions

The atomization strongly depends on the gas to liquid ratio. Drop size decreases rapidly as GLR value is increased to around 2–3, and at higher GLR, the drop size became insensitive to further increases in GLR.

Chapter V

At low value of GLR the flow regime inside the nozzle is bubbly whereas at higher value of GLR the flow became annular.

Finally we can summarize the role of CO₂ as following:

- The dissolved gas decreases surface tension that is one of the most important parameter involved in the formation of fine drops;
- The undissolved gas enhances the atomization process allowing the formation of discontinuity regions (bubbles or annular) that reduce the section for the passage of the liquid and rapidly expands inducing the breakup of the liquid ligaments.

The hypothesis mentioned above are formulated taking into account the results obtained on SDGA. It could be reasonable apply the same hypothesis to SAA process because the inert gas flow and temperature set in the precipitator have no influence inside the nozzle, however these two parameters affect the spray shape, removing the solvent from the droplet and avoiding the condensation phenomenon, with the result of dried spherical particles.

Furthermore, the size of the particles might be smaller to the one of the starting droplets due to the shrinking effect related to evaporation under N₂ flow.

Chapter VI

Effect of the solvent on particle size

Laser diffraction experiments, performed to obtain the size distribution of the droplets at the exit of the injector, demonstrated that the solubilization of CO₂ allows the reduction of cohesive forces to obtain smaller drops than the one obtained using traditional processes. This effect is marked when organic solvents are used, since CO₂ is very soluble in these solvents. To verify the effect of CO₂ solubilization we performed experiments using different kind of solvents.

For this purpose Polyvinylpyrrolidone (PVP), an amphiphilic polymer used as carrier to enhance the dissolution rate of hydrophobic compounds (Kanaze et al., 2010), was selected as model compound. PVP is also used to suppress re-crystallization (Crowley and Zograf, 2003) of active molecules, as coating agent for iron oxide nanoparticles, to produce MRI contrast agents (Lee et al., 2008). Moreover, it was found that PVP increases the activity of some active molecules, such as anticancer drugs (Kamada et al., 2000).

In this work, the micronization of PVP is proposed to study the influence of SAA operative conditions on morphology and particle size. PVP was chosen for its solubility in different kind of solvents, that have different behavior with SC-CO₂, therefore it is possible to understand the role of SC-CO₂ in particle production. The solvents selected were: water, a mixture of water and acetone and ethanol. In each case the vapor-liquid equilibria for the systems CO₂-solvent were taken into account.

VI.1 Material and methods

CO₂ (99.9%, SON, Naples, Italy), nitrogen (N₂, 99.9%, SOL, Milan, Italy), acetone (99.5%, Panreac, Barcelona, Spain), ethanol (99.5%, Aldrich Chemical Co, Milan, Italy), polyvinylpyrrolidone (PVP, Mw:10000, Aldrich Chemical Co, Milan, Italy) were used as received.

Chapter VI

The morphology of PVP particles was observed by a field emission-scanning electron microscope (FESEM, mod. LEO 1525, Carl Zeiss SMT AG, Oberkochen, Germany).

Particle size (PS) and particle size distribution (PSD) were measured by dynamic laser scattering (DLS) using a Nanosizer (NanoZS Malvern Instrument, UK) equipped with a He-Ne laser operating at 5.0 mW and 633 nm, that measures the hydrodynamic diameter of the particles. PVP microparticles were dispersed in ethyl acetate. DLS analysis was performed setting temperature at 25°C.

Solid state analysis of the precipitates was performed using an X-ray powder diffractometer (model D8 Advance; Bruker AXS, Madison, WI) with a Cu sealed tube source. The measuring conditions were: Ni-filtered Cu K α radiation, λ 1.54 Å, 2θ angle ranging from 2 to 50 with a scan rate of 1 s/step and a step size of 0.05.

VI.2 Effect of solvents

Different kind of solvents, that have different behaviour with SC-CO₂, were selected: water, in which CO₂ shows a low solubility, mixture of water and acetone, where acetone is a non-solvent for the polymer but enhances the solubility of CO₂ in the system; ethanol, in which CO₂ shows a good solubility.

All the experiments were performed setting a temperature of 100°C and a pressure of 1.8 bar in the precipitator, 85°C in the saturator and a GLR (ratio CO₂/liquid w/w) of 1.8. Different concentrations of solute in the liquid feed were used: 20, 40 and 80 mg/mL.

Water

Table VI.1 summarizes the operative conditions used for SAA experiments:

Table VI.1 Selected SAA experiments on PVP microparticles production using water as solvent. The nitrogen flow rate is 1380 NL/hr. (*c*: solute concentration; *Q*_{CO₂}: CO₂ flow rate; *T*_p: precipitation temperature; *p*_p: precipitation pressure; *T*_m: saturator temperature; *p*_m: saturator pressure)

n. test	solvent	c	GLR	Q _{CO₂}	T _p	p _p	T _m	p _m	D ₅₀
		mg/mL	w _{CO₂} /w _{liq}	g/min	°C	bar	°C	bar	μm
PVP_p04		20	1.8	8.43	102	1.7	85	115	1.20
PVP_p05	H ₂ O	40	1.8	8.43	102	1.8	84	115	1.46
PVP_p06		80	1.8	8.43	101	1.8	84	115	1.86

Effect of the solvent on particle size

When water is used as liquid solvent, a limited amount of CO₂ can be solubilized in the liquid solution, since the mutual solubility of the two compounds is very low at the usual SAA process conditions (Reverchon and Antonacci, 2006b). An heterogeneous mixture is formed in the saturator. The main effect of CO₂ is the pneumatic one, indeed, CO₂ supplementing nozzle pressure difference and improving the atomization (Caputo et al., 2010).

The experiments were performed at different concentration of solute. **Figure VI.1** reports SEM photomicrographs of the obtained microparticles.

Chapter VI

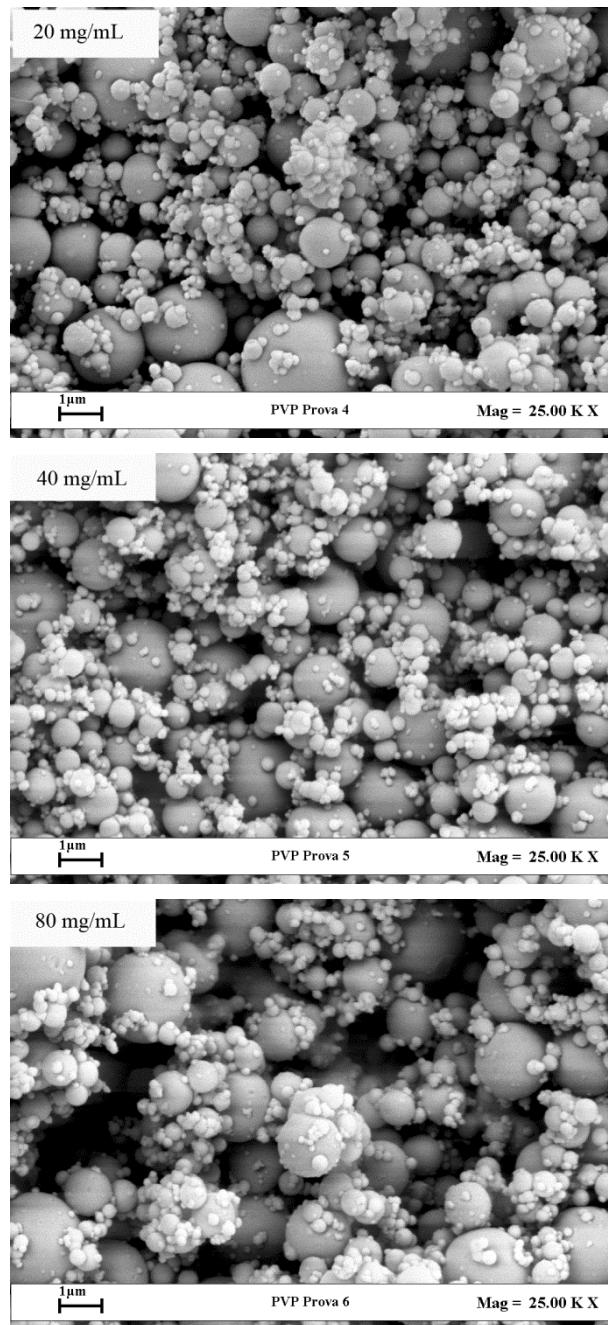


Figure VI.1 PVP microparticles obtained by SAA using water as solvent at different concentration of solute. (a) 20 mg/mL; (b) 40 mg/mL; (c) 80mg/mL.

Spherical particles were obtained and, as expected, the particle size decreases as the concentration of solute decreases (Adami et al., 2009), as

reported in **Table VI.1**. This effect is due to the increase of viscosity during the formation of particles (Braeuer et al., 2011).

Mixture water-acetone

Acetone is a non-solvent for PVP, but has a large affinity for SC-CO₂; therefore, its presence allows the solubilization of a larger quantities of CO₂ in the liquid solution. When SC-CO₂ is added to the system and the mixing takes place in the saturator, ternary system water-CO₂-acetone should be considered. In every case the amount of PVP in the system is low and its contribution to phase equilibria can be neglected (Adami et al., 2011). **Figure VI.2** reports VLE for the system CO₂-acetone-water. This VLE is referred to the water-CO₂-acetone equilibria at 90 bar and 80°C.

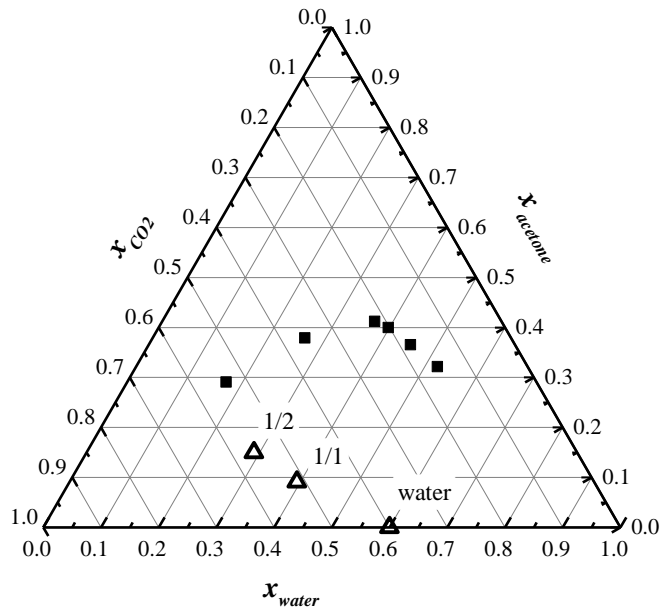


Figure VI.2 Vapor liquid equilibria for the system water-CO₂-acetone at 90 bar and 80°C detected by Raman based technology (see chapter IV). The operative points are indicated with the ratio water/acetone used, the GLR is 1.8 and is referred to the ratio between CO₂ and liquid (water + acetone) flow rate (w/w).

The GLR (1.8) is referred to the ratio between CO₂ and liquid (water + acetone) flow rates (w/w). Therefore, the formation of a two-phase mixture takes place. In this case the phase rich in water shows a lower viscosity and

Chapter VI

surface tension with respect to the previous series of experiments, due to the presence of a higher amount of CO₂ solubilized..

Table VI.2 Selected SAA experiments on PVP microparticles production using water-acetone mixture as solvent. The nitrogen flow rate is 1380 NL/hr. (c: solute concentration; Q_{CO2}: CO₂ flow rate; T_p: precipitation temperature; p_p: precipitation pressure; T_m: saturator temperature; p_m: saturator pressure)

n. test	solvent	c	GLR	Q _{CO2}	T _p	p _p	T _m	p _m	D ₅₀
		mg/mL	w _{CO2} /w _{liq}	g/min	°C	bar	°C	bar	µm
PVP_p01		20	1.8	7.58	103	1.7	85	110	0.91
PVP_p02	H ₂ O/Ac 1/1	40	1.8	7.58	101	1.7	84	110	1.43
PVP_p03		80	1.8	7.58	101	1.7	84	110	1.64
PVP_p07		20	1.8	7.24	99	1.7	85	103	1.17
PVP_p08	H ₂ O/Ac 1/2	40	1.8	7.24	101	1.7	85	103	1.72
PVP_p09		80	1.8	7.24	101	1.7	84	103	2.12

Figure VI.3 shows an example of PVP microparticles that can be obtained using the mixture water-acetone as liquid solvent: SEM photomicrographs related to different water/acetone ratio are shown.

Effect of the solvent on particle size

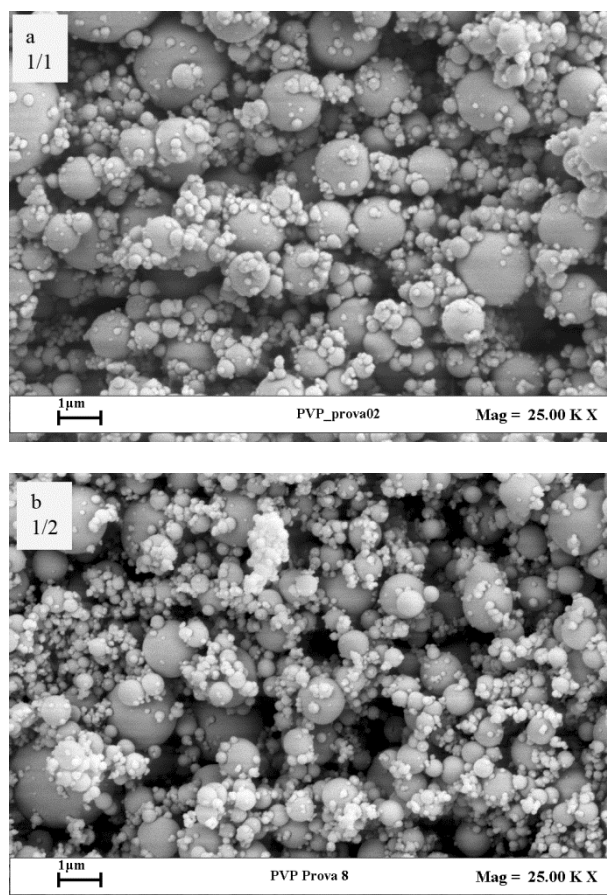


Figure VI.3 PVP microparticles obtained by SAA using water-acetone as solvent (a) 1/1(v/v); (b) 1/2 (v/v). Solute concentration 40 mg/mL.

Spherical particles were always obtained for all water/acetone ratios used, and no polymer residues were found in the saturator at the end of the experiment. This confirms the hypothesis, previously mentioned, on the effect of PVP on the phase equilibria, since no antisolvent effect takes place (Reverchon et al., 2008a).

The mean particle size is influenced by the solute concentration in a similar way than in the case of water as liquid feed, as shown in **Table VI.2**.

The smaller particles were obtained using 1/1 water/acetone ratio. When the mixture water-acetone is pressurized with CO₂, a phase split takes place: there will be a water rich phase, that contains all the PVP. In the solutions with a water/acetone ratio is 1/2 the amount of water rich phase is reduced, therefore the effective concentration of PVP in this phase is much higher than in the case of 1/1 water/acetone ratio. A higher amount of acetone in the

liquid feed does not induce the solubilization of a higher amount of CO₂ in the phase rich in water.

Ethanol

Ethanol has a large affinity with SC-CO₂, therefore, the quantity of CO₂ dissolved in the liquid phase can be maximize even when the operating conditions lie with the two-phase region of the VLEs. The vapor liquid equilibria for the system ethanol-CO₂ at different temperatures, are reported in **Figure VI.4**. This figure reports also the operative point related to the experimental conditions used in the performed test. Also in this case, and for the same reasons previously exposed, it can be hypothesized that solute has no influence or a negligible effect on VLEs.

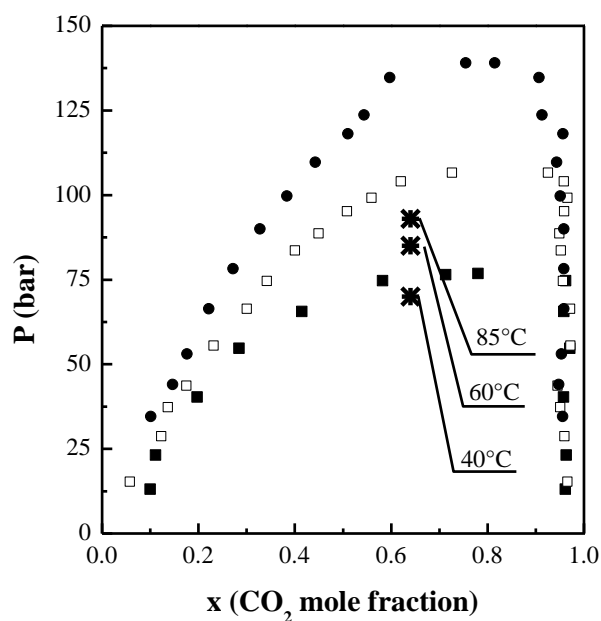


Figure VI.4 Vapor liquid equilibria for the system ethanol-CO₂ at different temperatures (■=40°C; □=60°C; ◆=80°C), adapted from Knez et al (Knez et al., 2008)

The feasibility tests demonstrated that PVP did not precipitate from the liquid phase in the saturator, therefore no antisolvent effect of SC-CO₂ with ethanol takes place at the tests operating conditions and CO₂/ethanol mole fraction used. When the saturator temperature is set at 85°C, two phases will be formed

Effect of the solvent on particle size

Setting the same conditions used for the experiments with water and the water/acetone mixtures (see **Table VI.2** and **Table VI.3**), spherical particles were again obtained, as shown in **Figure VI.5**.

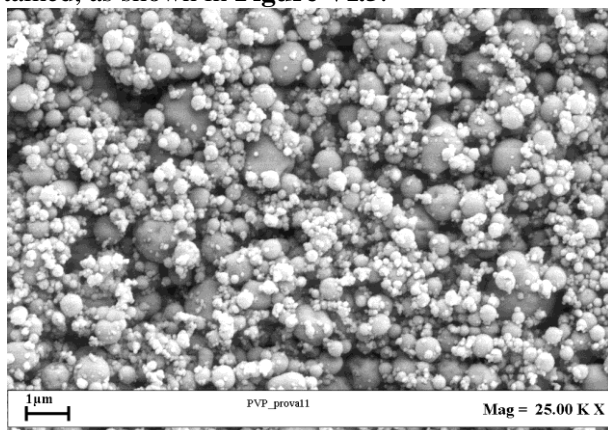


Figure VI.5 Microparticles obtained by SAA using ethanol and a concentration of PVP of 20 mg/mL.

Table VI.3 Selected SAA experiments on PVP microparticles production using ethanol as solvent. The nitrogen flow rate is 1380 NL/hr. (*c*: solute concentration; Q_{CO_2} : CO_2 flow rate; T_p : precipitation temperature; p_p : precipitation pressure; T_m : saturator temperature; p_m : saturator pressure)

n. test	solvent	c mg/mL	GLR w_{CO_2}/w_{liq}	Q_{CO_2} g/min	T_p °C	p_p bar	T_m °C	p_m bar	D_{nozzle} μm	D_{50} μm
PVP_p11		20	1.8	6.65	102	2	85	95	80	0.85
PVP_p10		20	1.8	6.65	85	1.8	86	95	80	0.96
PVP_p12		20	1.8	6.65	70	1.8	85	93	80	1.36
PVP_p13	EtOH	20	1.8	6.65	71	1.75	60	85	80	0.67
PVP_p16		20	1.8	6.65	71	1.8	41	70	80	0.73
PVP_p18		20	1.8	6.58	71	1.7	40	100	60	0.66
PVP_p19		20	1.8	6.54	70	1.5	40	165	40	0.47

However, DLS analysis (see **Table VI.3**) demonstrated that using ethanol, it is possible to obtain smaller particles than those produced using the mixtures water/acetone, with a mean diameter of 0.85 (± 0.6) μm. This is probably due, again, to the increase of CO_2 dissolved in the liquid phase. Indeed, the experimental evidences from the previous set of experiments, demonstrated that the solubilization of CO_2 in the liquid feed is a key factor in enhancing the atomization process. To verify this statement, other experiments were performed changing the saturator temperature, operating

Chapter VI

in this manner, for this specific system variation the amount of CO₂ solubilized in the liquid phase is obtained. The operative points of these tests are reported in **Figure VI.4**.

Figure VI.6 reports photomicrographs of the particles obtained at different saturator temperatures.

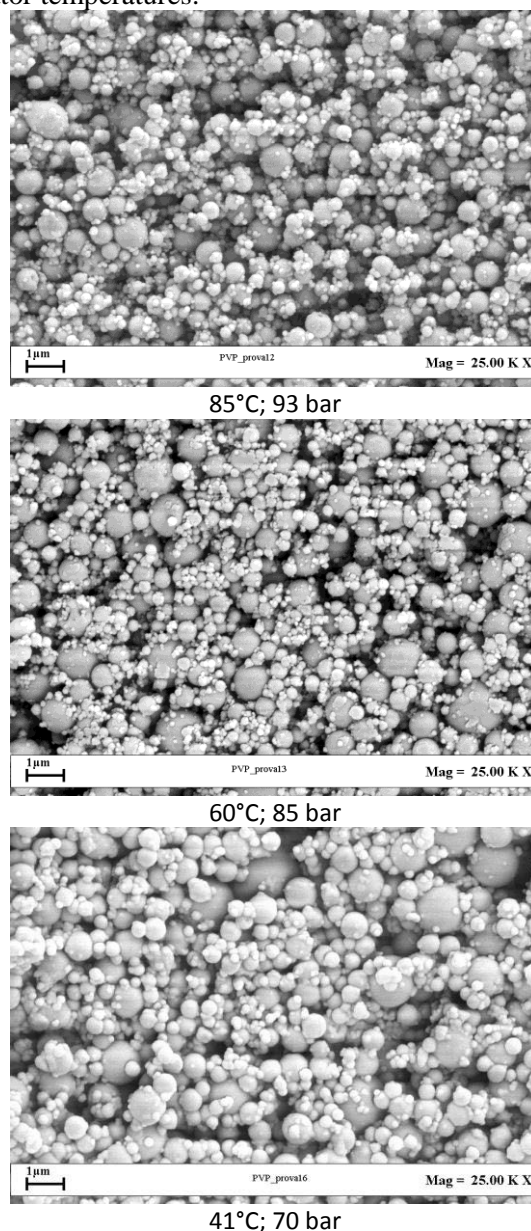
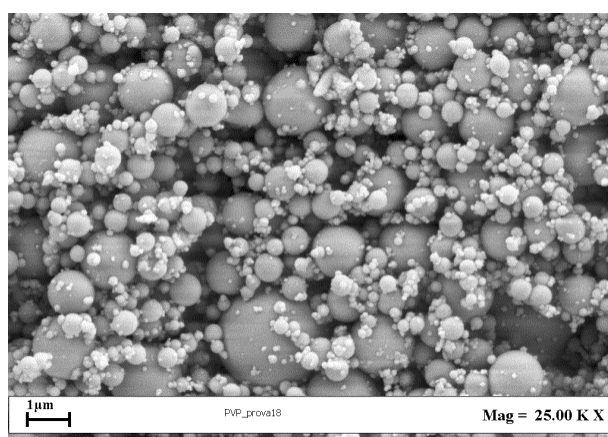


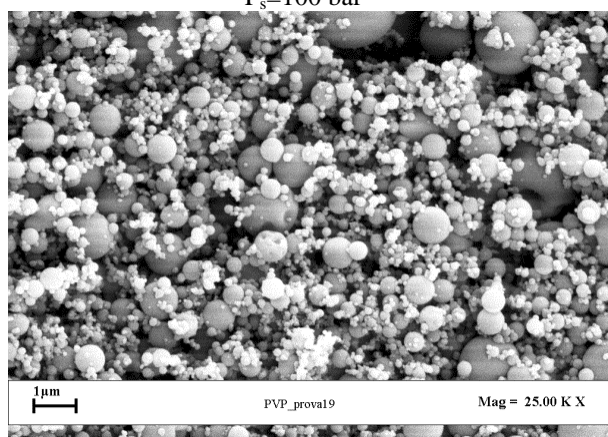
Figure VI.6 PVP microparticles obtained by SAA changing the saturator temperature. Ethanol was used as solvent and the concentration of solute was 20 mg/mL; GLR=1.8; $p=70-93$ bar (see **Table VI.3**).

Effect of the solvent on particle size

Figure VI.6 shows that the morphology of the particles is not influenced by the saturator temperature; whereas, particle size distributions (see **Table VI.3**) reveal that the increase of CO₂ solubilized allows the formation of smaller particles, especially at lower temperatures (40°C). However, **Table VI.3** reports that a decrease of temperature leads the decrease of saturator pressure. To decouple these effects and to understand if the pressure has any influence on particle size, some tests were performed setting 40°C in the saturator and using nozzles with different diameter (80, 60 and 40 µm) that, fixed all the other process parameters, produce an increase of saturator pressure.



Nozzle diameter 60 µm
 $P_s=100$ bar



Nozzle diameter 40 µm
 $P_s=165$ bar

Figure VI.7 PVP microparticles obtained by SAA using different nozzle diameters. Ethanol was used as solvent and the concentration of solute was 20 mg/mL.

Chapter VI

The powder was analyzed by XRPD and DSC to understand how SAA process affects the solid state of the polymer. **Figure VI.8** shows the XRPD diagrams for the untreated and SAA processed polymer. Processed PVP has the same amorphous structure as the untreated material. This is confirmed by DSC analysis.

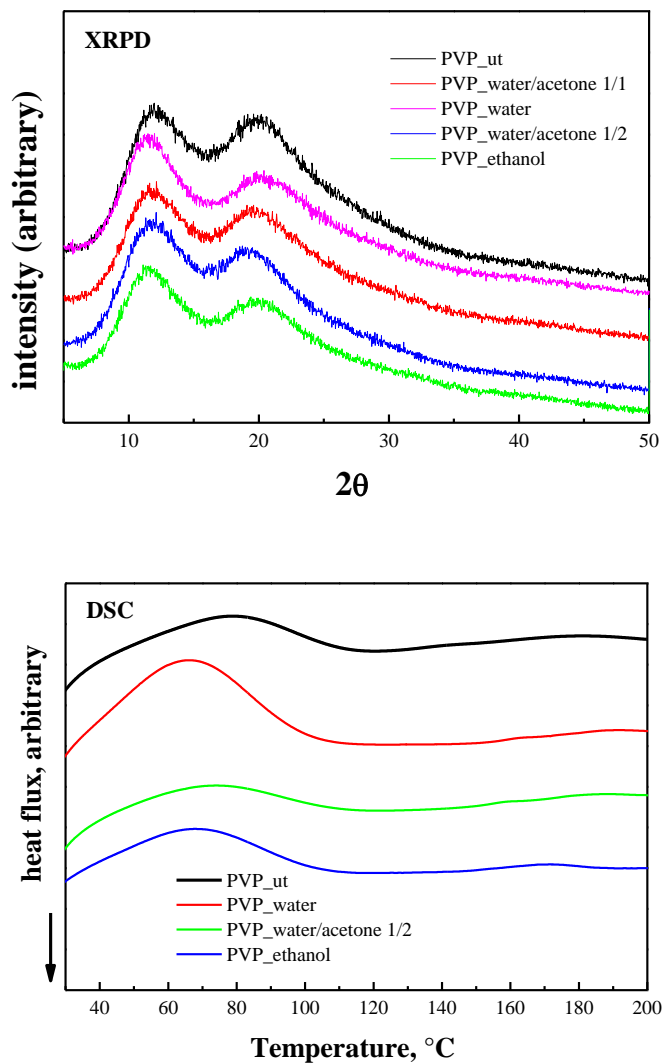


Figure VI.8 XRPD and DSC of PVP powder obtained by SAA compared with the untreated material.

shows that operating at 165 bar it is possible to obtain smaller particles. Therefore, at larger pressures, also the influence of this parameter cannot be neglected. However, CO_2 gives no contribution to a pneumatic effect in this

case, since, it is completely dissolved in the liquid. This fact could contribute to the demonstration that the main factor that influences the mean dimensions of the micro particles produced by SAA could be the amount of dissolved CO₂; indeed, when SC-CO₂ is completely solubilized in the liquid feed, smaller particles can be obtained. This experimental evidence confirms the key role of CO₂ in the atomization step, indeed its solubilization in the liquid feed allows to decrease the cohesive forces that have the most influence on particle size.

VI.3. Conclusions

The efficient micronization of PVP by SAA process clarifies the role of CO₂ was better understood: when a high amount of CO₂ can be solubilized in the liquid feed very small particles could be obtained. This results is summarized in **Table VI.4**:

Table VI.4 Mean diameter of PVP microparticles produced by SAA process, using different kind of solvents.

	<i>Dm</i> [μm]
<i>Water</i>	1.20 (± 0.25)
<i>Water/Acetone</i>	0.91 (± 0.30)
<i>Ethanol</i>	0.79 (± 0.30)

It is possible to produce sub-micrometric particles (0.50 μm diameter) operating in one phase region of VLSs, since in these conditions a significantly decrease of viscosity and surface tension takes place.

The geometry of nozzle is also important, since it affect the fluid velocity and the saturator pressure. The increasing in fluid velocity allows to operate at high Reynolds number whereas the increase of saturator pressure allows the reduction of cohesive forces; both these phenomena enhance the atomization process.

Chapter VI

Chapter VII

Choice of the operative conditions for the precipitation vessel.

VII.1 Drying mechanism

For quasi-steady heat transfer from the gas phase to the droplet surface the heat flux for the continuum regime is given by

$$q_{cont} = -\frac{k}{a}(T_{\infty} - T_s) \quad (14)$$

where k is the gas thermal conductivity, a is the droplet radius, T_s is the interfacial temperature, T_{∞} is the bulk temperature.

If the energy required for droplet evaporation is provided by heat conduction from the gas phase, the heat and mass fluxes are coupled because the vapor pressure is a strong function of the interfacial temperature, and the flux equations must satisfy the energy balance,

$$q = \lambda_{vap} j_i \quad (15)$$

in which λ_{vap} is the heat of vaporization.

The droplet mass change for a constant density droplet is related to the mass flux j_i of the evaporating species by

$$j_i = \frac{1}{4\pi a^2} \frac{dm}{dt} = -\rho \frac{da}{dt} \quad (16)$$

where m is the droplet mass, and ρ is its density.

$$\rho \frac{da}{dt} = \frac{k}{a\lambda_{evap}} (T_{\infty} - T_S) \quad (17)$$

This equation allows to evaluate the total lifetime of a drop.

Continuum theory is applicable when the mean free path, l , of the diffusing species is small compared to the droplet radius, that is, when the Knudsen number, Kn , is sufficiently small ($Kn \ll 1$) (2011). In SAA process Kn is lower than 1, as it will be discussed in following section.

However droplets contain solids, therefore they develop internal concentration gradient. For this reason the falling-rate period is usually matched by treating the drying problem as a diffusion problem, where the rate-limiting step is the diffusion of moisture from deep within the solid to the surface (Don Green, 2007).

VII.1.1. Nitrogen flow rate in the precipitator

Temperature control in the precipitator is necessary to allow a fast and complete evaporation of the solvent from the drops. To work at constant temperature in the precipitator an inert gas is fed to this vessel.

In this paragraph the nitrogen flow rate is evaluated on the bases of heat balance in the precipitator, without taking into account the mass transfer between the droplet and the inert gas, because nitrogen is continuously fed, therefore concentration gradient can be considered constant.

To evaluate the amount of nitrogen that is necessary we have to take into account the Joule Thompson effect that takes place when the solution passes through the injector. This effect is responsible for the decreasing of the temperature outside the injector. To evaluate the temperature at the exit from the nozzle we consider:

$$H_{IN} = H_{OUT} \quad (18)$$

Where H_{OUT} is the enthalpy outside the injector, whereas:

$$H_{IN} = H_{IN}^{ideal} + H_{IN}^{residue} \quad (19)$$

$$H_{IN}^{residue} = -RT^2 \int_{P=0}^P \left(\frac{\partial Z}{\partial T} \right)_P d \ln P \quad (20)$$

It is possible to evaluate temperature at the exit of the nozzle knowing temperature in the saturator.

The heat balance is necessary to evaluate the nitrogen flow rate.

Choise of the operative conditions for the precipitation vessel

$$Q_s = m_{solv} \cdot Cp_{solv} \cdot (T_\infty - T_{j-T}) + m_{CO2} \cdot Cp_{CO2} \cdot (T_\infty - T_{j-T}) \quad (21)$$

Heat necessary to increase temperature of the fluids from temperature due to Joule Thomson effect to precipitation temperature;

$$Q_{vap} = \lambda_{vap} m_{solv} \quad (22)$$

heat necessary for the evaporation of the solvent;

$$Q_{N2} = m_{N2} \cdot Cp_{N2} \cdot (T_{N2} - T_\infty) \quad (23)$$

heat due to nitrogen flow rate. There is, also, heat supplied by band heaters Q_h , that compensates the heat exchanged with surrounding ambient Q_{ex} .

$$Q_s + Q_{vap} + Q_{N2} + Q_h + Q_{ex} = 0 \quad (24)$$

From this balance it is possible to evaluate the flow rate of nitrogen, considering that T_{N2} , that is the inlet temperature for nitrogen, cannot be more than 20°C higher than T_∞ , to avoid the denaturation of the compound to micronize.

From this equation it can be deduced that if precipitation temperature decreases, because the compound cannot be processed at high temperature, the nitrogen flow has to be increased. Obviously, this flow cannot be increased up certain limits, because it induces non negligible increase of pressure inside the precipitator; moreover, in these conditions, condensation of solvent on the porous filter could take place. For this reason it is necessary to reduce the precipitation pressure.

VII.2 Study of precipitation at low temperature

Temperature necessary to allow the evaporation of the solvent changes with precipitation pressure. In order to reduce precipitation temperature to micronize thermolabile compounds we add a vacuum system downstream the precipitator.

VII.2.1 Choice of the vacuum system

The project of the vacuum system faces different problems:

Chapter VII

- Continuous nitrogen flow
- Evaporation of the solvent
- Presence of particles

Evaporation into a vacuum system is called outgassing. It can be defined as the release of gas during a phase transition (sublimation or evaporation). In a vacuum device, outgassing has the same effect as a leak and can limit the achievable vacuum. Outgassing products may condense on colder surfaces. The most common outgassing product in vacuum systems is water. Outgassed water can condense in the oil of rotary vane pumps and reduce their speed drastically if gas ballasting is not used. High vacuum systems must be clean and free of organic matter to minimize outgassing.

SAA process is a continuous process in which the outgassing products must be removed to avoid their condensation in the vacuum pump chamber. Moreover a considerable amount of inert gas continuously flow in the precipitator. These problems limit the choice of the pump.

The vacuum pumps can be classified as followed:

- Primary pumps: they operate at low vacuum in viscous regime.
- Secondary pumps: they operate at high vacuum and are placed in series with primary pumps. They operate at molecular flow regime.

It is necessary to determine the vacuum degree that has to be reached in the precipitation vessel. The vacuum degree depends on the temperature that is necessary for the solvent evaporation in the precipitator. The flow regime in the precipitator depends on the mean free path (L) of the molecules in the vessel.

Knudsen number (Kn) relates the mean free path to the equivalent diameter of the vessel:

$$Kn = \frac{L}{De} \quad (25)$$

De equivalent diameter

$$De = \frac{4S}{V} \quad (26)$$

L mean free path:

$$L = \frac{kT}{p\pi d^2 \sqrt{2}} \quad (27)$$

k Boltzmann's constant

T operating temperature

p pressure

d molecular diameter

The mean free path is the average distance covered by a molecule before successive impact. If the mean free path is smaller than the characteristic length of the vessel, or of the pipe, there will be a strong interaction between

Choice of the operative conditions for the precipitation vessel

the molecules so their flow is comparable to a viscous flow; only a low vacuum value can be obtained in the viscous regime, as shown from the

Table VII.1 *Vacuum rate*

<i>Vacuum range</i>	<i>Pressure [mbar]</i>	<i>Molecules / cm³</i>	<i>Molecules / m³</i>	<i>Mean free path</i>
<i>Ambient pressure</i>	1013	$2.7 \cdot 10^{19}$	$2.7 \cdot 10^{25}$	68 nm
<i>Low vacuum</i>	300-1	10^{19} - 10^{16}	10^{25} - 10^{22}	0.1-100 μ m
<i>Medium vacuum</i>	$1 \cdot 10^{-3}$	10^{16} - 10^{13}	10^{22} - 10^{19}	0.1-100 mm
<i>High vacuum</i>	10^{-3} - 10^{-7}	10^{13} - 10^9	10^{19} - 10^{15}	10 cm – 1 km
<i>Ultra high vacuum</i>	10^{-7} - 10^{-12}	10^9 - 10^4	10^{15} - 10^{10}	1 km – 10^5 km

When the flow is molecular (molecules do not interact, $Kn > 1$), the vacuum system has to be composed by a primary pump connected in series with a secondary pump; when the flow is viscous the $Kn \ll 1$, only primary pumps are necessary to get the required vacuum.

The Knudsen number for SAA process has been evaluated ($Kn \approx 10^{-5}$), and a viscous regime could be expected.

The primary pumps can be classified as following:

- Oil pumps;
- Oil free pumps.

The rotative oil pumps cannot be used in SAA process since the presence of particles reduces the efficiency of the pump. Moreover the condensable gases could form a corrosive emulsion. For these reasons it is much better to choose oil free pumps. This kind of pumps do not suffer of efficiency reduction in presence of condensable gasses or particles.

The oil free pumps can be classified as following:

- Scroll pumps
- Membrane pumps
- Piston pumps
- Rotative pumps

Scroll pump create vacuum using a simple dual scroll mechanism in which one of the nested scrolls orbits about the other, creating moving zones of captured gas. Gas enters the scroll set at the perimeter and is displaced

Chapter VII

and compressed toward the center hub where it is exhausted. **Figure VII.1** shows the mechanism of this kind of pumps. The vacuum degree that can be obtained with this pump is around 0.01 mbar, however the efficiency of the pump significantly decreases as vapour and chemical gasses pass through the vacuum chamber.

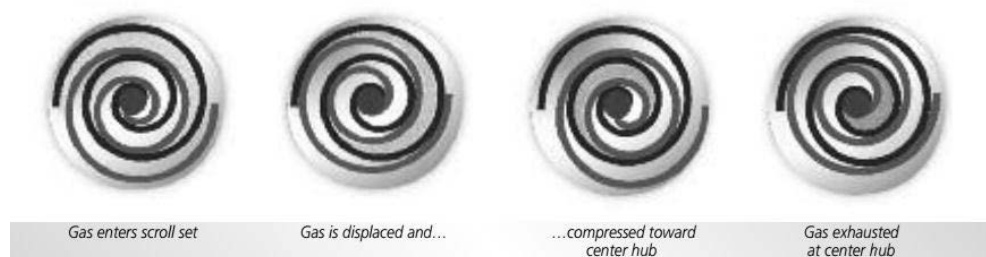


Figure VII.1 Scroll pump⁴

The membrane pump (**Figure VII.2**) is a positive displacement pump that uses a combination of the reciprocating action of a rubber, thermoplastic or teflon diaphragm and suitable non-return check valves to pump a fluid. Sometimes this kind of pump is also called membrane pump.

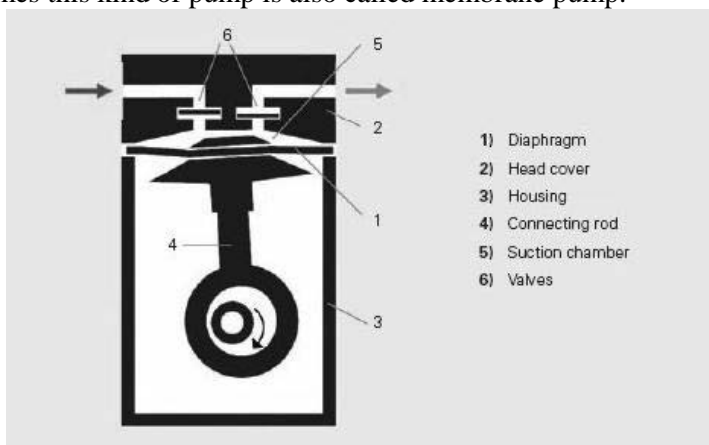


Figure VII.2 Membrane pump⁵

The vacuum degree that can be reached with this pump is around 1 mbar. The presence of condensable gasses does not induce the decrease of pump efficiency.

In the piston pump the piston oscillates between the upper position and the lower position. The direction of the movement is aligned with the direction of the connecting rod, therefore the component of the force is zero.

⁴ <http://www.chem.agilent.com>

⁵ <http://www.pfeiffer-vacuum.com>

Choice of the operative conditions for the precipitation vessel

The efficiency of this pump decreases very fast because the rot is scratched by the particles during the movement of the piston. Moreover, because this pump is oil free, it has to be made of some special material to avoid the disruption of the pump mechanical parts. The rate of vacuum that can be obtain is around 100 mbar.

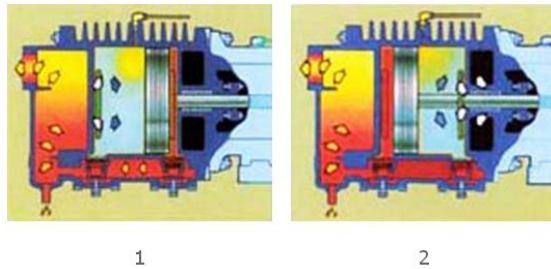


Figure VII.3 *Piston pump*⁶

A rotary vane pump is a positive-displacement pump that consists of vanes mounted to a rotor that rotates inside a cavity. The simplest vane pump is a circular rotor rotating inside a larger circular cavity. The centers of these two circles are offset, causing eccentricity. Vanes are allowed to slide into and out of the rotor and seal on all edges, creating vane chambers that do the pumping work. On the intake, the vane chambers are increasing in volume allowing to force the fluid inside the pump chamber. Often this inlet pressure is nothing more than pressure from the atmosphere. On the discharge side of the pump, the vane chambers decreases in volume, forcing fluid out of the pump. The action of the vane drives out the same volume of fluid with each rotation. Multistage rotary vane vacuum pumps can attain pressures as low as 3-10 mbar.

The oil free pumps have to be constructed using materials that do not need lubrication, as graphite. However, these material are sensitive to the presence of condensables.

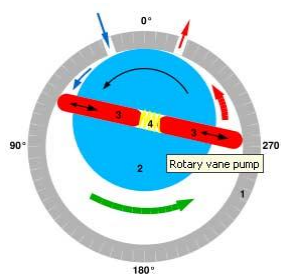


Figure VII.4 *Rotative pump*⁷.

⁶ <http://www.saurus.it>

Chapter VII

Oscillating piston pump with diaphragm can be chosen for SAA process, since the diaphragm isolates the mechanical parts of the pump avoiding the efficiency decrease in presence of particles and condensables.

The vacuum that can be obtained with oscillating piston pump is around 100 mbar

To choose the right pump, the volumetric rate S , the pumping speed and the lower pressure to be obtained have to be known. The pumping speed is a function of the inlet pressure and decreases when the work pressure decreases. In some situations the pumping speed decreases when the inlet pressure is too high, above the atmospheric pressure.

The mechanisms of vacuum pumps are comparable to the electrical circuits, therefore the electrical symbolism has to be used (Yoshimura, 2008).

The limit pressure is the lower pressure that the system reaches when there is not any gas feed. The final pressure can be different from the limit pressure. This pressure is function of conductance and gas flowrate:

$$Q = C(p_l - p_f) \quad (28)$$

Q gas flowrate
C conductance
 p_l limit pressure
 p_f final pressure

the pipe conductance can be calculated as followed:

$$C = \frac{DA^2T_0}{lT} \quad (29)$$

A transversal pipe area
l pipe length
T vessel temperature
 T_0 273 K

When the system operates in viscous regime the flow rate can be calculated as followed:

$$Q = \frac{\pi r_0^2 (p_1^2 - p_2^2)}{16\eta l} \quad (30)$$

r_0 pipe radius
 η viscosity

⁷ <http://www.emtivac.com.au>

Choice of the operative conditions for the precipitation vessel

To evaluate the pumping speed it is possible to use the same equation used for vacuum system of Freeze Drying, in which the evacuation time must be referred to the condensation.

$$S_{eff} = \left(\frac{2.3V}{T} * \frac{\log P_a}{P_{MD}} \right) + \left(\frac{3600S_w P_{RS}}{P_{SD}} \right) + \left(\frac{3600Q_L}{P_{SD}} \right) + \left(\frac{10^{-3}M}{t_{MD}} \right) \left[\frac{m^3}{h} \right] \quad (31)$$

- V volume of the system [m³]
- T evacuation time from the start pressure P_A to the condensation pressure [h];
- P_A start pressure [mbar];
- P_{MD} evaporation pressure [mbar];
- S_w lateral surface of the vessel [m²];
- P_{RS} vapor lived from the metallic surface [mbar L/s m²]
- M product [L]
- t_{MD} evaporation time [h]
- Q_L gas flowrate [mbar L/sec]

Using water as solvent the pumping speed in SAA process is evaluated around 60 L/min. For this reason oscillating piston pump with S=100 L/min is chosen; **Figure VII.5** shows vacuum pump scheme.

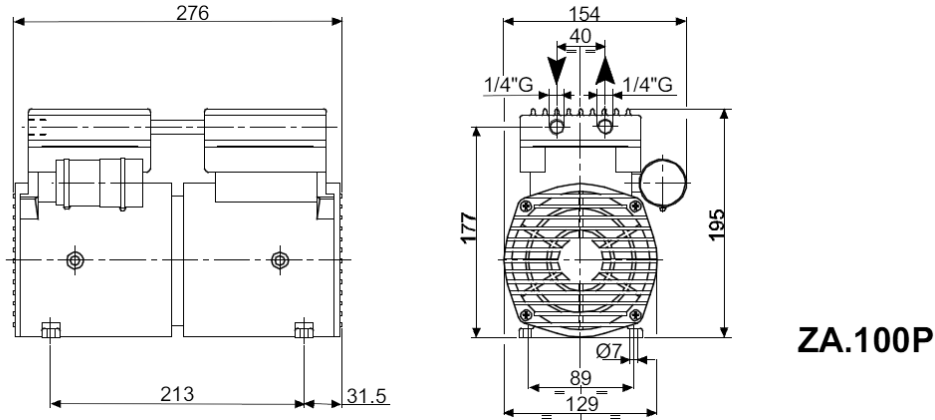


Figure VII.5 DVP pump⁸

The oscillating piston pump has an upper pumping speed of 100 L/min. **Figure VII.6** reports the flowrate versus vacuum rate of the commercial piston pumps (ZA.100P and ZA.60S DVP pump):

⁸ www.dvp.it

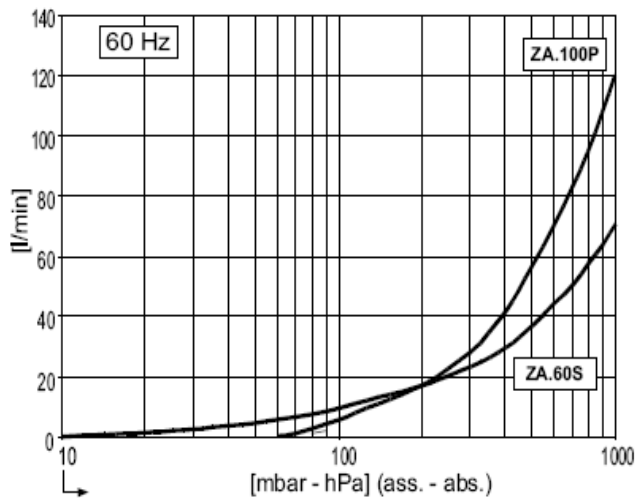
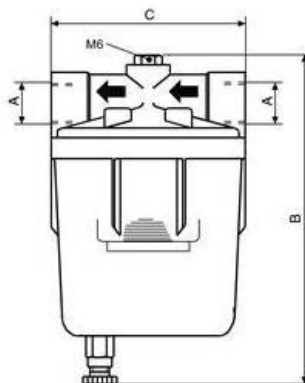


Figure VII.6 Vacuum rate scheme of DVP ZA-100P pump⁹

As previous discussed, the presence of condensable gases can be considered as a leak for the vacuum system. For this reason a condenser is introduced (see **Figure VII.7**)



Modello Modell Model Modelo	Codice Art-Nr. Code Código	Figura Figur Figure Figura	m ³ /h ⁽¹⁾	A	B	C
FSC.18R	9001013	A	18	3/8"G	135	80

Figure VII.7 Scheme of the condenser¹⁰

⁹ www.dvp.it

Choice of the operative conditions for the precipitation vessel

The condenser is cooled by a cold bath that operates at -10°C , the same bath that is used to cool the head of CO_2 pump.

Moreover, the capillary forces inside the porous filter increases the pressure drop in the precipitator. To overcome these limitations a parallel connection of two vacuum pumps is proposed.

The scheme of the plant in the configuration that works under vacuum is reported in **Figure VII.8**

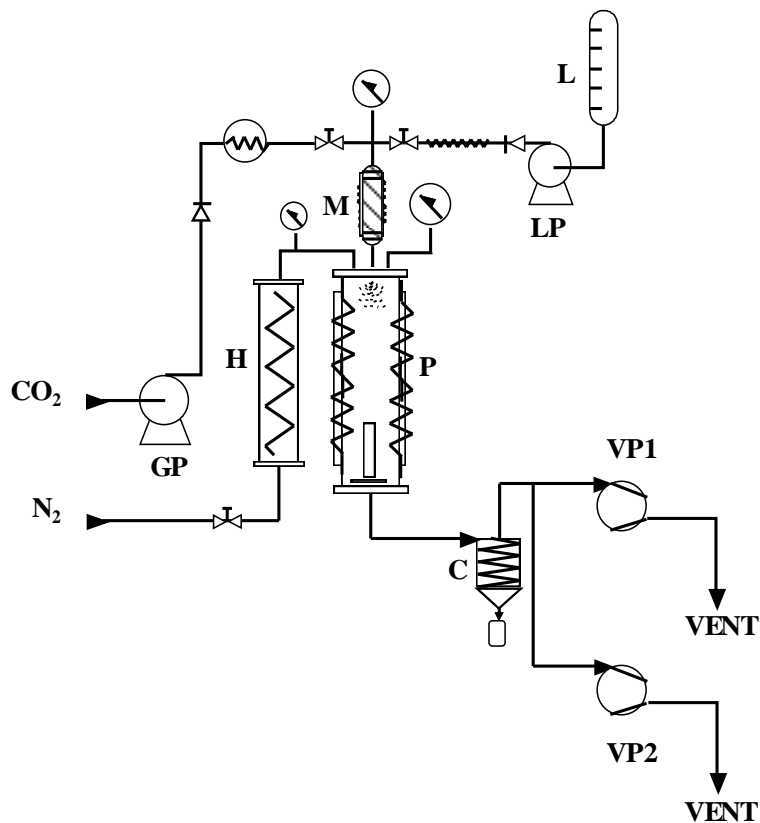


Figure VII.8 Configuration with vacuum system of SAA plant. GP: gas pump; H: heat exchanger; M: saturator; L: liquid feed; LP: liquid pump; P: precipitator; C: condenser; VP1 and VP2 vacuum pump

Chapter VII

Chapter VIII

Validation of the SAA plant in the configuration operated at reduced pressure

To validate the SAA plant in the new configuration, micronization test were performed. The chosen compounds are: protein, such as Bovine Serum Albumin, that is water soluble, and polymers with low glass transition temperature. The experiments were performed using different kind of solvents, water and organic solvents, therefore, the effect of CO₂ solubilization was evaluated.

VIII.1 Materials

VIII.1.1. *Bovine serum albumin*

Albumin is the most abundant serum protein. It is a globular protein with the approximate shape of a prolate spheroid (McClellan and Franses, 2003). It has several pharmacological and physiological functions:

- carrier of metals, fatty acids, cholesterol, bile pigments and drugs;
- regulator of the osmotic pressure;
- distributor of fluids between different compartments.

In general, albumin is the major antioxidant in the human plasma; many antioxidant activities of albumin result from its ligand-binding capacity. The flexibility of the albumin structure allows the adaptation of the protein sites to ligands; moreover, its three-dimensional structure provides many binding sites. Particularly the cationic ligands, like copper and iron, and transition metals, that can generate free radicals very quickly in presence of oxygen, do not form free radicals when are bounded with Bovine serum albumin (BSA).

The pulmonary route is a not invasive route for the administration of proteins for systemic therapy. For an effective inhalation fine particles

ranging between 1 and 5 μm are needed. The most used processes to obtain aerosolizable powders are spray drying, spray freeze-drying, lyophilization and emulsion drying. These processes have some limitation: they can denature the proteins and traces of the solvents could remain inside the particles.

BSA is very sensitive to high temperatures. The process of denaturation starts at about 65°C, at this temperature the denaturation is reversible; upon 65°C the unfolding of the BSA protein chain is irreversible (Kuznetsov et al., 1975, Lin and Koenig, 1976, Oakes, 1976).

Spray drying was proposed as micronization technique for BSA (Costantino et al., 2002). The temperature used for the processes induced several changes in the protein structure. Another technique for micronization of BSA is the spray drying under reduced pressure (Freitas et al., 2004); however the particles obtained have a mean diameter ranging from 15 to 24 μm .

As discussed in the introduction, Wang et al. (Wang et al., 2011) applied SAA to the micronization of BSA but the use of high temperature denatured the protein.

BSA (66 kDa, V fraction, γ globulin free) has been purchased from Sigma Aldrich.

VIII.1.2. Poly-L-Lactide Acid

Poly-L-Lactide Acid (PLLA) is a chiral form of Poly(lactic acid) or polylactide (PLA). This polymer is a biodegradable, thermoplastic, aliphatic polyester derived from renewable resources, such as corn starch (in the United States) or sugarcane (in the rest of world). Although PLA has been known for more than a century, it has only been of commercial interest in recent years, in light of its biodegradability.

PLLA has a crystallinity of around 37%, a glass transition temperature between 60-65°C, a melting temperature between 173-178 °C and a tensile modulus between 2.7-16 GPa.

PLLA is currently used in several biomedical applications, such as sutures, stents, dialysis media and drug delivery devices. It is also being evaluated as a material for tissue engineering.

Recently the FDA (Food and Drug Administration) has approved the PLLA injectable particles as a treatment for the dermal fat atrophy (Sadove, 2009). The microparticles of PLLA can be loaded with some drugs to produce aerosolizable formulation.

The microparticles can be obtained through Supercritical Fluid Precipitation Technology as proposed by Martin (Martin et al., 2002). The authors produced composite microparticles (PLLA-Budesonide) using the supercritical CO₂ as an antisolvent. The particles show a mean diameter of 1-2 μm , and they have a regular morphology.

Validation of the SAA plant in the configuration operated at reduced pressure

Liggins et al (Liggins and Burt, 2004) proposed the solvent evaporation as the technique to obtain PLLA microparticles loaded with Paclitaxel. The obtained particles had two size ranges: 1-15 μm and 35-105 μm with a regular morphology. This method does not allow to obtain particles with the required diameter: 1-5 μm for the aerosolizable formulations, and under 1 μm for the injectable formulations.

PLLA (Resomer L207S MW 85,000–140,000) and PLA (Resomer R203H; Mw:28000).

VIII.1.3. Polyethylene glycol

Many new compounds with recognized pharmaceutical activity cannot be commercialized due to low bioavailability connected to their poor water solubility. The formation of drug-polymer composites, in which the drug is uniformly dispersed in the polymeric matrix, allows to enhance the dissolution rate of the drug, increasing its bioavailability. From this point of view, the choice of the polymer is a crucial step. Indeed, it has to be approved for pharmaceutical applications, non-toxic, biodegradable (Barrett et al., 2008). Polyethylene glycol (PEG) is largely used in cosmetic, food and pharmaceutical industry, because it exhibits excellent biocompatibility, lack of toxicity and absence of immunogenicity (Izzo and Pappalardo, 2010, Yasugi et al., 1999, Barrett et al., 2008). In pharmaceutical industry, PEG can be used for the preservation, protection and restoration of cells, tissues or organ functions (Hauet and Eugene, 2008) and as a carrier, to manipulate the dissolution properties of active pharmaceutical ingredients (Izzo and Pappalardo, 2010, Anguiano-Igea et al., 1995, Barrett et al., 2008). One of the main advantages of the use of PEG as a carrier is the prevention of plasma protein adsorption of active nanoparticles (Vila et al., 2004b, Gref et al., 2000, Kursu et al., 2003, Ogris et al., 1999).

Micronization processes are commonly used to produce solid dispersions of polymers and drugs. Conventional processes are wet granulation, spray drying and spray freezing into liquid. The micronization of PEG by conventional processes is very difficult, since this polymer has low glass transition temperature and melting point (Törmälä, 1974, Craig, 1995), therefore, the produced particles tend to form agglomerates and/or films.

Spray drying was proposed for PEG coprecipitation with loperamide (Weuts et al., 2005), using dichloromethane as solvent and an evaporation temperature of about 50°C. Non negligible solvent residues were found in the precipitates, even after a further vacuum drying. No information was given about particle sizes and morphology. Spray freezing into liquid was also proposed (Barron et al., 2003) for PEG particle size reduction; it was performed into a cryogenic liquid at -50°C and under vacuum (0.7 mbar), using water as solvent and a liophylization step was required as post processing. The obtained particles had a mean diameter of 50-100 μm and

showed a spherical shape only if the liquid feed rate was very small (2 mL/min).

Summarizing, PEG microparticles can have many relevant applications, but PEG processing is still problematic. Supercritical fluids have been proposed to improve several industrial processes and supercritical carbon dioxide (SC-CO₂) based techniques to obtain microparticles with low or no residual solvent and a narrow particle size distribution (Reverchon et al., 2009, Reverchon et al., 2003, Caputo et al., on-line (ASAP)). However, only few examples of supercritical fluid based processes applied to the micronization of PEG can be found in literature. PEG micronization has been proposed from gas saturated solution (PGSS) (Nalawade et al., 2007). In this process CO₂ is dissolved in the polymer and the solution is expanded through a nozzle; the consequent Joule-Thompson effect induces a lowering of temperature and the solidification of the polymer. Tests performed on PEG6000 and PEG10000, using two different nozzles and different process conditions, produced irregular large particles with mean diameters ranging between about 200 and 350 μm. Rapid expansion of a supercritical solution with a nonsolvent (RESS-N) was also attempted for PEG micronization. A low molecular weight alcohol was used as cosolvent to obtain a reasonable PEG solubility in CO₂ (Matsuyama et al., 2003, Mishima et al., 2000). Particles with well defined morphology were obtained with a mean dimension of about 10 μm. Barret et al (Barrett et al., 2008) proposed gas antisolvent process (GAS), to obtain itraconazole loaded PEG20000 microparticles; but, coprecipitation was unsuccessful since the two compounds precipitated separately and the particles were irregular. Summarizing, supercritical CO₂ based techniques used until now were only partially successful in PEG micronization and limitations were experimented, similar to the ones of traditional techniques (Reverchon et al., 2010b, Caputo et al., 2010).

PEG (Mw:10000 and Mw: 6000) were purchased by Aldrich Chemical Co.

VIII.1.4. Coprecipitates PLA-PEG

Aliphatic polyesters attract increasing attention from both academic and industrial viewpoint as biodegradable and biocompatible synthetic materials, because of their important applications in pharmaceutical, medical, and biomedical engineering fields. Despite the PLLA high biocompatibility, non-toxicity, and biodegradability, its high crystallinity, low rate of degradation, and hydrophobicity constitutes significant drawbacks for the biomedical applications (Izzo and Pappalardo, 2010).

To overcome these limitations, copolymerization of PLA with hydrophilic poly(ethylene glycol) (PEG) has been studied. PLA-PEG diblock or triblock copolymers have been described in the literature, and a

Validation of the SAA plant in the configuration operated at reduced pressure

brilliant achievement has been the possibility to modulate the biodegradation rate and the hydrophilicity of the materials by adjusting the ratio between the hydrophilic and the hydrophobic parts; furthermore, previous studies have shown the importance of the PEG chain length for preventing plasma protein adsorption onto PLA-PEG (Vila et al., 2004a).

“Tree shaped” copolymers made of a poly(ethylene glycol) trunk and poly(lactide) (PLA) arms have been recently synthesized (Izzo and Pappalardo, 2010). The adopted chemical approach allowed the tuning of molecular weight, polydispersity and number of branching, whereas the physical properties were related to the copolymers architectures. It is foreseen that these materials could be also suitable as drug delivery systems, affording modulated behavior as a function of the number of branches, of the relative amount of the blocks and of the stereoregularity of the polylactide arms.

An interesting property of these particles is their reduced uptake by the mononuclear phagocytic system (MPS) in comparison to that of the uncoated Poly(lactic acid) (PLA) particles. The drug targeting is based on the micelle-forming propensity of PEG-PLA block copolymers in an aqueous medium through multi-molecular association. Polymer micelles prepared from various types of amphiphilic block copolymers including PEG-PLA are characterized by a core-shell architecture, in which a segregated core of associated hydrophobic segments is surrounded by a dense palisade of tethered hydrophilic chains (Yasugi et al., 1999).

Micronization is a widely diffused process, used to improve the bioavailability of pharmaceutical compounds and to allow the use of alternative routes for their administration. Micronization of PLA-PEG copolymers has been proposed by Vila et al. (Vila et al., 2004a) starting from simple and double emulsions. Other authors (Essa et al., 2010) prepared nanoparticles of PLA-PEG copolymers using the solvent evaporation of emulsions; however, the particles did not have a regular morphology. Lacasse et al. (Lacasse et al., 1998) reported spray drying to produce microparticles of PLA-PEG. The particles obtained tended to form agglomerates, probably because the drying temperature was very close to the glass transition temperature of the copolymer. Generally speaking, the difficulty of the traditional techniques in processing these copolymers, is related to their low glass transition temperature: solvent evaporation from emulsions and spray drying require relatively high temperatures and not well defined spherical particles are generally produced.

Supercritical assisted techniques were proposed to overcome the limitations cited above. Solution Enhanced Dispersion by Supercritical CO₂ (SEDS) was proposed to prepare nanoparticles of PLA-PEG copolymer for sustained release of siRNA (small interference ribonucleic acid). The presence of PEG reduces the burst effect and drug can be released more slowly than the system formed by PLA alone (Jacobson et al., 2010). Even if

Chapter VIII

very small particles were obtained, with a mean diameter of about 20 nm, no evaluation of loading were reported, since, it is very difficult to obtain coprecipitates using SC-CO₂ as an antisolvent.

The copolymers used in this work were synthesized by Izzo et al. (Izzo and Pappalardo, 2010) in the Department of Chemistry at University of Salerno.

The properties of the copolymers are reported in **Table VIII.1**

Table VIII.1. Properties of copolymers PLA-PEG. *M_w*, weight average molecular weight; *M_n*, number average molecular weight evaluated from NMR analysis [64]; *PI*, polydispersity index; *T_m*, melting temperature; ΔH_f , enthalpy

architecture	Lactide	<i>M_w</i> [kDa]	<i>M_n</i> [kDa]	PI	% PLA	<i>T_m</i> [°C]	ΔH_f [J/g]
Linear	L (2 gr)	11149	9543	1.17	47.4	151	39
Branched G1	L (2 gr)	18617	15702	1.18	56.6	161	55
Branched G1	L (4 gr)	n.d.	n.d.	n.d.	n.d.	n.d.	n.d.
Branched G2	L (4 gr)	20382	13519	1.51	70.6	157	46
Branched G2	D, L (3 gr)	19792	16762	1.21	71	n.d.	n.d.

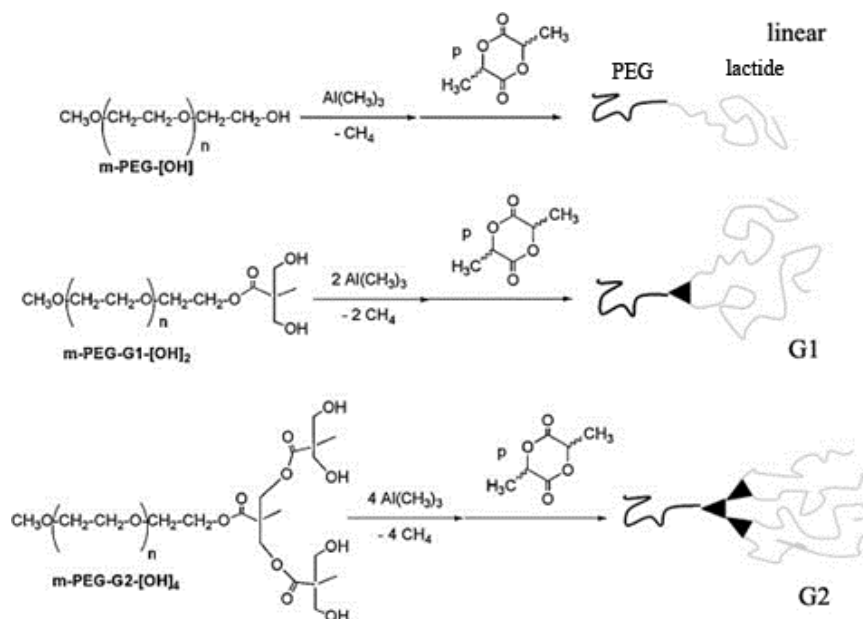


Figure VIII.1 Schematic representation of copolymeric architectures synthesized in this work (Izzo and Pappalardo, 2010).

It is important to remark that the polymer architecture influences not only the morphological and the physical-mechanical properties of the polymer, but also various facets of the drug delivery systems. Indeed, lactide branches allow to reduce dissolution rate of active molecules, moreover, the presence

Validation of the SAA plant in the configuration operated at reduced pressure of functional end group favors different interaction with cells (Izzo and Pappalardo, 2010).

VIII.1.5. Coprecipitates: PEG α -tocopherol acetate

α -Tocopherol acetate (α -TCP) is a lipophilic vitamin. It is an antioxidant and prevents cardiovascular diseases and cancer. However, the use of α -TCP is limited because it is thermolabile and suffers the presence of light and oxygen; moreover, it loses stability if dispersed in water because hydrolysis processes take place. To avoid these problems encapsulation of this vitamin or graft to succinate PEG has been proposed (Sheu et al., 2006). In addition α -TCP does not dissolve in water and surfactants are added in the formulation to enhance bioavailability (Yoo et al., 2006, Somchue et al., 2009).

Emulsion evaporation has been proposed to encapsulate lipophilic vitamins into biodegradable polymers, such as poly(lactic-co-glycolic)acid (PLGA) (Matsumoto et al., 2008) or inorganic compounds, as silica (Hwang et al., 2005). This process is time consuming and a large amount of organic solvents remains in the final product. To overcome this limitation some supercritical fluid based techniques have been proposed. For example, Supercritical antisolvent precipitation was used to produce microparticles of PEG and carotene, a lipophilic vitamin (He et al., 2007). All the techniques, mentioned above, do not allow an efficient micronization of PEG in terms of morphology, dimensions and processing times.

To overcome these limitations SAA at reduced pressure has been proposed to produce microspheres of PEG and α -TCP. This technique allows to operate at conditions that do not induce the degradation of vitamin and the softening of the polymer. The final formulation has the aim of protecting the vitamin during its storage and of enhancing its bioavailability.

α -tocopherol acetate semisynthetic was purchased by Aldrich Chemical Co.

VIII.2. Results and discussion

PLLA and BSA processability was investigated for the first validation of SAA in the vacuum configuration, new experiments were performed to understand how SAA process parameter could influence the morphology and precipitates size of the particles obtained using these solutes. Moreover, other experiments were performed on PEG, PEG-PLA copolymer and PLGA to verify the processability of polymers with a low glass transition temperature using SAA plant in the configuration operated at reduced pressure.

VIII.2.1. BSA

Behavior of the system water-SC-CO₂.

In the SAA process the choice of the proper conditions in the saturator is fundamental to produce microparticles, since, the solubilisation of SC-CO₂ in the liquid feed is considered as the key of the technique. However, many compounds are not soluble in organic solvents, as, for example, proteins such as albumin. When water is used as solvent in SAA process, only a limited amount of CO₂ can be solubilized in the liquid solution since, differently from the organic solvent, the mutual solubility of the two compounds is very low at the usual SAA process conditions [66]. When the quantity of CO₂ exceeds the solubility value, an heterogeneous mixture is formed in the saturator. The presence of CO₂ solubilized in water reduces the viscosity and surface tension of the solution; whereas CO₂ not solubilized, enhances the pneumatic effect in the injector, supplementing the nozzle pressure difference and improving primary atomization (Adami et al., 2009, Caputo et al., 2010). The GLR set for the water-CO₂ system was 1.8 (Adami et al., 2009), that corresponded to a CO₂ molar fraction of 0.4.

In a previous work BSA micronization by SAA was attempted with precipitation pressure of 2 bar, that is pressure reached in the precipitator without the vacuum system; the result was the denaturation of the protein that became hydrophobic (Della Porta et al., 2010).

However, if BSA has to be used as an active biomolecule its denaturation has to be avoided. Therefore, an accurate selection of the precipitation temperatures is requested, below the irreversible denaturation temperature of the protein. The preliminary experiments on BSA have been completed with experiments performed changing the temperature in the precipitator to understand how this parameter influence particles size and morphology and protein stability.

Validation of the SAA plant in the configuration operated at reduced pressure

Variation of the temperature in the precipitation vessel

To understand how the precipitation temperature influences the morphology and the structure of BSA, some tests were performed keeping constant all the operative conditions, 60°C and 100 bar in the saturator, but setting the precipitation temperature at 80°C and 60°C. Table 2 shows the operative condition used for the experiments:

Table VIII.2 Selected experiments performed using SAA equipped with the vacuum system. (T_p : precipitation temperature; p_p : precipitation pressure; T_m : saturator temperature; p_m : saturator pressure; c : solute concentration; GLR: gas to liquid ratio; Q_{CO_2} : CO_2 flow rate; Q_{LIQ} : solvent flow rate; Q_{N_2} : N_2 flow rate).

n. test	solute	solvent	c mg/mL	GLR w_{CO_2}/w_{liq}	T_p °C	p_p Bar	Q_{CO_2} [gr/min]	Q_{LIQ} [mL/min]	Q_{N_2} [L/h]	T_m °C	p_m bar
BSA_p01	BSA	H ₂ O	20	1.8	80	0.80	8.79	4.88	1224	61	80
BSA_p02	BSA	H ₂ O	20	1.8	60	0.87	8.79	4.88	1224	60	83

The pressure in the precipitation vessel was only partially reduced because water has great cohesive forces and high surface tension, therefore it can act as an obstacle in the pores of the filter put on the bottom of the precipitator, producing a larger pressure drop. As a consequence, the lower pressure obtainable in the precipitator was about 0.8 bar.

Examples of the produced BSA particles are reported in **Figure VIII.2**.

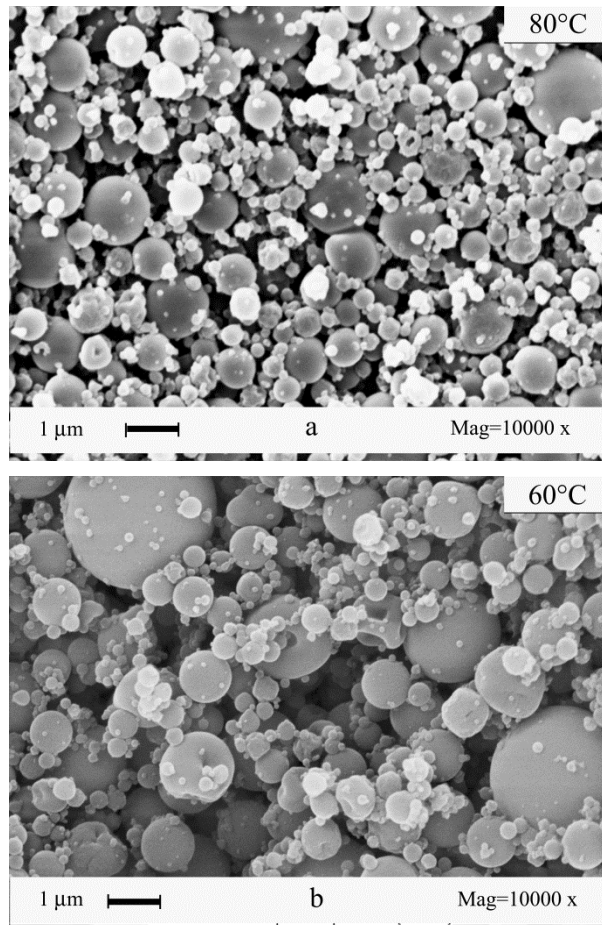


Figure VIII.2 SEM images showing the effect of precipitation temperature on the morphology of BSA microparticles. The operating conditions set in the precipitator were 80°C (a) and 60°C (b). See **Table VIII.2**.

SEM photomicrographs show that precipitation temperature did not affect the morphology, but the particle dimensions. These were quantitatively measured from SEM photomicrograph elaboration and using DLS analysis; the results are reported in **Figure VIII.3**.

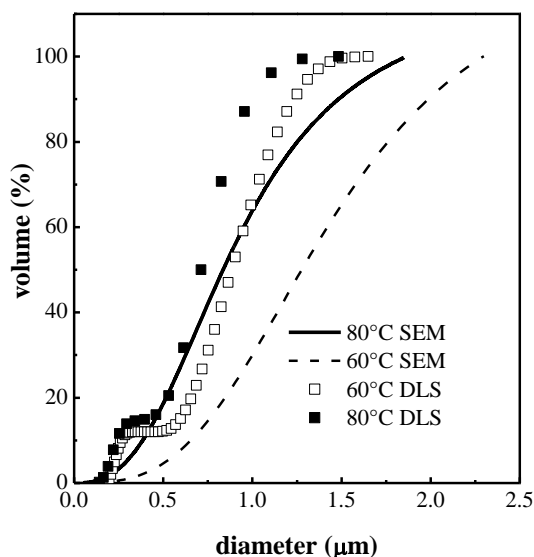


Figure VIII.3 PSD of BSA powders obtained by SAA operating at 0.8 bar and at different precipitation temperatures. The calculations were performed in terms of volumetric cumulative percentages.

SEM analysis gave a mean size ranging from 0.8 to 1.5 μm and a standard deviation of about 0.7. DLS analysis gave the additional information that probably two populations of particle were present in the sample, in particular one population was smaller than 250 nm, the other one, that represents the 80% (v/v) of the population, was smaller than 1.5 μm . In this case, the measurements made with the two techniques gave relatively different results; but, both techniques confirmed that the particles obtained at 80°C in the precipitator were smaller than those obtained setting the lower temperature. This result was not surprising, since previous works on SAA (Reverchon et al., 2007a) demonstrated that an increase of temperature allows the formation of smaller particles, due to a reduction of the viscosity of the sprayed system.

Characterization of BSA microparticles

To verify the success of the new SAA configuration, BSA structure of SAA processed particles was analyzed. FTIR is considered the proper analysis to investigate the degradation degree of a processed protein (Fu et al., 1999, Jeyachandran et al., 2009). The spectra in the mid-infrared range of polypeptides are divided by three regions: Amide I (1700-1600 cm^{-1}), Amide II (1600-1500 cm^{-1}) and Amide III (1320-1230 cm^{-1}) (Parker, 1986).

Chapter VIII

The Amide II band is believed to be not very sensitive to the conformation of the protein (Parker, 1986); the Amide III is approximately an order of magnitude less intense than Amide I. In the Amide I region, the observed stretching frequency of the bands depends on the secondary structure of the peptide chain (Bummer, 1996). Component bands, in the region of 1650 to 1658 cm^{-1} , are assigned to α -helix (Bummer, 1996); the infrared spectra related to β -sheet exhibit a low intensity region (1620-1640 cm^{-1}) and a high intensity region (1670-1695 cm^{-1}) (Bummer, 1996). The overall FTIR traces of raw material and SAA processed BSA are very similar; therefore, we decided to compare the relative intensity of the α -helix peaks of untreated BSA and SAA processed BSA, using also the data from literature (Mishra et al., 1996), to understand how the SAA process influenced the secondary structure of the peptide chain. The second order derivative method was applied to enhance the resolution of overlapping IR bands and to identify the secondary structures of the protein. The analysis revealed an α -helix content, referred to the percentage area of the peak at 1654 cm^{-1} , of about 32%, for the microparticles obtained setting 60°C in the precipitator, and 14%, for the particles obtained at 80°C. Considering that in the saturator a decrease of pH takes place, due to the presence of solubilized CO_2 (Spilimbergo et al., 2002), it is reasonable the comparison with the α -helix content of BSA processed by SAA with the value proposed by Mishra et al (Mishra et al., 1996) (about 32% at pH=2). It confirms that the SAA process conditions, obtained using the new process arrangement, have not modified the protein structure.

These results were supported by the results of BSA solubility tests in water. BSA particles produced operating at 60°C dissolved very fast in water: their dissolution time was close to the dissolution time of the untreated BSA, demonstrating that the protein maintained its hydrophilic characteristic. BSA particles obtained at 80°C dissolved very slow in water, confirming that some modifications occurred in the protein structure, inducing a relatively hydrophobic behavior.

Discussion

The experiments reported above demonstrated that SAA plant in the new configuration can be considered as the proper technique to avoid denaturation of BSA microparticles. The denaturation of the protein is related to the value of the temperature used in the saturator and in the precipitator, whereas the decreasing in pH, that takes place in the saturator, does not influence the proteic structure, since, the protein has a low residence time in the saturator. Moreover, the tests performed at different precipitation temperatures demonstrated that at higher temperatures in the precipitator it is possible to obtain smaller particles than operating at lower temperatures. This phenomenon is due to the lowering of viscosity of the solution that takes place at higher temperatures.

VIII.2.2. PLLA

Behavior of the system chloroform-SC-CO₂.

When an organic solvent is used the efficiency of the atomization process depends on the quantity of CO₂ solubilized in the liquid solution contained in the saturator (Reverchon, 2002a). Assuming that the solute has not a relevant influence on the vapor liquid equilibria (VLEs), the formation of an homogeneous mixture is assured if the SAA operative point is located in the one phase region of the VLE diagram for the binary system solvent-CO₂(Reverchon, 2002a). In a previous work (Reverchon and Antonacci, 2007), PLLA microparticles were obtained by SAA using dichloromethane (DCM) as solvent. They had an irregular morphology; therefore, in this work, chloroform was selected to produce PLLA microparticles. The operating conditions were chosen on the basis of the data on VLEs of the system chloroform-supercritical CO₂, reported in **Figure VIII.4**, where the diagram is constructed using the experimental data at 80°C from the literature (Peters and Florusse, 1995).

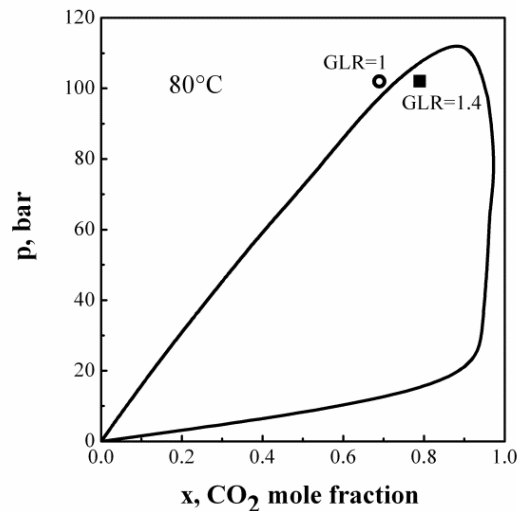


Figure VIII.4 High pressure vapor liquid equilibria at 80 °C; experimental data adapted from Peters et al (Peters and Florusse, 1995), for the binary system CO₂-CHCl₃.

Due to the uncertainties about the VLE behavior of the ternary system chloroform-PLLA-CO₂ with respect to the binary system, a first test was performed setting at 0.8 the CO₂ molar fraction, corresponding to a gas to liquid ratio (GLR w/w) of 1.4. An heterogeneous mixture should be

Chapter VIII

obtained. Operating in this condition the precipitation of PLLA on the surface of the internal packings of the saturator took place. Decreasing the GLR to 1, that corresponds to a CO₂ molar fraction of 0.7, the operative point is located in the one phases region (Figure 7) and the formation of an homogeneous mixture can be expected. Operating in these conditions, no polymer residues were found in the saturator at the end of the experiment. Supercritical CO₂ induces the reduction of polymer solubility in the solvent selected for these experiments (De Gioannis et al., 2004), up to values that induce the precipitation of the polymer from the liquid phase; decreasing the amount of CO₂ in the mixture it is possible to avoid the precipitation of the compound in the saturator.

The formation of dried particles in the precipitator is due to the fast evaporation of the solvent. The presence of the solute increases the boiling point of the solvent and, as a consequence, the temperature required in the precipitator. Pressure reduction in the precipitator leads to the decrease of the boiling point of the solvent and allows fast droplet evaporation at lower temperatures.

When PLLA was processed and the vacuum system was not used, a precipitation temperature near the glass transition temperature of the polymer was required for droplet evaporation and PLLA particles tended to form a membrane like structure on the filter (Reverchon and Antonacci, 2007). This phenomenon was probably due to the softening of the particles, in a process similar to the sintering of metals, in which a partial fusion of the particles took place at a temperature slightly lower than the fusion temperature and a porous structure was formed (Samyn et al., 2006).

Variation of temperature at different precipitation pressure

The use of the new SAA configuration with the vacuum pumps allowed to set lower precipitation temperatures and to perform experiments at different precipitation pressures. Some tests were performed setting 30°C and 40°C in the precipitator, keeping constant all other process parameters (see **Table VIII.3**).

Validation of the SAA plant in the configuration operated at reduced pressure

Table VIII.3 Selected experiments performed using SAA equipped with the vacuum system. (T_p : precipitation temperature; p_p : precipitation pressure; T_m : saturator temperature; p_m : saturator pressure; c : solute concentration; GLR : gas to liquid ratio; Q_{CO_2} : CO_2 flow rate; Q_{LIQ} : solvent flow rate; Q_{N_2} : N_2 flow rate).

n. test	solute	solvent	c	GLR	T_p	p_p	Q_{CO_2}	Q_{LIQ}	Q_{N_2}	T_m	p_m
			mg/mL	w_{CO_2}/w_{liq}	°C	bar	[gr/min]	[mL/min]	[L/h]	°C	bar
PLLA_p01	PLLA	$CHCl_3$	20	1	30	0.65	8.06	5.48	686	79	102
PLLA_p02	PLLA	$CHCl_3$	20	1	40	0.65	8.06	5.48	686	81	105
PLLA_p03	PLLA	$CHCl_3$	20	1	30	0.50	8.41	5.72	340	79	102
PLLA_p04	PLLA	$CHCl_3$	20	1	40	0.50	8.06	5.48	340	79	103

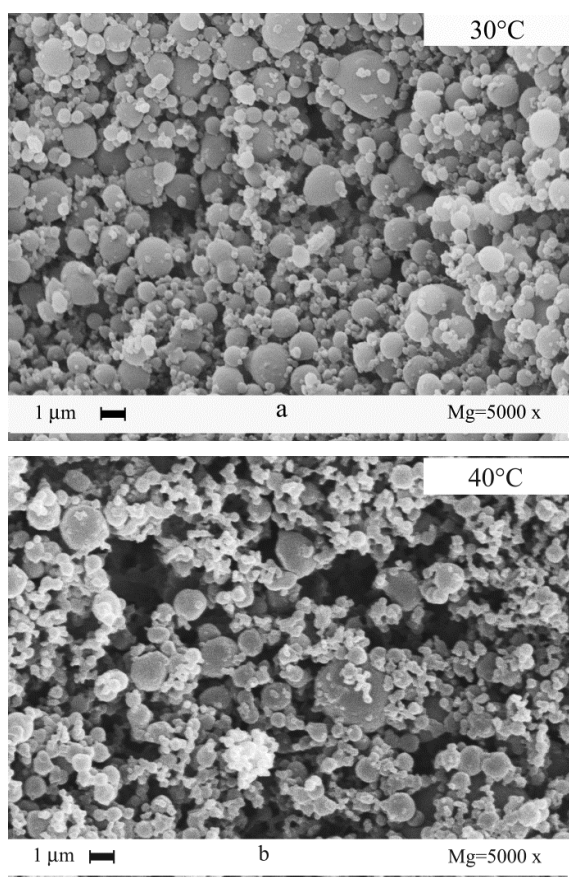


Figure VIII.5 SEM images showing the effect of the precipitation temperature on the morphology of PLLA microparticles obtained using SAA. Different temperatures were set in the precipitator: 30°C (a) and 40°C (b). See Table VIII.3.

SEM photomicrographs, reported in **Figure VIII.5**, show that the particles obtained setting 30°C in the precipitator did not form agglomerates; whereas, the particles obtained operating at 40°C were still partially fused altogether. The experimental evidence, at 30°C, confirmed that the new SAA process scheme was successful in the production of particles at lower temperatures.

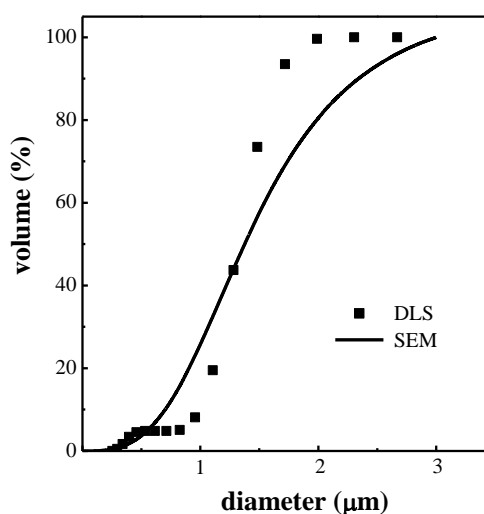


Figure VIII.6 Particle size distribution (PSD) of PLLA powders obtained by SAA operating at 0.65 bar and 30°C in the precipitation vessel. The calculations were performed in terms of volumetric cumulative percentages.

PSD of the obtained particles was investigated calculating particle diameter from SEM photomicrographs and by DLS. **Figure VIII.6** shows a comparison between the integral PSDs of PLLA particles, obtained operating at 30°C, using the two different analytical methods. SEM images analysis and DLS differ for sample preparation, number of analyzed particles and for the measuring principle. Therefore, it is interesting to observe that, though some differences in the curves, mean diameter (around 1.3 μm) and standard deviation (around 0.4) are similar for both the measuring techniques.

A further series of experiments was performed setting lower nitrogen flow rates (340 L/h instead of 686 L/h), that allowed to produce an even lower pressure in the precipitator (0.5 bar), since the overall amount of gas to be treated by the vacuum system was smaller. At the same time, a decreasing of the inert gas flow rate lowered the droplet evaporation rate and could affect the morphology of the particles.

Validation of the SAA plant in the configuration operated at reduced pressure

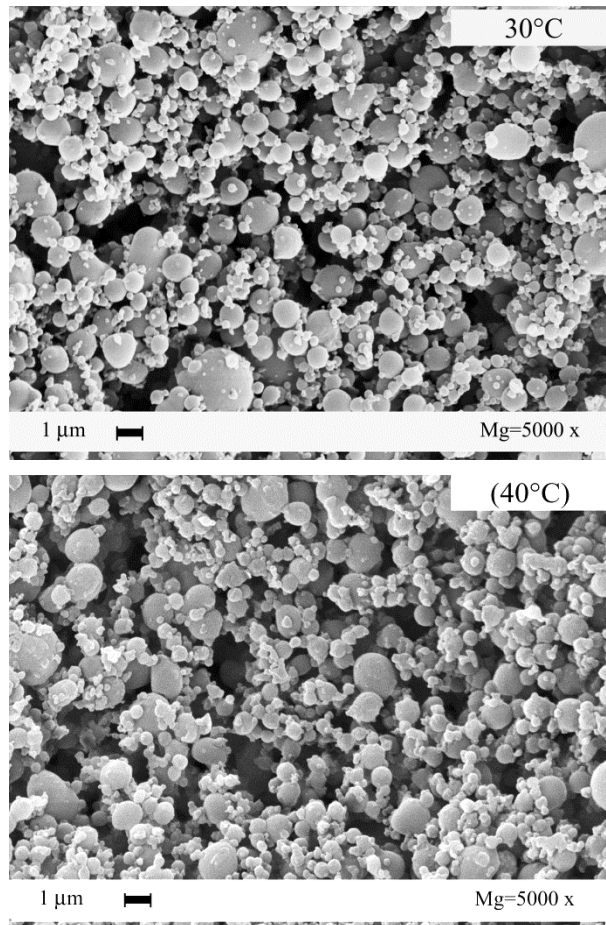


Figure VIII.7 SEM images showing the effect of precipitation temperature on the morphology of PLLA microparticles obtained using SAA. Saturator operated at 80°C, 100 bar; precipitator operated at 30°C (a) and 40°C (b), 0.5 bar. See Table VIII.3.

Figure VIII.7 shows that, operating at 0.5 bar, particles with a regular morphology were also obtained. The PSDs of PLLA particles produced in these experiments were analyzed from SEM photomicrographs and reported in **Figure VIII.8**.

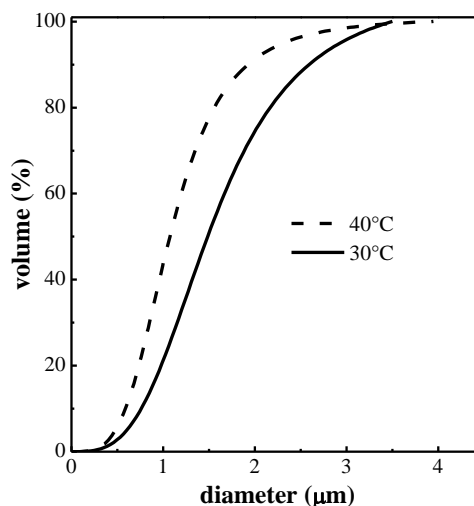


Figure VIII.8 PSD of PLLA powders obtained by SAA operating at 0.5 bar and at different temperatures in the precipitation vessel. The calculations were performed in terms of volumetric cumulative percentages.

The particles obtained at a higher temperatures (40°C) were smaller, with a mean diameter of 1 μm, whereas the particles obtained at 30°C had a mean diameter of 1.5 μm. This difference is probably due to the reduction of viscosity of the liquid at the exit of the injector (Reverchon et al., 2007a).

Solvent Residue

The solvent residue was analyzed to verify that chloroform content, in PLLA produced particles, was lower than the FDA limit, that is 60 ppm. The analysis revealed that the solvent residue was around 15 ppm (± 2) for all the particles produced at the different process conditions. This result confirmed that the particles produced using SAA plant in the new configuration were suitable for pharmaceutical formulations.

Solid state

The solid state of PLLA particles produced by SAA was investigated by XRPD (**Figure VIII.9**) and DSC (**Figure VIII.10**).

Validation of the SAA plant in the configuration operated at reduced pressure

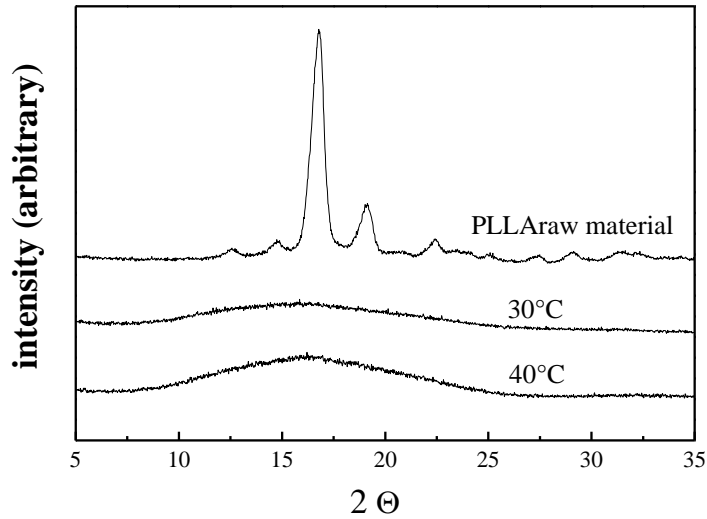


Figure VIII.9 XRPD of PLLA untreated (raw material) and PLLA microparticles produced by SAA process at different temperatures (30°C and 40°C) in the precipitation vessel.

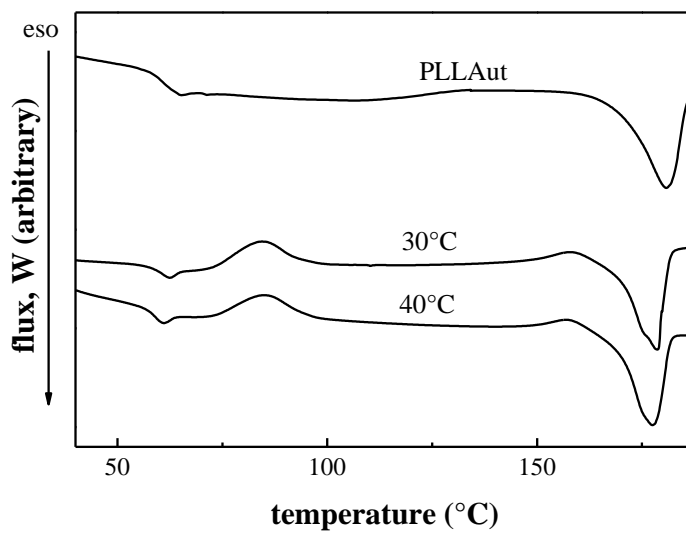


Figure VIII.10 Thermograms of untreated raw material and SAA produced PLLA microparticles at different temperatures (30°C and 40°C) in the precipitation vessel.

Chapter VIII

XRPD diagrams show that the particles obtained by SAA are amorphous, since the characteristic peaks of the crystalline state, showed by the XRPD diagram related to the raw material, are not present. DSC analysis confirmed that the particles obtained by SAA were amorphous, indeed an exothermic peak, at about 85°C, for all processed samples, is present, attributable to the crystallization phenomenon. The more pronounced glass transition temperature, with respect to the raw material, was due to the aging of the polymer (Pan et al., 2008) caused by the SAA process.

Discussion

The experiments described above demonstrated that SAA plant in the new configuration can be considered as a proper technique to obtain microparticles of PLLA with a well defined spherical shape. The particles that can be obtained are amorphous. As in the case of BSA precipitation temperature influences the mean dimensions of the obtained particles, indeed, operating at higher temperatures it is possible to obtain smaller particles. This is due to the reduction of viscosity that takes place at higher temperatures. However it is not possible to obtain sub-micro particles because it is not possible to operate at temperatures close to the glass transition temperature of the polymer.

VIII.2.3. PEG

Behavior of the system acetone-SC-CO₂

PEG can be dissolved in water or in organic solvents. As previous discussed, the use of water as solvent induces the increase of cohesive forces that act as an obstacle in the pores of the filter. For this reason we used acetone as solvent for micronization to operate at low pressures and temperatures in the precipitator. The experiments were performed using PEG at different molecular weights: 6000 and 10000 kDa.

The vapor-liquid equilibrium (VLE) between SC-CO₂ and acetone (Pan et al., 2008) (**Figure VIII.11**) gives some indications about the proper conditions that have to be set in the saturator in order to obtain one phase flow and to avoid the precipitation of the polymer on the packing of the mixer.

Validation of the SAA plant in the configuration operated at reduced pressure

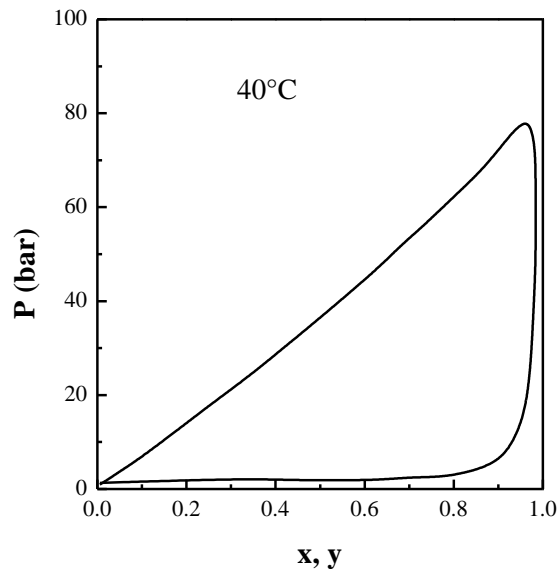


Figure VIII.11 VLE of the system CO₂-acetone, at 40°C, adapted from Sato et al [77].

Therefore, some preliminary tests at different CO₂ molar fractions were performed, to verify that single phase conditions were obtained. Successfully results were obtained using a gas to liquid ratio (GLR) of about 3.5 (w/w), and, no material was precipitated in the saturator by antisolvent effect.

A first SAA experiment was performed using the standard plant configuration, in which the precipitation is obtained at atmospheric pressure. Temperature and pressure in the saturator were set at 40°C and 67 bar, respectively. CO₂ flow rate was of about 9 g/min and a liquid flow rate of PEG6000 dissolved in acetone of about 3 mL/min was used. Solute concentration was 20 mg/mL; precipitation temperature was set at 50°C, with a nitrogen flow rate of 690 NL/h, used to allow the evaporation of the solvent. At the end of the process, a film of PEG, formed by interconnected filaments, was found on the collection filter, as shown in **Figure VIII.12**; moreover, the extensive formation of this film, induced a progressive increase of the pressure in the precipitator by blockage of the filter pores.

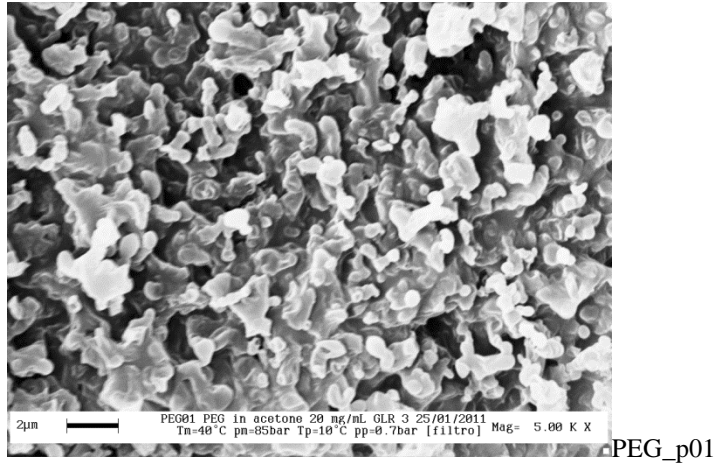


Figure VIII.12 SEM images showing the effect of high precipitation temperature on the morphology of PEG microparticles.

This result can be due to the temperature in the precipitator that induces the softening of the produced particles and the connection among their surface. Operating at a lower temperature in the precipitator, 5°C, it is possible to obtain no agglomerated particles, as shown in **Figure VIII.13**:

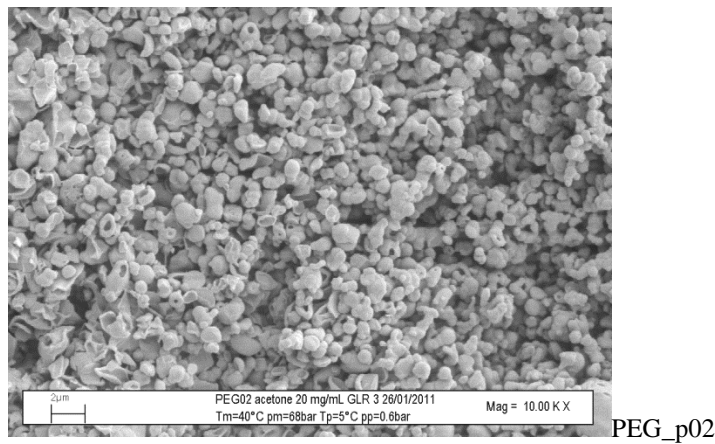


Figure VIII.13 SEM images showing the effect of low precipitation temperature on the morphology of PEG microparticles. The operating conditions set in the precipitator were 5°C and 0.6 bar.

However, SEM photomicrograph shows that some particles collapsed on themselves, forming a sheet-like aggregate shape, probably because their structure was not stable; moreover, the impact with the metallic frit might have broken them. To understand if concentration of the polymer in the liquid feed could influence the structure of the particles some experiments were performed changing this. The particles consist of hollow and/or

Validation of the SAA plant in the configuration operated at reduced pressure imploded microspheres. This morphology is the result of the formation of spherical droplets and of the subsequent breakage of the particles, due to the fragility of the polymer, that can be correlated to its low molecular weight (Al-Nasassrah et al., 1998).

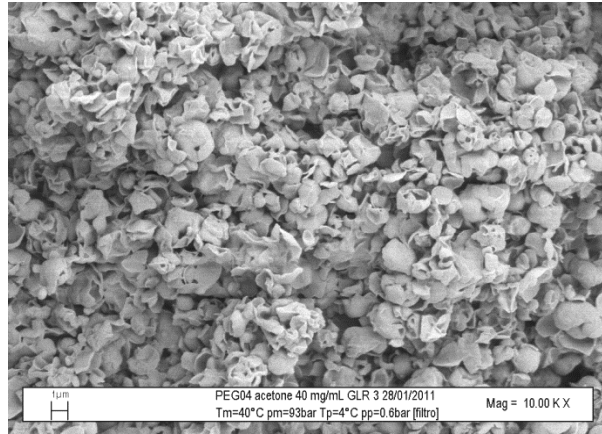
A similar phenomenon has been sometimes observed during spray drying (Seydel et al., 2006), in this process, when supersaturation of the solute is reached, the formation of a solid shell takes place on droplet surface; the solvent that leaves the droplet thorough the solid shell can break or shrink the particle. This phenomenon is more evident when the polymer has a low molecular weight (Al-Nasassrah et al., 1998). To avoid this problem, all subsequent experiments were performed using PEG10000.

Variation of polymer concentration

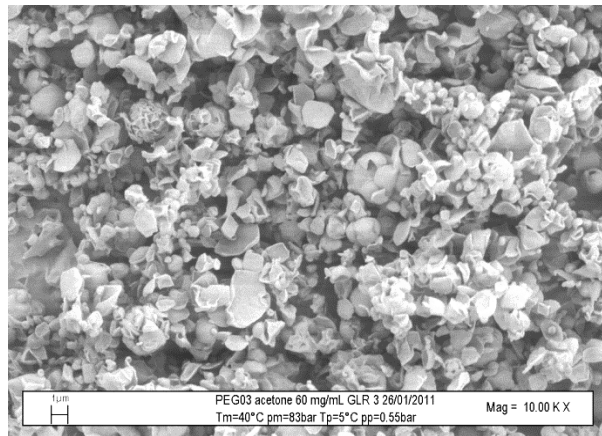
In the experiments on BSA and PLLA we noticed that the solute did not modify the vapor liquid equilibria of the system solvent-CO₂, when a low concentration of solute is used (20 mg/mL). In this section we want to study the correlation between the particles morphology and the concentration of solute in the liquid feed. **Figure VIII.13** shows the particles obtained setting 20 mg/mL.

Figure VIII.14 shows the particles obtained setting 40 mg/mL and 60 mg/mL.

Chapter VIII



PEG_p03 40 mg/mL



PEG_p04 60 mg/mL

Figure VIII.14 SEM images showing the effect of concentration on the morphology of PEG microparticles; 40 mg/mL (p03) and 60 mg/mL (p04).

Increasing the concentration an increase of particles with sheet shape can be observed. PSD diagram (**Figure VIII.15**) shows that the particles obtained at high concentration are bigger.

Validation of the SAA plant in the configuration operated at reduced pressure

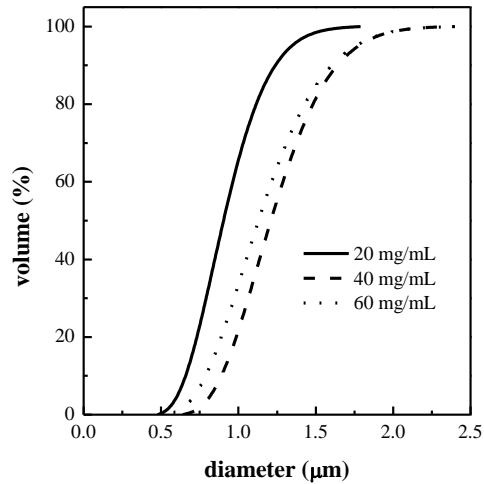


Figure VIII.15 PSD of PEG 6000 powders obtained by SAA at different concentration of solute in the liquid feed. The calculations were performed in terms of volumetric cumulative percentages by DLS analysis.

The high concentration of polymer in the liquid feed increases the viscosity of the system, therefore, the efficiency of the atomization process decreases. Moreover, the presence of a high amount of solute changes the boiling point of the solvent and, as a consequence, the evaporation rate. In this case the precipitation of the polymer takes place faster than the evaporation process and particles with high void degree are formed. Those particles have a highly fragile structure; therefore, when they impact with the filter they could be broken forming sheets.

Using the higher PEG molecular weight, and maintaining the same SAA process conditions previously discussed, we performed a new series of experiments (see **Table VIII.4**), in which the influence of SAA process parameters on particle size and distribution was performed using PEG10000 (see **Figure VIII.16**).

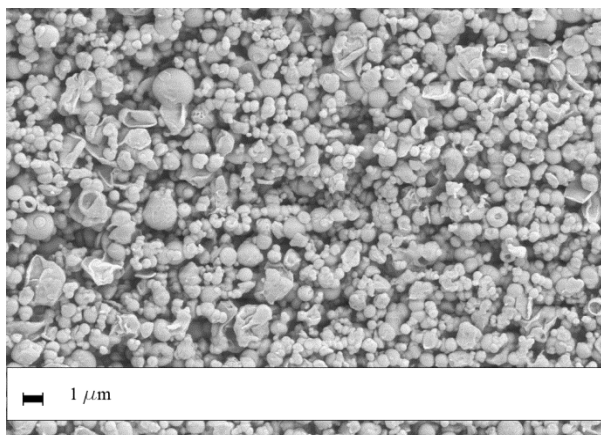


Figure VIII.16 SEM images showing the microparticles obtained using PEG (M_w :10000). Set conditions 18°C and 0.8 bar in the precipitator and 40°C and 67 bar in the saturator.

In this case we can observe a decrease of the percentage of particles with sheet shape. This because the structure of the particles is less fragile and cannot be broken by the impact with the filter. Moreover this test demonstrated that, using PEG 10000 as solute, it is possible to operate at higher temperature in the precipitator, 20°C, whereas using PEG 6000 operating at 10°C only membrane like structure was obtained.

Effect of PEG10000 concentration

During this series of tests, all SAA process conditions were the same used in the previous experiments (see **Table VIII.4**), except the precipitation pressure and temperature, that were set at 0.8 bar and 5°C, respectively. PEG concentration in acetone was varied from 20 to 60 mg/mL.

Validation of the SAA plant in the configuration operated at reduced pressure

Table VIII.4 Selection of SAA tests performed on PEG6000 and PEG10000: SAA operating conditions, and particle size. Solvent: acetone; CO₂ flow rate 9 g/min; liquid flow rate 3 mL/min; GLR = 3.5; nitrogen flow rate 690 NL/h; saturator operating conditions 40 °C and 67 bar.

<i>test</i>	<i>Solute</i>	<i>C</i> [mg/mL]	<i>T_p</i> [°C]	<i>P_p</i> [bar]	<i>SEM</i> <i>D_m</i> [μm]	<i>DLS</i> <i>D_m</i> [μm]
PEG_00		20	50	1.8	-	-
PEG_01	PEG (MW: 6000)	20	5	0.7	-	1 (±0.22)
PEG_02		40	5	0.7	-	1.5 (±0.31)
PEG_03		60	5	0.7	-	1.21 (±0.31)
PEG_04		20	18	0.8	0.85 (±0.19)	1.95 (±0.34)
PEG_05		20	9	0.8	0.85 (±0.19)	2.33 (±0.27)
PEG_06	PEG (MW: 10000)	20	5	0.8	0.75 (±0.21)	2.52 (±0.19)
PEG_07		30	5	0.8	0.85 (±0.22)	2.71 (±0.22)
PEG_08		40	5	0.8	1.10 (±0.23)	2.65 (±0.23)
PEG_09		60	5	0.8-1	1.5 (±0.44)	3.32 (±0.21)

Spherical microparticles were obtained at all the concentrations and examples are shown in the SEM images reported in **Figure VIII.17**.

Chapter VIII

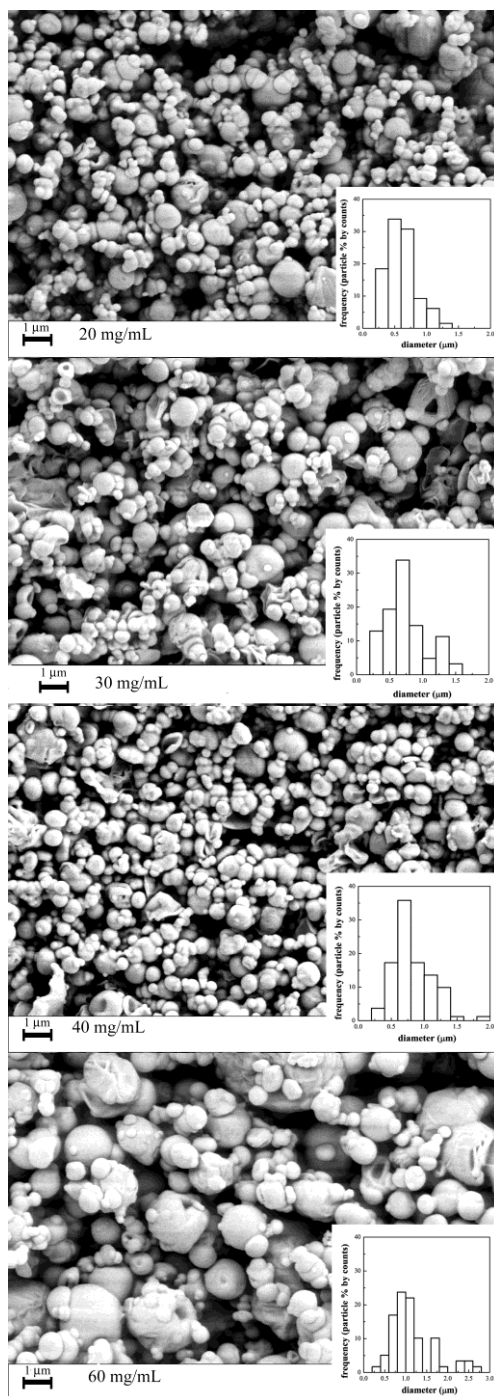


Figure VIII.17 SEM images showing the effect of solute concentration on the morphology and diameter of PEG10000 microparticles obtained by SAA

Validation of the SAA plant in the configuration operated at reduced pressure at 5°C and 0.8 bar, using (a) 20 mg/mL, (b) 30 mg/mL, (c) 40 mg/mL and (d) 60 mg/mL solute concentration. Histograms by count embedded.

The histograms of the particle size have been embedded in the corresponding images to get an immediate idea of the distributions as given by the photomicrographs. An increase of the particle size was qualitatively evident for the experiment performed at the highest polymer concentration (60 mg/mL).

DLS analysis revealed that the particle size distribution (PSDs), expressed in volumetric fraction (**Figure VIII.18**), were very narrow.

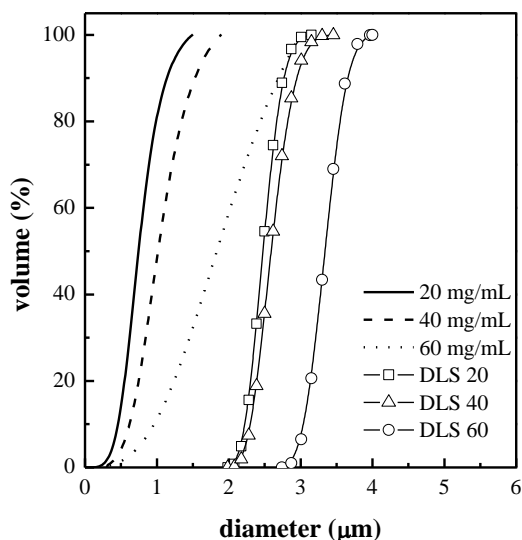


Figure VIII.18 Volumetric cumulative PSDs, obtained DLS, of PEG10000 microparticles obtained by SAA at 5 °C and 0.8 bar, different concentrations.

The particle size ranged between 2 and 3 µm when concentrations from 20 mg/mL to 40 mg/mL were selected; moreover, the tendency to produce large particles at 60 mg/mL was confirmed. However, SEM images, in **Figure VIII.17**, revealed the presence of particles smaller than those evidenced by DLS analysis; this difference can be due to the fact that, particles smaller than 1 µm, still showed the tendency to form aggregates.

Data related to particle mean diameters and standard deviations for these experiments are also summarized in **Table VIII.4**.

The increase of the particle size with the concentration is not linear, as well as the size distribution: the increase is small from 20 to 40 mg/mL and it is relatively larger at 60 mg/mL. As explained in previous SAA papers

Chapter VIII

(Reverchon et al., 2007b) an increase of solute concentration produces an increase of the viscosity of the starting solution, that in turn, decreases atomization efficiency since viscosity is a cohesive force for the liquid jet. The concentration of 60 mg/mL is also an operating limit for SAA processing of PEG10000, since during this test, the pressure in the precipitator raised to about 1 bar, due to the solvent condensation on the filter. Indeed, a no negligible boiling-point increase took place when this solute concentration was used.

Effect of precipitation temperature.

The effect of precipitation temperatures on PEG microparticles morphology and particle size distribution was also investigated. The operating conditions used for the following experiments were the same mentioned above (see also the legend of **Table VIII.4**), keeping constant the precipitation pressure at 0.8 bar and varying the precipitation temperature from 5°C to 18°C.

SEM photomicrographs, with the PS histograms embedded (**Figure VIII.19**), show that PEG particles, obtained at 5 and 9°C, do not present agglomeration; whereas, those produced at 18°C tend to coalesce.

Validation of the SAA plant in the configuration operated at reduced pressure

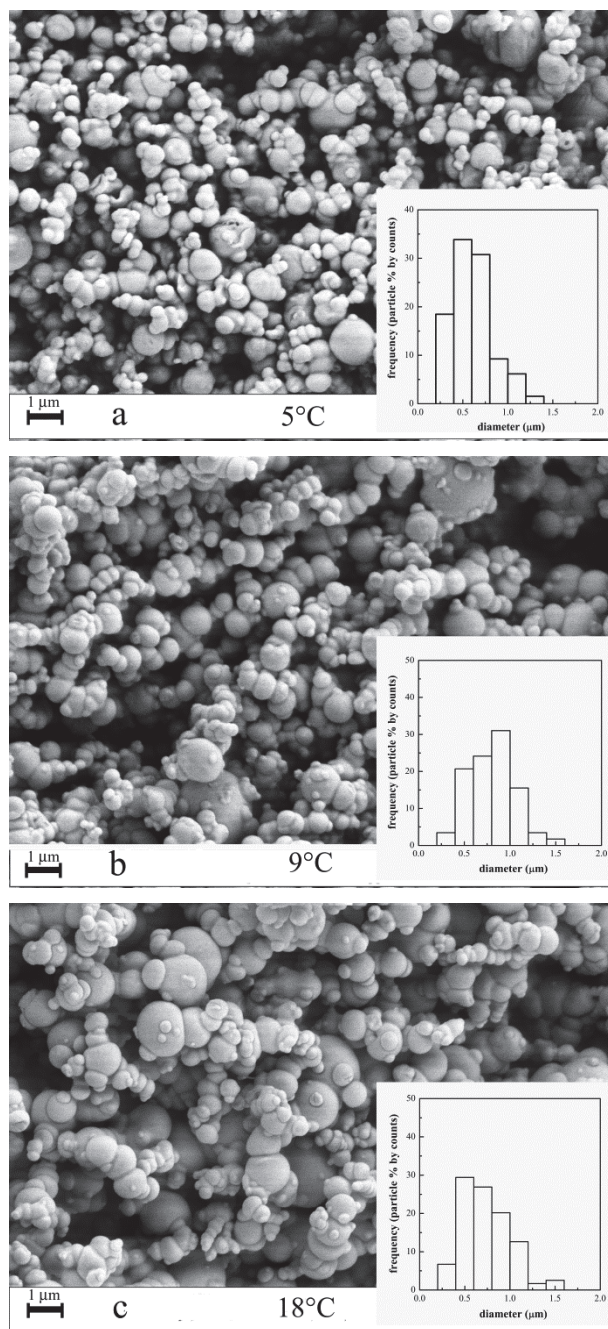


Figure VIII.19 SEM images showing the effect of precipitation temperature on morphology and diameter of PEG10000 microparticles obtained by SAA at 0.8 bar, 20 mg/mL solute concentration and precipitation temperature: (a) 5°C, (b) 9°C and (c) 18°C. Histograms by count embedded.

This result is probably due to the partial softening of the particles at the highest temperature tested, that is the problem found by the other authors in the literature and was discussed in the introduction. The presence of agglomerated particles was also revealed by DLS data analysis; indeed, despite the reduction of the mean diameter (see **Figure VIII.20**), the particles obtained operating at 18°C show the largest standard deviation (see **Table VIII.4**).

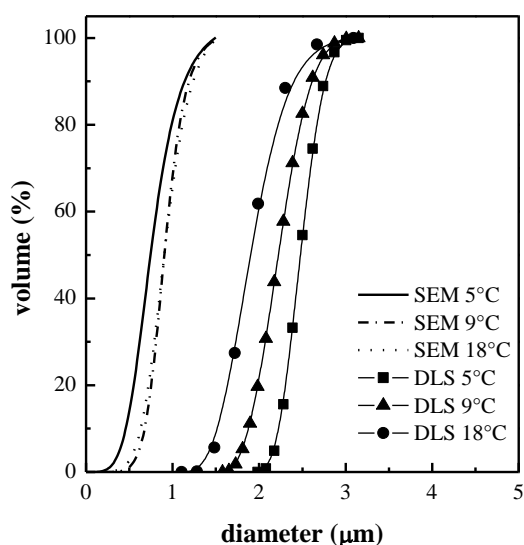


Figure VIII.20 Volumetric cumulative PSDs, obtained by DLS, of PEG10000 powders obtained by SAA at 0.8 bar, 20 mg/mL solute concentration, operating at different precipitation temperatures.

The two analytical techniques used to study the particle size distribution are based on different principles, this may cause variations in the results (Reverchon et al., 2007b). SEM analysis gives the information related to the size of the single particles; nevertheless, DLS analysis is affected by the presence of aggregates that, in the case of particles produced at 18°C is more pronounced.

In the case of our experiments, two opposite effects influence the particle size of precipitates: the reduction of the viscosity and surface tension of the liquid solution, due to the increasing of temperature at the exit of the injector, induce the formation of smaller droplets (Adami et al., 2011); but, particles softening also starts to produce aggregation.

Validation of the SAA plant in the configuration operated at reduced pressure

Solid state

The solid state of PEG particles produced by SAA was investigated by XRPD (**Figure VIII.21**) and DSC (**Figure VIII.22**).

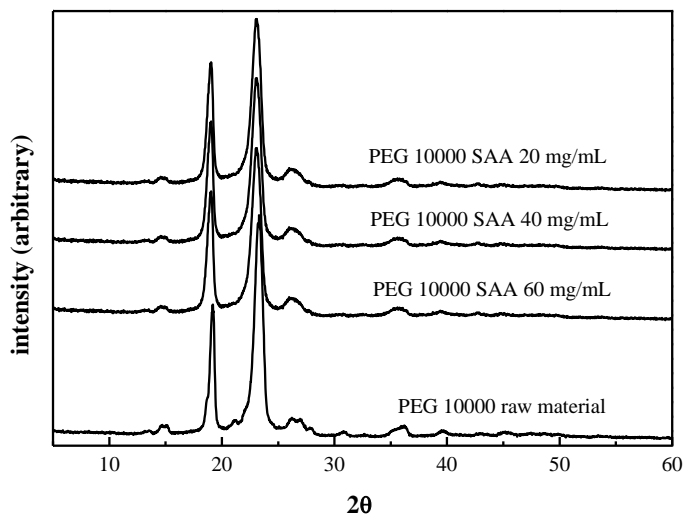


Figure VIII.21 XRPD of PEG10000 untreated and microparticles produced by SAA at 5°C and 20 mg/mL concentration.

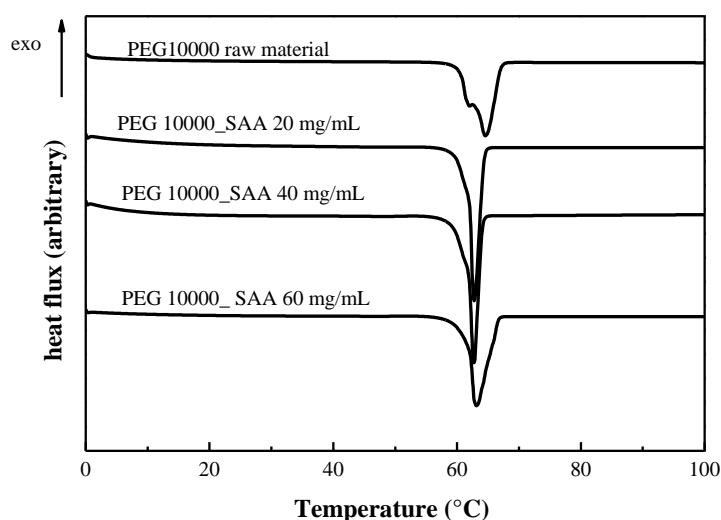


Figure VIII.22 DSC thermograms of PEG10000 untreated and PEG10000 microparticles produced by SAA at different solute concentration. Analyses performed with heating rate of 5°C/min.

XRPD spectra showed that the particles maintained the crystalline structure of the no processed material. This fact is relatively unusual in SAA processing; as a rule, SAA processed materials are amorphous (Cai et al., 2008, Reverchon and Antonacci, 2007) due to the very fast drying process; only in some cases, crystalline particles have been observed (Reverchon et al., 2010a) and this phenomenon has been explained by the very fast crystallization rate of small molecules. In this case, a polymer is involved; nevertheless, the possible explanation is the same: the crystallization rate is higher than the evaporation rate; therefore, the molecules can organize their structure before the drying process is completed, but, maintained the spherical shape, descending from the liquid droplets. DSC analysis (**Figure VIII.22**) confirmed that processed PEG is crystalline: a sharp endothermic peak is present at about 63°C, and it is attributable to the melting of the polymer. Moreover, considering the heat of fusion (ΔH_m) of the samples obtained by SAA ($\Delta H_{m(20\text{mg/mL})}=62.76\pm 0.18$ J/g, $\Delta H_{m(40\text{mg/mL})}=62.79\pm 0.18$ J/g, $\Delta H_{m(60\text{mg/mL})}=63.10\pm 0.18$ J/g) and the one of the raw material ($\Delta H_{m(\text{raw})}=64.5\pm 0.18$ J/g), it is possible to notice that the values are comparable. This confirms that SAA process did not affect the crystalline structure of the particles

Validation of the SAA plant in the configuration operated at reduced pressure

Discussion

SAA plant in the vacuum configuration was successfully used for the production of PEG microparticles. The experimental evidence confirms that, increasing the concentration of solute, the structure of the obtained particles becomes more fragile, because the supersaturation phenomenon takes place more quickly than the evaporation process. However, these tests demonstrate that the processability of compounds with a very low glass transition temperature is possible using the SAA process in the new configuration. The success of this experimentation is due to the low temperature reached in the precipitation vessel, improved by the use of CO₂ as atomization medium. Indeed, the evaporation of the dissolved CO₂ allows the lowering of the temperature downstream the injector and to operate at 5°C in the precipitator, while the presence of nitrogen keeps constant the set temperature.

VIII.2.4. Copolymers PLA-PEG

Different PLA-PEG copolymers, characterized by various architectures (linear L, branched G1, branched G2), different length and tacticity (atactic or isotactic) of the polylactide arms have been synthesized. The synthesis was achieved performing controlled ring-opening polymerization (ROP) of L or D,L-lactides on a multifunctional initiator core made of polyethyleneglycol monomethyl ether (m-PEG, Mn = 2000 Da, Mw/Mn = 1.04) in the presence of Al(CH₃)₃ (**Figure VIII.1**) (Izzo and Pappalardo, 2010)

Table VIII.5 Composition, molecular weight and architecture of the copolymers used for SAA process.

<i>architecture</i>	<i>PEG/PLA (w/w)</i>	<i>Mn^a (kDa)</i>	<i>mol_{L-LA} (%)</i>	<i>Mw/Mn^b</i>	<i>Unit per block of PLA</i>
L	1/4	7.7	47	1.17	40
G1	1/4	10.7	57	1.18	30
G2	1/4	9.7	55	1.29	13
L	1/8	18.1	70	1.20	125
G1	1/8	17.5	70	1.38	64
G2	1/8	23.1	73	1.51	27

Mn:molar mass; Mw:molecular weight

^aEvaluated by ¹H NMR

^bEvaluated by GPC

^cCalculated using equation: [Mn(copolymer)-Mn(PEG)]/(144-n-PLLA blocks)

This process allowed the preparation of samples with well-defined architectures. The control of the parameters, such as number and size of the branching, stereoregularity of PLA arms and polydispersity, is mandatory, as they strongly influence the crystallinity of the materials, and their thermal and rheological properties. Copolymers with relative content of PEG:PLA of

Chapter VIII

1:4 and 1:8 (w/w) were prepared for each architecture (I, G1 and G2), with atactic and isotactic polylactide arms.

To perform SAA experiments, we selected chloroform, since the solubility of PEG–PLA copolymer is high in this solvent. A concentration of polymer of 20 mg/mL was used and the operative conditions were chosen on the basis of the previous SAA papers related to polymer microparticle production (Adami et al., 2011).

In this specific work, according to the previous considerations, a Gas to Liquid Ratio on mass basis (GLR) of 1.8 was used, corresponding to a CO₂ molar fraction of 0.83, using a CO₂ flow rate of 9 g/min and the operating conditions of temperature and pressure in the saturator were chosen as 80°C and 90 bar. Working at these specific conditions, the operating point of SAA processing is located in the two phase region of the high pressure vapour–liquid equilibrium diagram for the system chloroform–CO₂ (Peters and Florusse, 1995). In this case, the part of CO₂ not dissolved in the expanded liquid, will operate as a pneumatic agent that can further improve the atomization process. The possible influence of solute on the thermodynamics of the high-pressure fluid phase system has been neglected.

The first experiments on PEG–PLA copolymer were performed using the SAA configuration with the precipitation at atmospheric pressure, using a precipitation temperature of 60°C and a flow rate of 1380 L/h of heated N₂. The results were not satisfactory, since the material softened in the precipitator: the temperature used for evaporating the solvent during precipitation was too high for these copolymers and induced particle coalescence. This result depends on the glass transition temperature (T_g) of the material; atactic PLA based copolymers were characterized by $T_g < 45^\circ\text{C}$; whereas T_g of isotactic PLA based copolymers were not detected; however, it is reasonable to hypothesize that they are lower than 57°C, that is the T_g of isotactic PLA homopolymer (Vanhoorne et al., 1992). Therefore, verified that standard SAA was unsuccessful in processing these materials, in the following of this work, SAA in the vacuum configuration was used, in which the vacuum system allows to use reduced pressures and, correspondingly, lower evaporation temperatures in the precipitator.

In all the following experiments, 40°C was the temperature set in the precipitator and a reduced pressure of about 0.65 bar was used. A flow rate of 686 L/h of heated N₂ was used to allow solvent evaporation. The polymer concentration in chloroform was maintained at 20 mg/mL and the GLR at 1.8. At these process parameters, the copolymers containing atactic PLA blocks were not efficiently processed because of the low T_g values with respect to the process temperature. On the contrary, copolymers having isotactic PLA blocks were processed, obtaining different results depending on the architectures used.

Validation of the SAA plant in the configuration operated at reduced pressure

1:4 copolymer processing

Particles obtained by processing the 1:4 (PEG:PLA) copolymers are shown in **Figure VIII.23**.

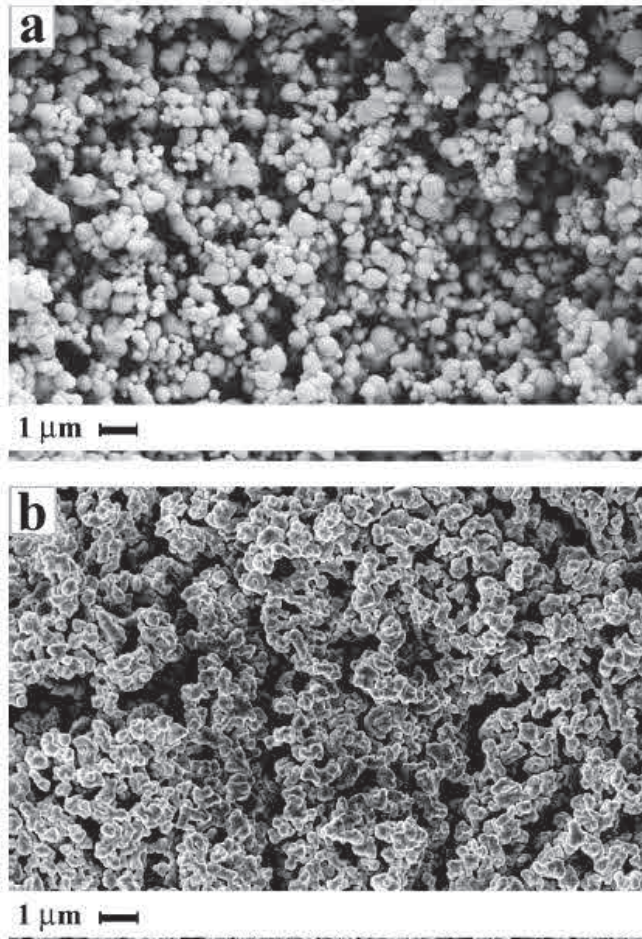


Figure VIII.23 SEM photomicrographs of 1:4 (PEG:PLA) SAA precipitated microparticles. (a) l, (b) G1 branched copolymer (magnification 20Kx).

SEM photomicrographs show that the l copolymer produced well defined particles with a spherical morphology. In **Figure VIII.24** SEM photomicrograph with a higher magnification is reported, in which microparticle morphology is more clearly shown.

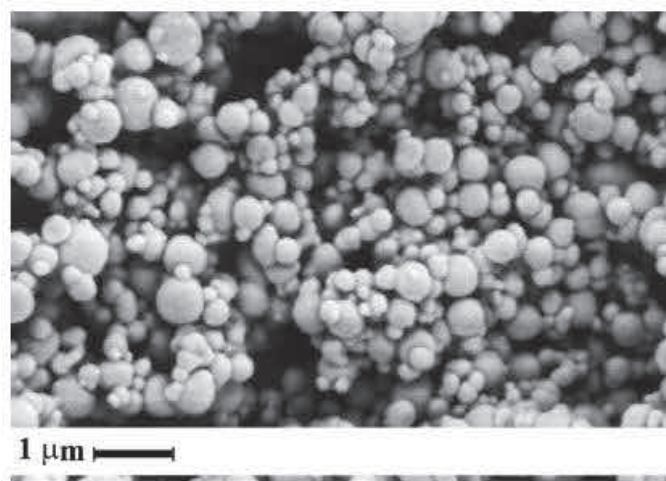


Figure VIII.24 SEM photomicrograph of 1:4 (PEG:PLA) microparticles of *l* copolymer (magnification 40Kx).

On the contrary, in the case of the branched copolymer of first generation (G1), it was not possible to obtain particles with a well-defined structure, since massive agglomeration of the particles took place. This phenomenon is evident in the SEM photomicrograph reported in **Figure VIII.23b**, where an example of G1 SAA precipitated particles is reported. In the case of the second generation copolymer (G2) no particles were recovered, but a continuous film was formed in the precipitation vessel. This phenomenon has also been observed in other cases in SAA processing (Reverchon and Antonacci, 2007)

Table VIII.6 Results of selected experiments performed using SAA.

PEG:PLA	structure	Particle morphology
1:4	<i>l</i>	Spherical
1:4	G1	Connected
1:4	G2	Film
1:8	<i>l</i>	Spherical
1:8	G1	Connected
1:8	G1	Spherical

1:8 copolymer processing

SAA micronization of copolymers 1:8 (PEG–PLA) was, then, performed. In this case spherical microparticles were obtained for *l* and G2 copolymers; whereas, connected particles for the G1 architecture were again observed (**Table VIII.6**). Examples of these precipitates are shown in **Figure VIII.25**, where SEM photomicrographs taken at the same enlargement are reported.

Validation of the SAA plant in the configuration operated at reduced pressure

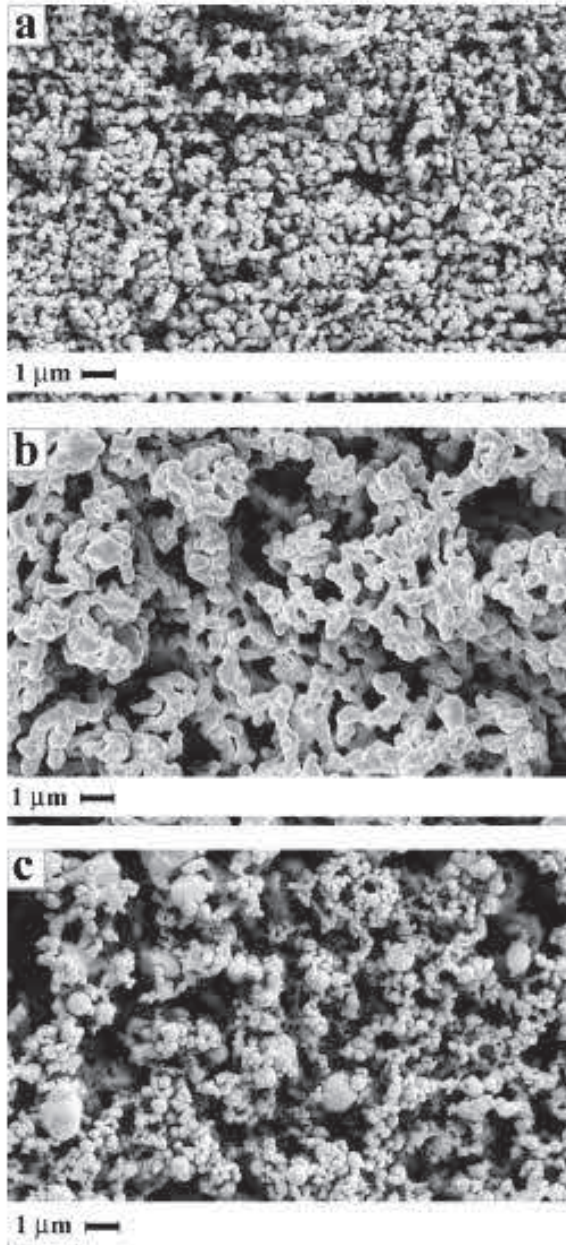


Figure VIII.25 SEM photomicrographs of 1:8 (PEG:PLA) microparticles. (a) I, (b) G1 and (c) G2 copolymer (magnification 20Kx).

Comparing these results to the 1:4 copolymers, G1 1:8 copolymer micronization was again unsuccessful, because of particle coalescence;

whereas, 1:8 G2 copolymer was obtained as no coalescing microparticles (**Figure VIII.25c**).

In fact, SAA micronization of PEG–PLA copolymers was successful in three cases; the obtained particles showed always a mean diameter smaller than 1 μm (see **Table VIII.7**)

Table VIII.7 PS and PSD of PEG–PLA copolymer particles obtained by SAA.

PEG:PLA	structure	Mean diameter [μm]
1:4	<i>l</i>	0.24 (± 0.09)
1:8	<i>l</i>	0.44 (± 0.18)
1:8	G2	0.28 (± 0.07)

Moreover, the mean diameter of the particles PEG–PLA 1:8 of the branched copolymer was smaller than the one of the corresponding linear one. These results are also shown in **Figure VIII.26**, where the PSDs in terms of volumetric cumulative percentages are reported. As it may be expected, the particles obtained for the linear copolymer with a PEG:PLA ratio of 1:4 are smaller than the particles obtained using the linear copolymer with a PEG:PLA ratio of 1:8 because of the lower molecular weight. Their standard deviation is smaller too. Furthermore, by comparison of samples having the same PEG:PLA ratio (1:8), but a different structure (linear vs G2, see **Table VIII.7**), it can be concluded that the particle size of precipitates also depends on the architecture of the copolymer, with the G2 copolymer producing smaller particles with a lower SD. Longer polymeric chains could organize themselves in larger entanglements compared to the branched chain; this produces a more compact steric arrangement, that can influence the precipitation behavior.

Validation of the SAA plant in the configuration operated at reduced pressure

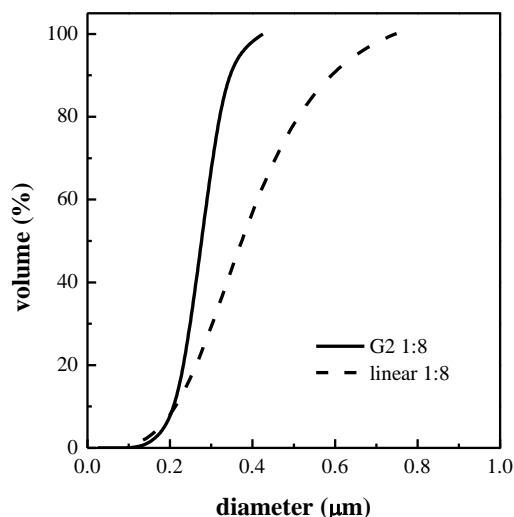


Figure VIII.26 PSD of 1:8 PEG–PLA copolymer particles obtained by SAA. Calculations were performed in terms of volumetric cumulative percentages from SEM images.

The role of molecular weight has been probably decisive for the success of the micronization in the case of G2 branched copolymer with PEG–PLA ratio 1:8, because it has a higher molecular weight when compared to the copolymer 1:4.

When PEG–PLA copolymer particles were suspended in water, to simulate a pharmaceutical formulation, larger particles were detected by DLS with respect to the measurements performed on the starting powder. The particles formed during DLS analysis (**Table VIII.8**) showed a mean diameter increase of about 0.2 μm with respect to SEM image measurements, whereas, the standard deviation decreased from about 2 to about 5 times with respect to SEM related data.

Table VIII.8 PSD of PEG–PLA copolymer particles obtained by SAA, suspended in water and measured by DLS.

PEG:PLA	structure	Mean diameter [μm]
1:4	<i>l</i>	0.40 (± 0.03)
1:8	<i>l</i>	0.60 (± 0.03)
1:8	G2	0.46 (± 0.03)

These results cannot be explained by the use of different measurement systems; but, they could depend on the salvation of PEG blocks, that produced the swelling of the particles and the corresponding increase of their

mean diameter. The narrowing of the standard deviation (SD) might be explained by the achievement of a solvation equilibrium of the suspended microparticles, similar to the one of micellar systems (Vila et al., 2004a, Heald et al., 2002, Riley et al., 2003).

In the case of the branched copolymers of first generation (G1) it was not possible to obtain particles with a defined structure, since agglomeration of the particles took place. This problem can be due to the nature of the polymeric structure; indeed, G1 copolymers have a “Y” shape and display a higher hydrodynamic volume than the linear ones (Izzo and Pappalardo, 2010). As a consequence, larger amount of water could be absorbed and remain in the droplets when SAA precipitation occurred, inducing the partial coalescence of the particles on the filter. It might be possible that inter-chain hydrogen bonds, due to the absorbed water, are responsible of the formation of physical bridges among the particles.

To better understand the effect of the SAA processing on the studied copolymers, the samples were characterized through ^1H NMR and GPC before and after the micronization. ^1H NMR showed that there were no chemical modifications in the processed copolymers (**Table VIII.9**).

Table VIII.9 Comparison between copolymers untreated (*u*) and after micronization (*m*): molecular mass, percentage in mole of lactide in the copolymer, polydispersity index, melting point and melting enthalpy. (T_f : melting temperature; ΔH_f : enthalpy of fusion)

PEG:PLA (w/w)	Mn (kDa)		mol _{L-LA}		Mw/Mn		T _f (°C)		ΔH _f (J/g)	
	u	m	u	m	u	m	u	m	u	m
1 (1/4)	7.7	8.7	47	50	1.17	1.27	151	152	36	59
G1 (1/4)	10.7	10.2	57	56	1.18	n.d.	161	161	56	56
G2 (1/4)	9.7	-	55	-	1.29	-	155	-	50	-
1 (1/8)	18.1	17.0	70	69	1.20	1.18	154	154	46	48
G1 (1/8)	17.5	20.7	70	71	1.38	1.38	166	166	63	64
G2 (1/8)	23.1	19.3	73	77	1.51	1.43	161	161	48	56

Indeed, no shift of the peaks were registered and the relative intensity of the characteristic groups (metilic for PLA $\delta = 5.17$; and metilenic for PEG $\delta = 3.64$) were not modified for all the samples. Analogously, the low polydispersity index and the molecular weight of the samples, determined by GPC analysis and ^1H NMR respectively, revealed that SAA process did not induce any change in the polymer structure.

The untreated copolymers were semicrystalline, with a higher degree of crystallinity of the branched copolymer compared to that of the linear one (Di Lorenzo et al., 2011), XRPD spectra in **Figure VIII.27** show for the untreated copolymers the characteristic peaks of PLA, detected at $2\theta = 16.6$

Validation of the SAA plant in the configuration operated at reduced pressure and $2\theta = 19$, with the first peak of higher intensity compared to the second one.

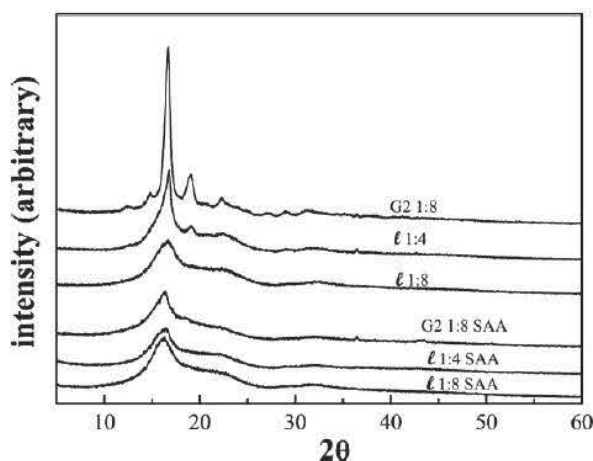


Figure VIII.27 DSC analyses of PEG–PLA microparticles: *l* linear 1:4, *l* linear 1:8, G2 branched 1:4.

Processed copolymers show the characteristic halo of the amorphous structures. SAA processing induces the formation of structures with a lower degree of crystallinity compared to the unprocessed material as a consequence of the faster rate of precipitation compared to the traditional crystallization (Cai et al., 2008).

Characterization: composition

All the samples were characterized through H NMR and GPC in order to verify if SAA process changed the chemical structure of the polymer.

Figure 33 shows that the process did not modify the polymeric structure of linear copolymer and the branched copolymer G1, since no shift of the peaks were registered and the relative intensity of the characteristic group (metinic for PLA $\delta= 5.17$; and metilenic for PEG $\delta=3.64$) were the same for both samples. Whereas an increase of lactide percentage were registered after the process of the branched copolymer G2.

Chapter VIII

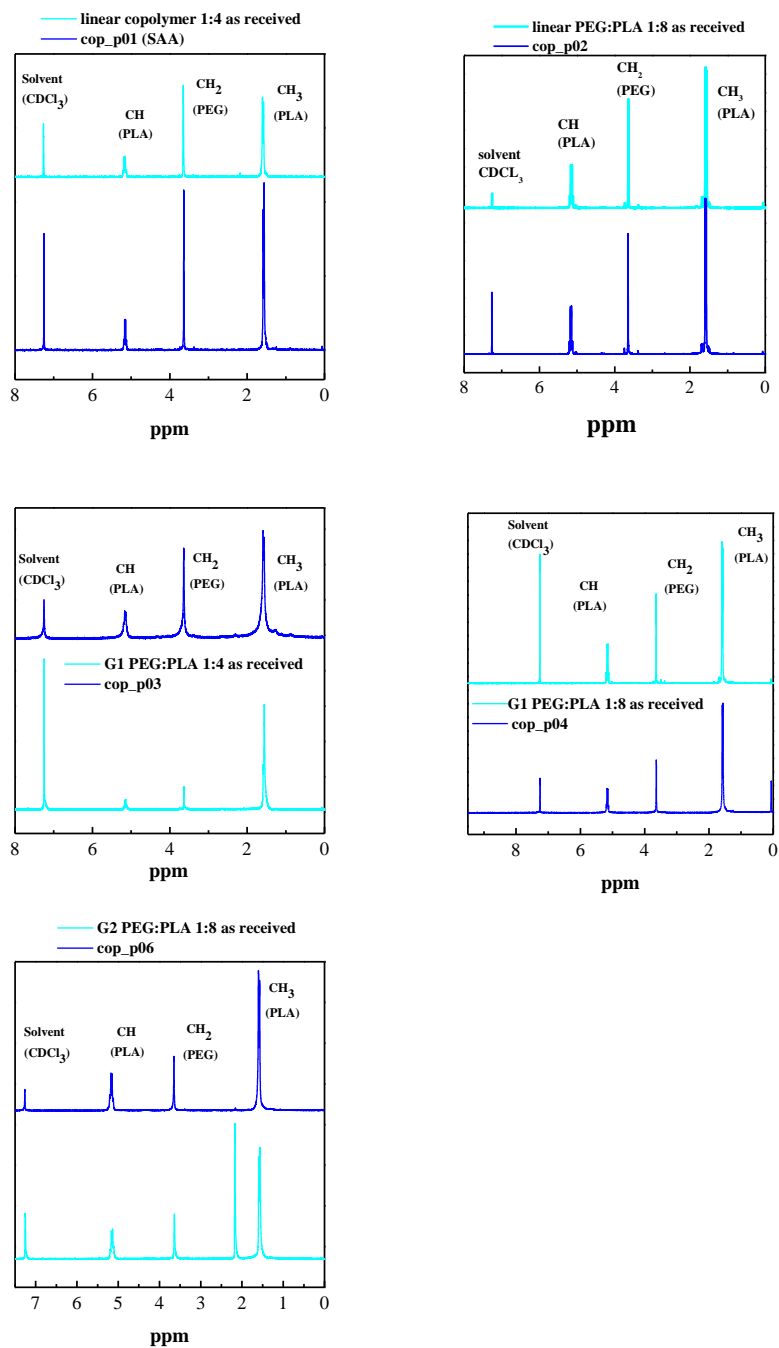


Figure VIII.28 Comparison between ¹H NMR (CDCl₃, 5°C) spectra related to the copolymer as received and the processed polymer.

Validation of the SAA plant in the configuration operated at reduced pressure

Using the same technique it is possible to calculate the molecular mass of the copolymer:

Table VIII.10 *H NMR analysis of the molecular mass and lactide percentage of the linear copolymer as received and after SAA process.*

	<i>Mn [kDa]</i>	<i>mol % LA</i>
Linear 1:4	7.7	47
cop_p01	8.7	50
Linear 1:8	18.1	70
cop_p02	17.0	69
G1 1:8	17.5	70
cop_p04	20.7	71
G2 1:8	23.1	730
cop_p06	19.3	77

Table VIII.10 demonstrates that no significant variations in molecular structure of the copolymer took place during SAA process when linear copolymer was used as solute.

Gel Permeation Chromatography (GPC) was used to evaluate the polydispersity of the molecular weight in the copolymer.

Table VIII.11 *Evaluation of polydispersity index obtained using GPC. Comparison between copolymer as received and processed copolymer.*

	PDI
Linear 1:4	1.17
cop_p01	1.27
Linear 1:8	1.20
cop_p02	1.18
G1 1:8	1.38
cop_p04	1.38
G2 1:8	1.51
cop_p06	1.43

The low polydispersity index registered by GPC analysis reveals that no secondary reaction took place during polymerisation reactions and that during SAA process the molecular structure did not change.

Discussion

SAA in the new reduced pressure configuration has been successfully used to process polymers with low glass transition temperatures like PEG–PLA copolymers. The experimental evidences demonstrate that the parameters that influence the particle size distribution are the molecular weight of the copolymer, the total amount of lactide arms and stereoregularity of lactide chains. Indeed, linear structures and higher length of lactide branches induce the formation of larger particles, as well as the higher molecular weight, represented by lower PEG:PLA ratio. Moreover, water absorption can influence the morphology of the particles, since it can induce the formation of micellar structures. The most promising copolymer structure seems to be the G2 branched 1:8 PEG–PLA, that represents a good compromise between size of the particles and architecture. In conclusion, modulation of the PEG–PLA ratio and of the architecture of the copolymers, in combination with the new reduced pressure configuration of SAA, represent a very promising approach to the preparation of micronized particles for an engineered control of drug release.

VIII.2.5. Coprecipitates: PEG- α Tocopherol acetate

The tests on the system PEG- α Tocopherol (α -TCP) acetate were performed at the same operating conditions used for PEG 10000, since this is the polymer chosen for α -TCP encapsulation.

Table VIII.12 Selected experiments performed using SAA equipped with the vacuum system. (T_p : precipitation temperature; p_p : precipitation pressure; T_m : saturator temperature; p_m : saturator pressure; c : solute concentration; GLR: gas to liquid ratio; Q_{CO_2} : CO_2 flow rate; Q_{LIQ} : solvent flow rate; Q_{N_2} : N_2 flow rate).

n. test	solute	solvent	c mg/mL	GLR w_{CO_2}/w_{liq}	T_p °C	p_p bar	Q_{CO_2} [gr/min]	Q_{LIQ} [mL/min]	Q_{N_2} [L/h]	T_m °C	p_m bar
α TCP_p01	PEG 5% α TCP	C_2H_6CO	20	3.5	20	0.82	11.22	3.5	686	40	67
α TCP_p02	PEG 10% α TCP	C_2H_6CO	20	3.5	23	0.8	12.52	3.76	686	40	68
α TCP_p03	PEG 20% α TCP	C_2H_6CO	20	3.5	24	2	13.71	4.28	686	40	70

Validation of the SAA plant in the configuration operated at reduced pressure

We report the test performed on PEG (Mw 10000), that we discussed in the section 5.3:

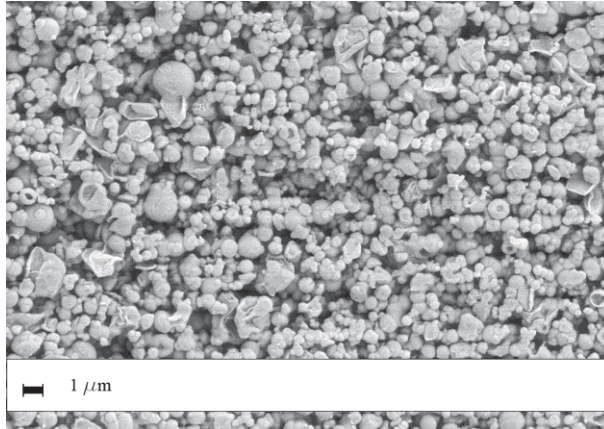


Figure VIII.29 PEG microparticles obtained by SAA, at 20°C and 0.8 bar in the precipitator; 40°C and 67 bar in the saturator.

Other experiments were performed adding α -TCP in the solution of PEG and acetone fed to the saturator.

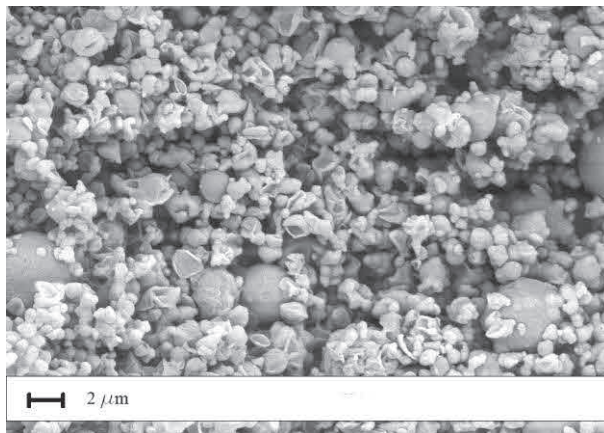


Figure VIII.30 PEG loaded 5% (w/w) of α -TCP. Microparticles obtained by SAA at 20°C and 0.82 bar in the precipitator; 40°C and 67 bar in the saturator (see **Table VIII.12**).

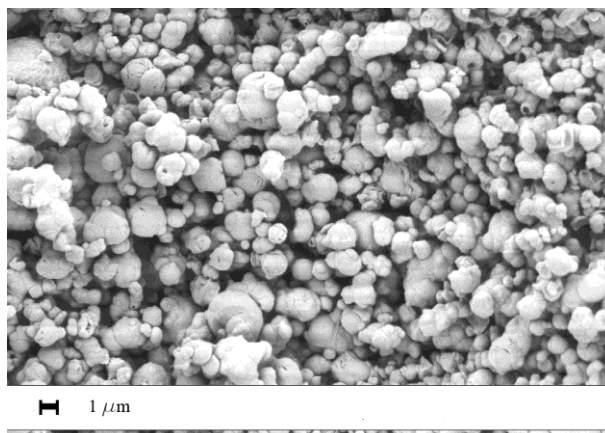


Figure VIII.31 PEG loaded 10% (w) of α -TCP microparticles obtained by SAA at 23°C and 0.8 bar in the precipitator; 40°C and 68 bar in the saturator (see **Table VIII.12**).

SEM photomicrographs (**Figure VIII.29** and **Figure VIII.30**) shows that adding a higher percentage of α -TCP it is possible to obtain more free flowing particles with well-defined morphology. This phenomenon is due to the stabilizing effect of α -TCP in polymeric matrix (Teo et al., 2010). **Figure VIII.32** shows the particle size distribution of the produced powder.

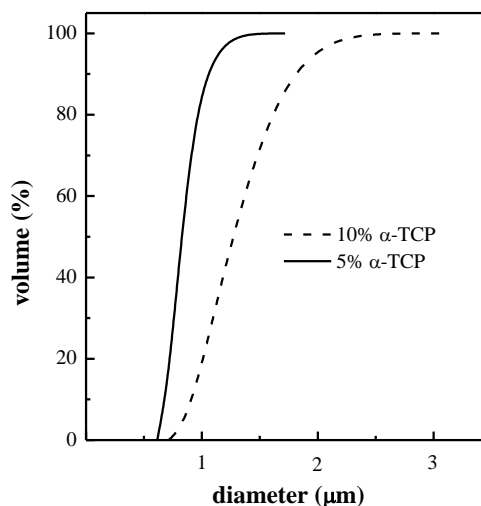


Figure VIII.32 Cumulative volumetric particle size distribution of the particles produced using SAA. Comparison between the particles loaded with different percentage of α -TCP.

Validation of the SAA plant in the configuration operated at reduced pressure

The particles have a mean diameter ranged between 0.8 and 1.3 μm . The presence of a larger percentage of α -TCP induced an increasing of particle dimensions (Teo et al., 2010).

XRPD and DSC analysis gave some information about the solid state of the produced particles.

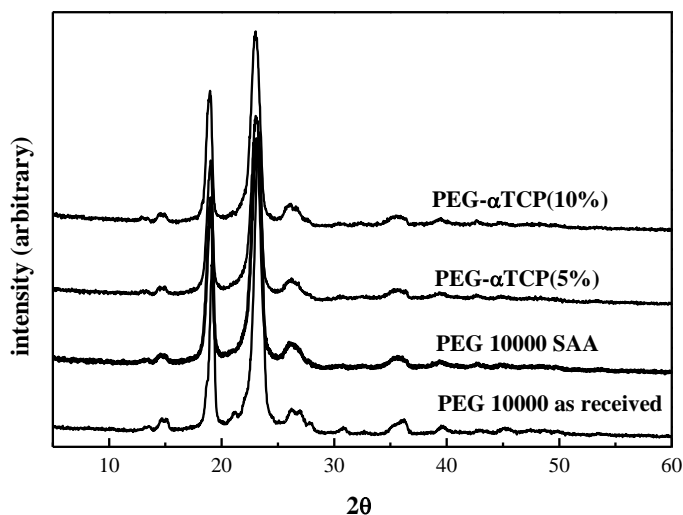


Figure VIII.33 XRPD of untreated raw material and SAA produced PEG- α TCP microparticles at different α TCP percentage in liquid feed. See Table 12.

Figure VIII.33 reports a XRPD comparison between the unprocessed material and the microparticles obtained by SAA: the process allows the formation of crystalline microparticles as in the case of PEG 6000. This experimental evidence was confirmed by DSC analysis.

The thermogram, **Figure VIII.34**, related to the unprocessed PEG shows the double melting behavior of the polymer as received, due to the presence of imperfect crystals that melt at different temperatures (Delahaye et al., 1997). The thermograms related to the particles produced by SAA had only the peak at 62°C, corresponding to the more stable crystal structure formation.

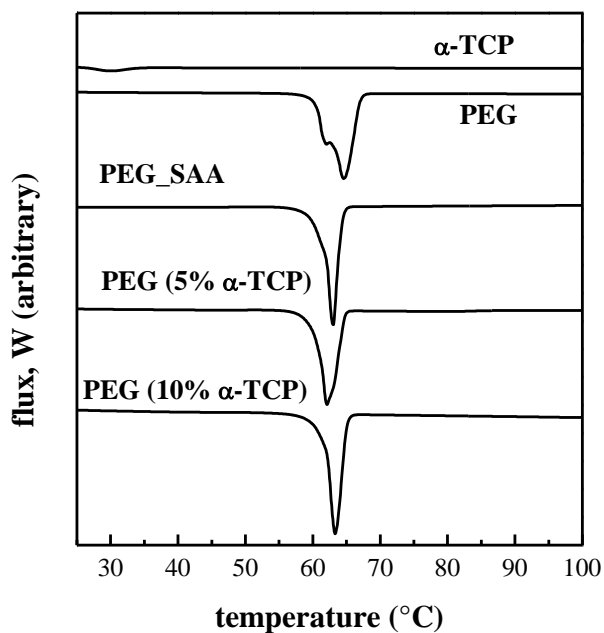


Figure VIII.34 Thermograms: comparison among the analysis performed on the powder produced by SAA and the raw materials, PEG and α -TCP untreated.

The analysis performed using HPLC revealed that the measured loading was close to theoretical one.

Finally the stability to hydrolysis of the vitamin in water medium was investigated using HPLC (**Table VIII.13**). The vitamin retained at least 67% of its stability when loaded in PEG matrix.

Validation of the SAA plant in the configuration operated at reduced pressure

Table VIII.13 *Stability to hydrolysis, in water medium, of the vitamin in SAA formulation. The percentage was related to the content of vitamin loaded in polymer matrix.*

<i>Time, min</i>	<i>Stability %</i>
8	81.56
9	78.26
10	67.54
70	67.48
1 day	67.50

Discussion

The SAA process was successfully performed for the micronization of PEG and α -TCP loaded with PEG. The obtained particles had a regular morphology and vitamin preserved its stability when dissolved in water medium. The presence of vitamin in the polymeric matrix allows the formation of free flowing particles and no agglomerated structure were obtained.

VIII.2.6. Effect of polymer architecture and molecular weight

Results obtained on polymer micronization demonstrated that polymer architecture and molecular weight have a strong influence on the mean dimension of SAA products.

SAA micronization experiments were performed on PLLA at different molecular weight, 120000 and 28000 Da, in the same operative conditions and very different results were obtained, as shown in **Figure VIII.35**.

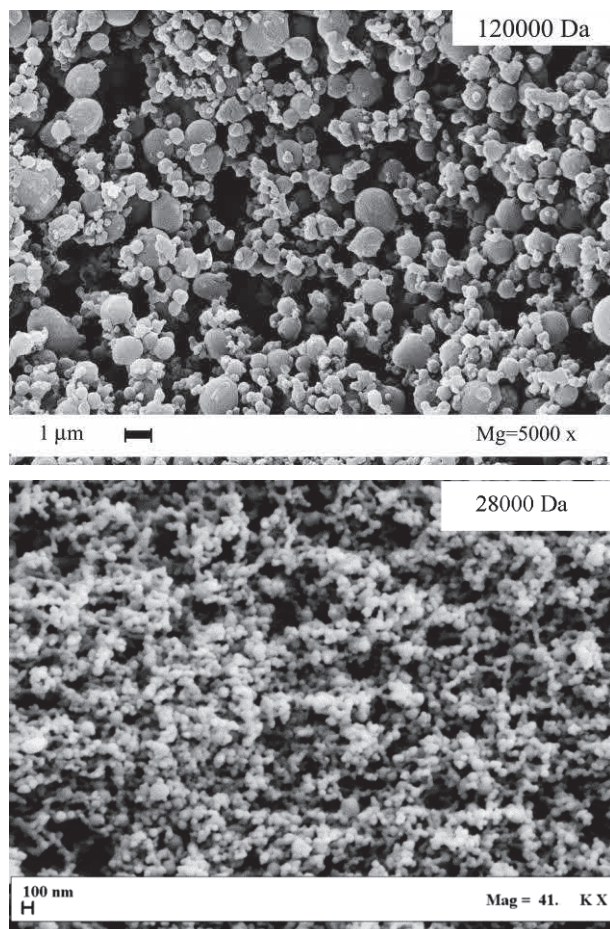


Figure VIII.35 PLLA 120000 Da and PLLA 28000 Da, microparticles obtained by SAA at 40°C in the precipitator. The concentration of the solution is 20 mg/mL

Particle Size Distribution, evaluated from SEM photomicrograph analysis, reveals that nanometric particles were obtained when PLLA 28000 was used, as shown in **Figure VIII.36**.

Validation of the SAA plant in the configuration operated at reduced pressure

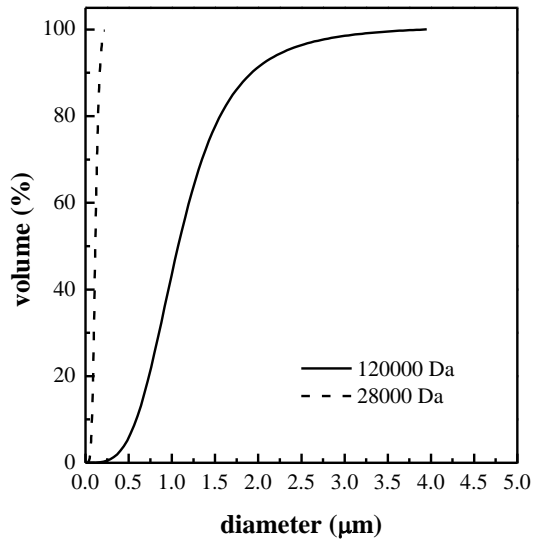


Figure VIII.36 Volumetric cumulative particle size distribution of PLLA microparticles produced by SAA.

Mean particle size of PLLA28000 microparticles is of about $0.11 (\pm 0.06)$ μm , therefore, it is possible to say that nanoparticles of this material can be produced by SAA. Probably this result is due to the different viscosity of this polymer in the solution that is fed to the saturator. High molecular weight polymers induce an increase in solution viscosity that allows the formation of bigger particles (Legrand et al., 2007).

It is also interesting to analyze the effect of polymer chain architecture on mean particle size. This effect is shown in **Figure VIII.37**, in which SEM photomicrographs of microparticles of ramified and linear copolymer PEG-PLA are reported.

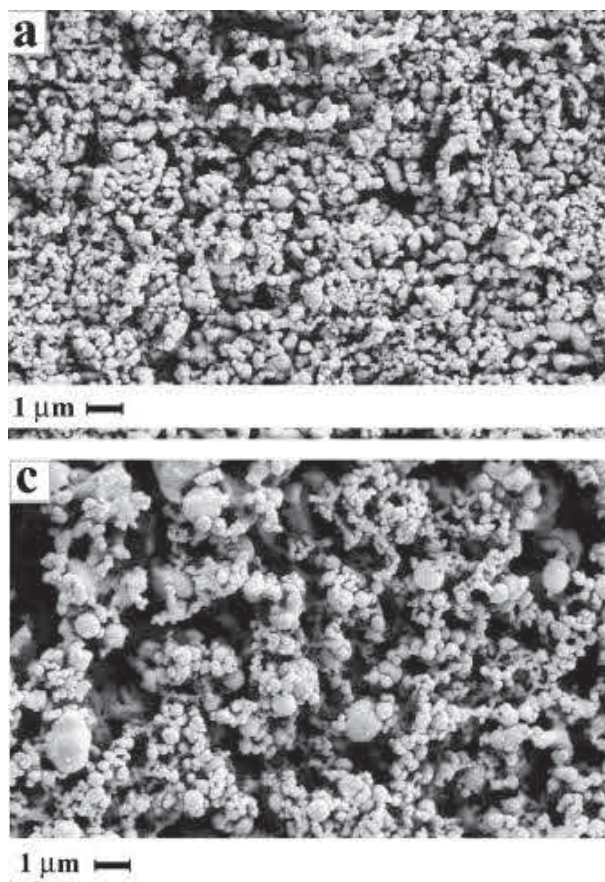


Figure VIII.37 PEG-PLA copolymer produced by SAA at 40°C and 0.65 bar in the precipitator; 80°C and 87 bar in the saturator. Ramified copolymer G2 (right); Linear copolymer (left).

Smaller particles were obtained when ramified copolymer was used, as shown in **Figure VIII.38**.

Validation of the SAA plant in the configuration operated at reduced pressure

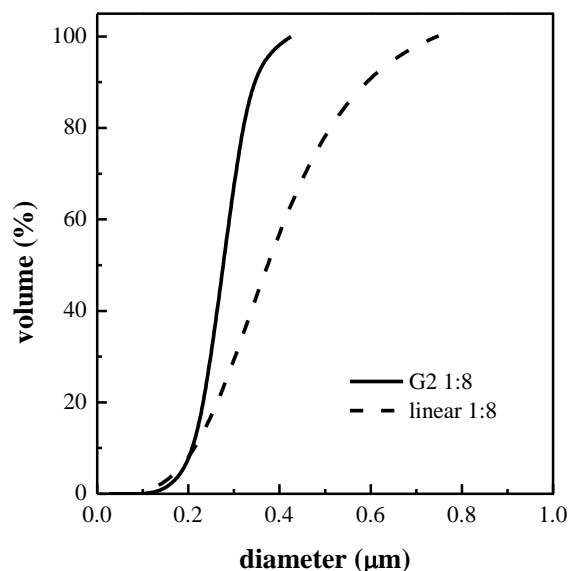


Figure VIII.38 Volumetric particle size distribution of microparticles of copolymer PLA-PEG obtained by SAA.

Ramification affects polymeric chain length, therefore ramified particles have shorter polymeric chains and their organization is more compact than the polymeric chain of linear polymer with the same molecular weight.

The obtained results, mentioned above, demonstrate that it is possible to obtain nanoparticles by SAA process. However this possibility depends on the structure of the compound to micronize, in the case of polymers.

VIII.3. Conclusions

All the tests performed demonstrated that it is possible to use SAA plant in the vacuum configuration even for polymers with very low glass transition temperature, such as PEG. In this case study, it was possible to verify that the molecular weight of the polymer has a great influence on particles stability and morphology, since polymer with lower molecular weight tends to form particles with more fragile structure.

In the tests performed on PEG-PLA copolymers the experimental evidences demonstrate that the parameters that influence the particle size distribution are the molecular weight of the copolymer, the total amount of lactide arms and stereoregularity of lactide chains. Indeed, linear structures and higher length of lactide branches induce the formation of larger particles, as well as the higher molecular weight, represented by lower

Chapter VIII

PEG:PLA ratio. Moreover, water absorption can influence the morphology of the particles, since it can induce the formation of micellar structures. The most promising copolymer structure seems to be the G2 branched 1:8 PEG-PLA, that represents a good compromise between size of the particles and architecture. In conclusion, modulation of the PEG-PLA ratio and of the architecture of the copolymers, in combination with the new reduced pressure configuration of SAA, represent a very promising approach to the preparation of micronized particles for an engineered control of drug release.

The SAA plant, in the vacuum configuration, can be used also for production of coprecipitates of thermolabile compounds: PEG and α -Tocopherol acetate. Good results in term of particle morphology were obtained when a higher amount of vitamin was fed.

The experiments performed using different polymers demonstrated that the solid state of the obtained particles depends on the precipitation temperature. Indeed, when this temperature is set at value lower than the crystallization one, the obtained particles are amorphous, as in the case of PLLA particles production, whereas if the temperature set in the precipitator is above the crystallization one, the obtained particles are crystalline, as in the case of PEG.

SAA technique, using the plant configuration with the vacuum system, is also promising for the production of nanoparticles. The tests performed on PEG-PLA copolymer demonstrated that sub-micro and nanoparticles can be produced by SAA.

Chapter IX

Conclusions

The first part of the thesis work, related to the studies on thermodynamic and atomization mechanisms, has given a significant contribution on the understanding of SAA micronization technique.

The second part of the thesis work successfully gave birth to a new configuration of SAA plant for the micronization of thermolabile compounds. The validation of the plant ensures the use of the technique for several kinds of compounds that could not be processed in the previous configuration.

Raman laser scattering based technique is an efficient method to detect the composition of the phases at equilibrium. The Raman detection has been efficiently validated, comparing data reported in literature on the system CO₂-water-acetone at 60°C and 100 bar, and can be used to detect the equilibria for the same system at 80°C and 90 bar, that are the operative conditions used for SAA experiments, such as VLE of more other operating conditions.

The study of the atomization process allowed to elucidate the role of supercritical CO₂ in the spray formation. CO₂ induces a decrease of viscosity and surface tension allowing an increase of jet breakup efficiency. CO₂, that is not solubilized in the solution, allows the formation of annular flow, in which the no dissolved gas reduces the section for the passage of the liquid, improving, again, the efficiency of jet breakup.

The new layout for the SAA plant proposed, constructed and validated, can be used for the production of thermolabile compounds and polymers with low glass transition temperature. Some examples are:

- BSA
- PLLA
- PLA-PEG
- PLA/Rifampicin

The mean diameter of produced particles can range from 0.1 to 3 μm, and the mean dimension depends on the operative condition used in the precipitator and in the saturator. Particularly, the mean diameter decreases when a good solubilization of CO₂ is reached in the saturator, when higher temperatures are selected in the precipitator.

Chapter IX

During this work fruitful collaborations have contributed to validate the results:

SAOT institute in Erlangen, CSIR in Pretoria, Department of Chemistry and Biology (UNISA) and Department of Science for Biology, Geology and Environment (UNISANNIO), Universidad de Zaragoza.

References

(2011). Handbook of Atomization and Sprays: Theory and Applications. *Handbook of Atomization and Sprays: Theory and Applications*, 1-935.

R. Adami, S. Liparoti and E. Reverchon (2011). A new supercritical assisted atomization configuration, for the micronization of thermolabile compounds. *Chem Eng J*, 173, 55-61.

R. Adami, L. S. Osseo and E. Reverchon (2009). Micronization of Lysozyme by Supercritical Assisted Atomization. *Biotechnol Bioeng*, 104, 1162-1170.

T. Adrian and G. Maurer (1997). Solubility of carbon dioxide in acetone and propionic acid at temperatures between 298 K and 333 K. *J Chem Eng Data*, 42, 668-672.

M. A. Al-Nasassrah, F. Podczec and J. M. Newton (1998). The effect of an increase in chain length on the mechanical properties of polyethylene glycols. *Eur J Pharm Biopharm*, 46, 31-38.

S. Anguiano-Igea, F. J. Otero-Espinar, J. L. Vila-Jato and J. Blanco-Méndez (1995). The properties of solid dispersions of clofibrate in polyethylene glycols. *Pharmaceutica Acta Helvetiae*, 70, 57-66.

A. Bamberger, G. Sieder and G. Maurer (2000). High-pressure (vapor+liquid) equilibrium in binary mixtures of (carbon dioxide+water or acetic acid) at temperatures from 313 to 353 K. *The Journal of Supercritical Fluids*, 17, 97-110.

A. M. Barrett, F. Dehghani and N. R. Foster (2008). Increasing the dissolution rate of itraconazole processed by gas antisolvent techniques using polyethylene glycol as a carrier. *Pharmaceut Res*, 25, 1274-1289.

M. K. Barron, T. J. Young, K. P. Johnston and R. O. Williams, 3rd (2003). Investigation of processing parameters of spray freezing into liquid to prepare polyethylene glycol polymeric particles for drug delivery. *AAPS PharmSciTech*, 4, E12.

A. Braeuer, S. Dowy, E. Torino, M. Rossmann, S. K. Luther, E. Schluecker, A. Leipertz and E. Reverchon (2011). Analysis of the supercritical antisolvent mechanisms governing particles precipitation and morphology by in situ laser scattering techniques. *Chem Eng J*, 173, 258-266.

P. M. Bummer (1996). An FTIR study of the structure of human serum albumin adsorbed to polysulfone. *Int J Pharm*, 132, 143-151.

M. Q. Cai, Y. X. Guan, S. J. Yao and Z. Q. Zhu (2008). Supercritical fluid assisted atomization introduced by hydrodynamic cavitation mixer (SAA-HCM) for micronization of levofloxacin hydrochloride. *J Supercrit Fluid*, 43, 524-534.

C. E. P. S. Campos, H. G. D. Villardi, F. L. P. Pessoa and A. M. C. Uller (2009). Solubility of Carbon Dioxide in Water and Hexadecane:

References

Experimental Measurement and Thermodynamic Modeling. *J Chem Eng Data*, 54, 2881-2886.

G. Caputo, R. Adami and E. Reverchon (2010). Analysis of Dissolved-Gas Atomization: Supercritical CO₂ Dissolved in Water. *Ind Eng Chem Res*, 49, 9454-9461.

G. Caputo, S. Liparoti, R. Adami and E. Reverchon (2012). Use of Supercritical CO₂ and N₂ as Dissolved Gases for the Atomization of Ethanol and Water. *Ind Eng Chem Res*, 51, 11803-11808.

G. Caputo, S. Liparoti, R. Adami and E. Reverchon (on-line (ASAP)). Use of supercritical CO₂ and N₂ as dissolved gases for the atomization of ethanol and water *Ind Eng Chem Res*.

S. K. Chen and A. H. Lefebvre (1994). Spray Cone Angles of Effervescent Atomizers. *Atom. Sprays*, 4, 291-301.

H. R. Costantino, L. Firouzabadian, C. C. Wu, K. G. Carrasquillo, K. Griebenow, S. E. Zale and M. A. Tracy (2002). Protein spray freeze drying. 2. Effect of formulation variables on particle size and stability. *J Pharm Sci-US*, 91, 388-395.

D. Q. M. Craig (1995). A Review of Thermal Methods Used for the Analysis of the Crystal Form, Solution Thermodynamics and Glass-Transition Behavior of Polyethylene Glycols. *Thermochim Acta*, 248, 189-203.

K. J. Crowley and G. Zografi (2003). The effect of low concentrations of molecularly dispersed poly(vinylpyrrolidone) on indomethacin crystallization from the amorphous state. *Pharmaceut Res*, 20, 1417-1422.

B. De Gianninis, A. Vega-Gonzalez and P. Subra (2004). Anti-solvent and co-solvent effect of CO₂ on the solubility of griseofulvin in acetone and ethanol solutions. *J Supercrit Fluid*, 29, 49-57.

N. Delahaye, R. Duclos and J. M. Saiter (1997). Characterization of PEG6000 phase transitions influence of kinetic conditions. *Int J Pharm*, 157, 27-34.

G. Della Porta, R. Adami, P. Del Gaudio, L. Prota, R. Aquino and E. Reverchon (2010). Albumin/Gentamicin Microspheres Produced by Supercritical Assisted Atomization: Optimization of Size, Drug Loading and Release. *J Pharm Sci-US*, 99, 4720-4729.

M. L. Di Lorenzo, M. Cocca and M. Malinconico (2011). Crystal polymorphism of poly(L-lactic acid) and its influence on thermal properties. *Thermochim Acta*, 522, 110-117.

R. P. Don Green (2007). Perry's Chemical Engineers' Handbook, Eighth Edition.

S. Dowy, A. Brauer, R. Schatz, E. Schluecker and A. Leipertz (2009). CO₂ partial density distribution during high-pressure mixing with ethanol in the supercritical antisolvent process. *J Supercrit Fluid*, 48, 195-202.

References

- C. Dumouchel, P. Yongyingsakthavorn and J. Cousin (2009). Light multiple scattering correction of laser-diffraction spray drop-size distribution measurements. *International Journal of Multiphase Flow*, 35, 277-287.
- S. Essa, J. M. Rabanel and P. Hildgen (2010). Effect of polyethylene glycol (PEG) chain organization on the physicochemical properties of poly(D, L-lactide) (PLA) based nanoparticles. *Eur J Pharm Biopharm*, 75, 96-106.
- S. Freitas, H. P. Merkle and B. Gander (2004). Ultrasonic atomisation into reduced pressure atmosphere - envisaging aseptic spray-drying for microencapsulation. *J Control Release*, 95, 185-195.
- K. Fu, K. Griebenow, L. Hsieh, A. M. Klibanov and R. Langer (1999). FTIR characterization of the secondary structure of proteins encapsulated within PLGA microspheres. *J Control Release*, 58, 357-366.
- R. Gref, M. Luck, P. Quellec, M. Marchand, E. Dellacherie, S. Harnisch, T. Blunk and R. H. Muller (2000). 'Stealth' corona-core nanoparticles surface modified by polyethylene glycol (PEG): influences of the corona (PEG chain length and surface density) and of the core composition on phagocytic uptake and plasma protein adsorption. *Colloid Surface B*, 18, 301-313.
- Ö. L. Gülder (1990). Multiple Scattering Effects in Dense Spray Sizing by Laser Diffraction. *Aerosol Sci Tech*, 12, 570-577.
- F. Han, Y. Xue, Y. L. Tian, X. F. Zhao and L. Chen (2005). Vapor-liquid equilibria of the carbon dioxide plus acetone system at pressures from (2.36 to 11.77) MPa and temperatures from (333.15 to 393.15) K. *J Chem Eng Data*, 50, 36-39.
- T. Hauet and M. Eugene (2008). A new approach in organ preservation: potential role of new polymers. *Kidney international*, 74, 998-1003.
- W. Z. He, Q. L. Suo, H. L. Hong, A. Shan, C. P. Li, Y. C. Huang, Y. X. Li and M. D. Zhu (2007). Production of natural carotene-dispersed polymer microparticles by SEDS-PA co-precipitation. *J Mater Sci*, 42, 3495-3501.
- C. R. Heald, S. Stolnik, K. S. Kujawinski, C. De Matteis, M. C. Garnett, L. Illum, S. S. Davis, S. C. Purkiss, R. J. Barlow and P. R. Gellert (2002). Poly(lactic acid)-poly(ethylene oxide) (PLA-PEG) nanoparticles: NMR studies of the central solidlike PLA core and the liquid PEG corona. *Langmuir*, 18, 3669-3675.
- A. M. Hiroyasu, H. Shimizu and M. (1991). Breakup length of a liquid jet and internal flow in a nozzle. *Proc. ICLASS-91*, 26.
- Y. J. Hwang, C. Oh and S. G. Oh (2005). Controlled release of retinol from silica particles prepared in O/W/O emulsion: The effects of surfactants and polymers. *J Control Release*, 106, 339-349.
- L. Izzo and D. Pappalardo (2010). "Tree-Shaped" Copolymers Based on Poly(ethylene glycol) and Atactic or Isotactic Polylactides: Synthesis and Characterization. *Macromol Chem Phys*, 211, 2171-2178.
- G. B. Jacobson, E. Gonzalez-Gonzalez, R. Spitler, R. Shinde, D. Leake, R. L. Kaspar, C. H. Contag and R. N. Zare (2010). Biodegradable

References

Nanoparticles With Sustained Release of Functional siRNA in Skin. *J Pharm Sci-U.S.*, 99, 4261-4266.

Y. L. Jeyachandran, E. Mielczarski, B. Rai and J. A. Mielczarski (2009). Quantitative and qualitative evaluation of adsorption/desorption of bovine serum albumin on hydrophilic and hydrophobic surfaces. *Langmuir*, 25, 11614-11620.

H. Kamada, Y. Tsutsumi, Y. Yamamoto, T. Kihira, Y. Kaneda, Y. Mu, H. Kodaira, S. I. Tsunoda, S. Nakagawa and T. Mayumi (2000). Antitumor activity of tumor necrosis factor-alpha conjugated with polyvinylpyrrolidone on solid tumors in mice. *Cancer Res*, 60, 6416-20.

F. I. Kanaze, E. Kokkalou, I. Niopas, P. Barmplexis, E. Georarakis and D. Bikiaris (2010). Dissolution rate and stability study of flavanone aglycones, naringenin and hesperetin, by drug delivery systems based on polyvinylpyrrolidone (PVP) nanodispersions. *Drug Dev Ind Pharm*, 36, 292-301.

J. Kiefer (2010). Dual-Wavelength Raman Spectroscopy Approach for Studying Fluid-Phase Equilibria Using a Single Laser. *Appl. Spectrosc.*, 64, 687-689.

Ž. Knez, M. Škerget, L. Ilič and C. Lütge (2008). Vapor-liquid equilibrium of binary CO₂-organic solvent systems (ethanol, tetrahydrofuran, ortho-xylene, meta-xylene, para-xylene). *The Journal of Supercritical Fluids*, 43, 383-389.

M. Kurs, G. F. Walker, V. Roessler, M. Ogris, W. Roedl, R. Kircheis and E. Wagner (2003). Novel shielded transferrin-polyethylene glycol-polyethylenimine/DNA complexes for systemic tumor-targeted gene transfer. *Bioconjugate chemistry*, 14, 222-31.

A. N. Kuznetsov, B. Ebert, G. Lassmann and A. B. Shapiro (1975). Adsorption of small molecules to bovine serum albumin studied by the spin probe method. *Biochimica et Biophysica Acta*, 379, 139-146.

F. X. Lacasse, P. Hildgen and J. N. McMullen (1998). Surface and morphology of spray-dried pegylated PLA microspheres. *Int J Pharm*, 174, 101-109.

H. Y. Lee, S. H. Lee, C. J. Xu, J. Xie, J. H. Lee, B. Wu, A. L. Koh, X. Y. Wang, R. Sinclair, S. Xwang, D. G. Nishimura, S. Biswal, S. H. Sun, S. H. Cho and X. Y. Chen (2008). Synthesis and characterization of PVP-coated large core iron oxide nanoparticles as an MRI contrast agent. *Nanotechnology*, 19.

A. Lefebvre 1988. *Atomization and Sprays*, Taylor & Francis.

P. Legrand, S. Lesieur, A. Bochot, R. Gref, W. Raatjes, G. Barratt and C. Vauthier (2007). Influence of polymer behaviour in organic solution on the production of polylactide nanoparticles by nanoprecipitation. *Int J Pharm*, 344, 33-43.

References

- T. Li, K. Nishida and H. Hiroyasu (2011). Droplet size distribution and evaporation characteristics of fuel spray by a swirl type atomizer. *Fuel*, 90, 2367-2376.
- R. T. Liggins and H. M. Burt (2004). Paclitaxel loaded poly(lactic acid) (PLLA) microspheres II. The effect of processing parameters on microsphere morphology and drug release kinetics. *Int J Pharm*, 281, 103-106.
- S. P. Lin and R. D. Reitz (1998). Drop and spray formation from a liquid jet. *Annu Rev Fluid Mech*, 30, 85-105.
- V. J. C. Lin and J. L. Koenig (1976). Raman studies of bovine serum albumin. *Biopolymers*, 15, 203-218.
- K. Lopez and A. Leipertz (2010). Lab course: Raman spectroscopy. *LTT Erlangen*.
- J. R. Manion, S. P. Cape, D. H. McAdams, L. G. Rebits, S. Evans and R. E. Sievers (2012). Inhalable Antibiotics Manufactured Through Use of Near-Critical or Supercritical Fluids. *Aerosol Sci Tech*, 46, 403-410.
- T. M. Martin, N. Bandi, R. Shulz, C. B. Roberts and U. B. Kompella (2002). Preparation of budesonide and budesonide-PLA microparticles using supercritical fluid precipitation technology. *AAPS PharmSciTech*, 3, E18.
- A. Matsumoto, T. Kitazawa, J. Murata, Y. Horikiri and H. Yamahara (2008). A novel preparation method for PLGA microspheres using non-halogenated solvents. *J Control Release*, 129, 223-227.
- K. Matsuyama, K. Mishima, K. I. Hayashi, H. Ishikawa, H. Matsuyama and T. Harada (2003). Formation of microcapsules of medicines by the rapid expansion of a supercritical solution with a nonsolvent. *J Appl Polym Sci*, 89, 742-752.
- S. J. McClellan and E. I. Franses (2003). Effect of concentration and denaturation on adsorption and surface tension of bovine serum albumin. *Colloids and Surfaces B: Biointerfaces*, 28, 63-75.
- K. Mishima, K. Matsuyama, D. Tanabe, S. Yamauchi, T. J. Young and K. P. Johnston (2000). Microencapsulation of proteins by rapid expansion of supercritical solution with a nonsolvent. *Aiche J*, 46, 857-865.
- P. Mishra, K. Griebenow and A. M. Klibanov (1996). Structural basis for the molecular memory of imprinted proteins in anhydrous media. *Biotechnol Bioeng*, 52, 609-614.
- R. A. Mugele and H. D. Evans (1951). Droplet Size Distribution in Sprays. *Industrial & Engineering Chemistry*, 43, 1317-1324.
- S. P. Nalawade, F. Picchioni and L. P. B. M. Janssen (2007). Batch production of micron size particles from poly(ethylene glycol) using supercritical CO₂ as a processing solvent. *Chem Eng Sci*, 62, 1712-1720.
- J. Oakes (1976). Thermally denatured proteins: Nuclear magnetic resonance, binding isotherm and chemical modification studies of thermally denatured bovine serum albumin. *Journal of the Chemical Society, Faraday Transactions 1: Physical Chemistry in Condensed Phases*, 72, 228-237.

References

- M. Ogris, S. Brunner, S. Schuller, R. Kircheis and E. Wagner (1999). PEGylated DNA/transferrin-PEI complexes: reduced interaction with blood components, extended circulation in blood and potential for systemic gene delivery. *Gene therapy*, 6, 595-605.
- P. Pan, Z. Liang, B. Zhu, T. Dong and Y. Inoue (2008). Roles of physical aging on crystallization kinetics and induction period of poly(L-lactide). *Macromolecules*, 41, 8011-8019.
- B. S. Park and S. Y. Lee (1994). An Experimental Investigation of the Flash Atomization Mechanism. *Atom. Sprays*, 4, 159-179.
- F. S. Parker (1986). Biochemical Applications of Fourier-Transform Infrared-Spectroscopy. *Can J Spectrosc*, 31, 1-6.
- C. J. Peters and L. J. Florusse (1995). Experimental determination of vapor-liquid equilibria in binary mixtures of carbon dioxide + chloroform. *Journal of Chemical & Engineering Data*, 40, 948-949.
- E. Reverchon (2002a). Supercritical-assisted atomization to produce micro- and/or nanoparticles of controlled size and distribution. *Industrial and Engineering Chemistry Research*, 41, 2405-2411.
- E. Reverchon (2002b). Supercritical-assisted atomization to produce micro- and/or nanoparticles of controlled size and distribution. *Ind Eng Chem Res*, 41, 2405-2411.
- E. Reverchon, R. Adami and G. Caputo (2007a). Production of cromolyn sodium microparticles for aerosol delivery by supercritical assisted atomization. *AAPS PharmSciTech*, 8.
- E. Reverchon, R. Adami and G. Caputo (2007b). Production of cromolyn sodium microparticles for aerosol delivery by supercritical assisted atomization. *AAPS PharmSciTech*, 8, 272-280.
- E. Reverchon, R. Adami, G. Caputo and I. De Marco (2008a). Spherical microparticles production by supercritical antisolvent precipitation: Interpretation of results. *The Journal of Supercritical Fluids*, 47, 70-84.
- E. Reverchon, R. Adami, S. Cardea and G. Della Porta (2009). Supercritical fluids processing of polymers for pharmaceutical and medical applications. *J Supercrit Fluid*, 47, 484-492.
- E. Reverchon, R. Adami, M. Scognamiglio, G. Fortunato and G. Della Porta (2010a). Beclomethasone Microparticles for Wet Inhalation, Produced by Supercritical Assisted Atomization. *Ind Eng Chem Res*, 49, 12747-12755.
- E. Reverchon and A. Antonacci (2006a). Chitosan microparticles production by supercritical fluid processing. *Ind Eng Chem Res*, 45, 5722-5728.
- E. Reverchon and A. Antonacci (2006b). Cyclodextrins micrometric powders obtained by supercritical fluid processing. *Biotechnol Bioeng*, 94, 753-761.
- E. Reverchon and A. Antonacci (2007). Polymer microparticles production by supercritical assisted atomization. *J Supercrit Fluid*, 39, 444-452.

References

- E. Reverchon, G. Caputo, S. Corraera and P. Cesti (2003). Synthesis of titanium hydroxide nanoparticles in supercritical carbon dioxide on the pilot scale. *J Supercrit Fluid*, 26, 253-261.
- E. Reverchon, G. Lamberti and A. Antonacci (2008b). Supercritical fluid assisted production of HPMC composite microparticles. *J Supercrit Fluid*, 46, 185-196.
- E. Reverchon, E. Torino, S. Dowy, A. Braeuer and A. Leipertz (2010b). Interactions of phase equilibria, jet fluid dynamics and mass transfer during supercritical antisolvent micronization. *Chem Eng J*, 156, 446-458.
- T. Riley, C. R. Heald, S. Stolnik, M. C. Garnett, L. Illum, S. S. Davis, S. M. King, R. K. Heenan, S. C. Purkiss, R. J. Barlow, P. R. Gellert and C. Washington (2003). Core-shell structure of PLA-PEG nanoparticles used for drug delivery. *Langmuir*, 19, 8428-8435.
- R. Sadove (2009). Injectable Poly-L-Lactic Acid: A Novel Sculpting Agent for the Treatment of Dermal Fat Atrophy After Severe Acne. *Aesthetic Plastic Surgery*, 33, 113-116.
- P. Samyn, G. Schoukens, I. Van Driessche, J. Van Craenenbroeck and F. Verpoort (2006). Softening and melting mechanisms of polyamides interfering with sliding stability under adhesive conditions. *Polymer*, 47, 5050-5065.
- Y. Sato, N. Hosaka, K. Yamamoto and H. Inomata (2010). Compact apparatus for rapid measurement of high-pressure phase equilibria of carbon dioxide expanded liquids. *Fluid Phase Equilibria*, 296, 25-29.
- B. Schrader (2008). Infrared and Raman Spectroscopy: methods and applications. *John Wiley & Sons*.
- P. Seydel, J. Blomer and J. Bertling (2006). Modeling particle formation at spray drying using population balances. *Dry Technol*, 24, 137-146.
- M. T. Sheu, A. B. Wu, K. P. Lin, C. H. Shen and H. O. Ho (2006). Effect of tocopheryl polyethylene glycol succinate on the percutaneous penetration of minoxidil from water/ethanol/polyethylene glycol 400 solutions. *Drug Dev Ind Pharm*, 32, 595-607.
- R. E. Sievers, E. T. S. Huang, J. A. Villa, G. Engling and P. R. Brauer (2003). Micronization of water-soluble or alcohol-soluble pharmaceuticals and model compounds with a low-temperature Bubble Dryer (R). *J Supercrit Fluid*, 26, 9-16.
- R. E. Sievers, E. T. S. Huang, J. A. Villa, J. K. Kawamoto, M. M. Evans and P. R. Brauer (2001). Low-temperature manufacturing of fine pharmaceutical powders with supercritical fluid aerosolization in a Bubble Dryer (R). *Pure Appl Chem*, 73, 1299-1303.
- W. Somchue, W. Sermsri, J. Shiowatana and A. Siripinyanon (2009). Encapsulation of alpha-tocopherol in protein-based delivery particles. *Food Res Int*, 42, 909-914.

References

- S. D. Sovani, J. D. Crofts, P. E. Sojka, J. P. Gore and W. A. Eckerle (2005). Structure and steady-state spray performance of an effervescent diesel injector. *Fuel*, 84, 1503-1514.
- S. D. Sovani, P. E. Sojka and A. H. Lefebvre (2001). Effervescent atomization. *Prog Energ Combust*, 27, 483-521.
- S. Spilimbergo, N. Elvassore and A. Bertuccio (2002). Microbial inactivation by high-pressure. *J Supercrit Fluid*, 22, 55-63.
- A. Stratmann and G. Schweiger (2002). Fluid Phase Equilibria of Ethanol and Carbon Dioxide Mixtures with Concentration Measurements by Raman Spectroscopy. *Appl. Spectrosc.*, 56, 783-788.
- B. S. Teo, M. Basri, M. R. Zakaria, A. B. Salleh, R. N. Rahman and M. B. Rahman (2010). A potential tocopherol acetate loaded palm oil esters-in-water nanoemulsions for nanocosmeceuticals. *Journal of nanobiotechnology*, 8, 4.
- P. Törmälä (1974). Determination of glass transition temperature of poly(ethylene glycol) by spin probe technique. *European Polymer Journal*, 10, 519-521.
- P. Vanhoorne, P. Dubois, R. Jerome and P. Teyssie (1992). Macromolecular Engineering of Polylactones and Polylactides .7. Structural-Analysis of Copolyesters of Epsilon-Caprolactone and L-Caprolactone or D,L-Lactide Initiated by Al(OiPr)₃. *Macromolecules*, 25, 37-44.
- S. Varona, A. Braeuer, A. Leipertz, Á. Martín, E. Schluecker and M. J. Cocero (2012). Lycopene Solubility in Mixtures of Carbon Dioxide and Ethyl Acetate. *10th International Symposium on Supercritical Fluids, May 13-16, 2012, San Francisco (USA)*.
- R. Vehring, W. R. Foss and D. Lechuga-Ballesteros (2007). Particle formation in spray drying. *J Aerosol Sci*, 38, 728-746.
- A. Vila, H. Gill, O. Mccallion and M. J. Alonso (2004a). Transport of PLA-PEG particles across the nasal mucosa: effect of particle size and PEG coating density. *J Control Release*, 98, 231-244.
- A. Vila, H. Gill, O. Mccallion and M. J. Alonso (2004b). Transport of PLA-PEG particles across the nasal mucosa: effect of particle size and PEG coating density. *J Control Release*, 98, 231-44.
- O. W (1936). Formation of drops by nozzles and the breakup of liquid jets. *Z Angew Math Mech* 16, 355-358.
- R. A. Wade, J. M. Weerts, P. E. Sojka, J. P. Gore and W. A. Eckerle (1999). Effervescent atomization at injection pressures in the MPa range. *Atom. Sprays*, 9, 651-667.
- Q. Wang, Y. X. Guan, S. J. Yao and Z. Q. Zhu (2010). Microparticle formation of sodium cellulose sulfate using supercritical fluid assisted atomization introduced by hydrodynamic cavitation mixer. *Chem Eng J*, 159, 220-229.
- Q. Wang, Y. X. Guan, S. J. Yao and Z. Q. Zhu (2011). Controllable preparation and formation mechanism of BSA microparticles using

References

- supercritical assisted atomization with an enhanced mixer. *J Supercrit Fluid*, 56, 97-104.
- M. Wendland, H. HaseandG. Maurer (1994). Multiphase High-Pressure Equilibria of Carbon-Dioxide Water Acetone. *J Supercrit Fluid*, 7, 245-250.
- I. Weuts, D. Kempen, G. Verreck, A. Decorte, K. Heymans, J. Peeters, M. BrewsterandG. Van Den Mooter (2005). Study of the physicochemical properties and stability of solid dispersions of loperamide and PEG6000 prepared by spray drying. *Eur J Pharm Biopharm*, 59, 119-126.
- J. Xiao, Z. Huang, J. J. MaandX. Q. Qiao (2009). An Experimental Study on Spray Transient Characteristics in Fuel Containing Co₂. *Atom. Sprays*, 19, 311-320.
- K. Yasugi, Y. Nagasaki, M. KatoandK. Kataoka (1999). Preparation and characterization of polymer micelles from poly(ethylene glycol)-poly(D,L-lactide) block copolymers as potential drug carrier. *J Control Release*, 62, 89-100.
- S. H. Yoo, Y. B. Song, P. S. ChangandH. G. Lee (2006). Microencapsulation of alpha-tocopherol using sodium alginate and its controlled release properties. *Int J Biol Macromol*, 38, 25-30.
- N. Yoshimura (2008). Vacuum Technology, Practice for Scientific Instruments. *Springer Berlin Heidelberg*.

List of symbols

$\frac{\partial \sigma}{\partial \Omega}$	scattering cross section
μ :	viscosity of CO ₂ -solution mixture
A:	transversal pipe area
a :	droplet radius
B_e	rotational constant
BSA:	Bovine serum albumin
C:	conductance
c :	speed of light
C:	concentration of solute
C _p :	specific heat
d :	moleculolar diameter
D:	nozzle diameter
D _e :	equivalent diameter
DLS:	dynamic laser scattering
DSC:	differential scanning calorimeter
E	electrical field strength
F:	rotational term value
FTIR:	Fourier transform infrared
G(ν):	vibrational term value
GLR:	mass of CO ₂ /mass of solution
GPC:	gel permeation chromatography
H:	enthalpy
h :	Planck's constant
HPLC:	high performance liquid chromatography
I_0	laser intensity
I_e :	moment of inertia
I_{ps}	intensity with a special polarization
J:	rotational quantum number
j_i :	mass flux
k	Boltzmann's constant (VLE Raman detection)
k :	gas thermal conductivity
Kn:	Knudsen number
L	length of the measurement volume
L:	mean free path
L:	pipe length
M	product [L]
m :	droplet mass
m :	mass
M _n :	molecular mass
M _w :	molecular weight
MW:	molecular weight

n:	number density
P	polarisation
P:	pressure
p:	pressure
P_A	start pressure [mbar];
PEG:	polyethylene glycol
p_f :	final pressure
PI:	polydispersity index
p_l :	limit pressure
PLA-PEG:	copolymer polylactic acid-polyethylen glycol
PLLA:	poly-L-lactic acide
p_m :	pressure in the saturator
P_{MD}	evaporation pressure [mbar];
p_p :	pressure in the precipitator
P_{RS}	vapor lived from the metallic surface [mbar L/s m ²]
PSD:	particle size distribution
PVP:	polyvinyl pirrolidone
Q:	gas flow rate
Q_{CO_2} :	CO ₂ mass flow rate
Q_L	gas flowrate [mbar L/sec]
R	distance of atoms
R:	costant for ideal gas
r_0 :	pipe radius
Re:	Reynolds number
S:	particle surface
SAA:	supercritical assisted atomization
SC-CO ₂ :	supercritical carbon dioxide
S_W	lateral surface of the vessel [m ²];
T	evacuation time from the start pressure P_A to the condensation pressure [h];
T	temperature
T:	operating temperature
T_0 :	273 K
T_1, T_2	term value
T_∞ :	bulk temperature
T_m :	temperature in the saturator
t_{MD}	evaporation time [h]
T_p :	temperature in the precipitator
T_s :	interfacial temperature
U_{rot} :	internal rotational energy
V	volume of the system [m ³]
v:	jet velocity at nozzle exit
V:	particle volume

ν :	vibrational quantum number (VLE Raman scattering)
We:	Weber number
We_g :	gas Weber number
We_L :	liquid Weber number
Z:	compressibility
Z:	Ohnesorge number
α -TCP:	α -tocopherol acetate
ΔH_f :	enthalpy of fusion
η :	viscosity
λ_{vap} :	heat of vaporization
ρ :	density of CO ₂ -solution mixture
σ :	surface tension solution-drying medium
ΔE	energy difference between molecule levels
Ω	room angle
α	polarisability
ϵ_0	dielectric constant
μ	reduced mass (VLE Raman detection)
ν_i	indication of the different molecule vibrations
ν_0	laser frequency